SURFACE CURRENT OBSERVATIONS USING HIGH FREQUENCY RADAR AND ITS ASSIMILATION INTO THE NEW YORK HARBOR OBSERVING AND PREDICTION SYSTEM

by

GANESH GOPALAKRISHNAN

A DISSERTATION

Submitted to the Faculty of the Stevens Institute of Technology
in partial fulfillment of the requirements for the degree of

DOCTOR OF PHILOSOPHY

Ganesh Gy	09/12/08
Ganesh Gopalakrishnan, Candidate	Date

ADVISORY COMMITTEE

Alan F. Blumberg	9/12/08
Alan F. Blumberg, Chairman	Date
Richard I. Hires	9/12/08
Richard I. Hires, Co-Adviser	Date
Thomas O. Herrington	9/12/08
Thomas O. Herrington, Member	Date
Siva Thangam	9/12/08
Siva Thangam, Member	Date
Scott Glenn	9/12/08
Scott M. Glenn, Member	Date

STEVENS INSTITUTE OF TECHNOLOGY
Castle Point on the Hudson,
Hoboken, NJ 07030
2008

ABSTRACT

SURFACE CURRENT OBSERVATIONS USING HIGH FREQUENCY RADAR AND ITS ASSIMILATION INTO THE NEW YORK HARBOR OBSERVING AND PREDICTION SYSTEM

A surface current observation system based on high-frequency (HF) radar (CODAR) has been constructed for Raritan Bay, NJ; and the New York Bight (NYB) Apex. The availability of surface current data measured using HF radar in real-time over a synoptic scale makes it appropriate for data assimilation (DA). The present work is an attempt to validate HF radar data in the NYB Apex and to develop a practical, but still nearly optimal, method to assimilate HF radar data into an estuarine and coastal ocean circulation model in a tidally-dominated region of NY/NJ Harbor Estuary and the NYB Apex. This model, forced by an extensive real-time observational network, is called the New York Harbor Observing and Prediction System (NYHOPS). A nudging or Newtonian damping scheme is developed to assimilate HF radar data. A nudging parameter is introduced into the equations of motion which affects the model dynamics. The data is imparted to neighboring (three-dimensional) grid points via model dynamics. The effectiveness of HF radar DA is studied by computing the *DA skill* based on mean square error. A positive *DA skill* (0 − 100%) represents an improvement in the model performance by HF radar DA.

The HF radar data validation study showed a reasonable comparison between HF radar surface currents and near-surface *in-situ* currents obtained from one out of the two

moorings. HF radar DA experiments focused on both the hindcasting as well as forecast capabilities of the NYHOPS model with respect to three regions; inner-shelf region (0 – 30 m), mid-shelf (30 – 90m), and outer-shelf (90 – 120 m). For the inner-NJ shelf region, based on NYHOPS model hindcasts, a 40 day long DA study using HF radar data in Raritan Bay and the NYB Apex region yielded a *DA skill* of +22% for near-surface currents (with respect to mooring data), and +53% and +38% for near-surface temperature and salinity (with respect to Glider/fixed sensor data). Based on NYHOPS model forecasts, for the inner-NJ shelf region, another 120 days long DA study using HF radar data in the NYB region yielded a *DA skill* of +11% for near-surface currents (with respect to mooring data), and +10% and +16% for near-surface temperature and salinity (with respect to Glider/fixed sensor data). The *DA skill* for temperature and salinity is higher in the inner-NJ shelf (0 – 30m) region and decreases steadily towards mid-NJ shelf (30 – 90m) and outer-NJ shelf (90 – 120m) regions. The nudging scheme is found to be robust and efficient for the NYHOPS model with minimum computational burden.

Author: Ganesh Gopalakrishnan

Advisor: Prof. Alan F. Blumberg

Co-Advisor: Prof. Richard I. Hires

Date: August 31st, 2008

Degree: Doctor of Philosophy

Department: Civil, Environmental, and Ocean Engineering

ACKNOWLEDGEMENTS

DEDICATION

To my Beloved Mother – Ganapathy Bhagyalakshmi Krishnambal

and my Brother & Family

TABLE OF CONTENTS

LIST OF TABLES

LIST OF FIGURES

Chapter 1

Introduction

1.1   Overview and Motivation

The coastal ocean has been studied by oceanographers with a focus on maritime security, growth and balance of the marine eco-system, recreation, beach erosion, and maritime safety. The combined system of rivers, estuaries, and continental shelf waters, represent a complex hydrodynamic environment, governed by astronomical tides, surface meteorology (wind, heat and salt fluxes), river discharge, geophysical variability (Ekman drift, Stokes drift, and baroclinicity), bathymetry, earth rotation, and large scale ocean circulation. Ocean current is one of the more critical parameters in coastal oceanography, responsible for the various physical and dynamic processes in the coastal zone. Ocean currents are important in terms of vessel navigation, search and rescue operations, heat and mass transport, plankton ecology, ocean circulation and mixing processes. The spatial and temporal variability of ocean surface currents are of critical importance for many practical applications in different fields. One of these applications is with respect to safe and secured vessel navigation, especially in the present study area of the New York

Bight (NYB) Apex, through which the majority of waterborne traffic in and out of the New York/New Jersey (NY/NJ) Harbor passes.

Measurement of ocean surface currents is difficult using conventional current measuring instruments such as Acoustic Doppler Current Profiler (ADCP), and current meter, which are either deployed in the water (fixed frame), or mounted to a vessel (moving frame). The dynamic nature of the ocean surface and vessel traffic renders a challenging environment to measure surface currents. These water based current measuring instruments provide the temporal variations of the ocean current at particular depths, but not at the surface.

The motivation of the present work is to explore the immense capabilities of measuring surface currents using High Frequency (HF) radar technology and its practical application by assimilating the measured surface current data into an estuarine and coastal ocean circulation model, providing more accurate hindcasts, nowcasts, and forecasts for the study domain. The present work deals with surface current measurements which uses relatively new, land-based HF radar systems. HF radar technique uses reflection of electromagnetic pulses to probe ocean surface currents. HF radar system provides both spatial and temporal variations of near-surface current which are averaged over the depth, theoretically expressed as a function of the transmitting frequency (Traditional HF radar system operates in the frequency band of 3 ~ 30 MHz). The present work uses the Coastal Ocean Dynamics Application Radar (CODAR) HF radar system which operates in the frequency band of 3 ~ 50 MHz, and utilizes a unique three-element crossed-loop/monopole antennas and direction-finding algorithm. The

motivation for the present study can be elaborated with respect to the practical applications of HF radar data and ocean forecast model simulations as:

- *Data Assimilation (DA):* Surface current data remotely measured using HF radar over a synoptic scale of O(200 km) can be effectively assimilated into the ocean circulation model to enhance the model hindcasting/forecasting capabilities.

- *Maritime Safety:* Ocean surface current maps representing the spatial and temporal variability of currents help pilots more to safely navigate their ships by avoiding stronger currents, vortices, and narrow channels.

- *Maritime Security:* HF radar technology is a powerful tool for the ship surveillance providing continuous monitoring of ships by transmitting radio pulses with range ~ 400 km, and can be used to identify any potential threats to the maritime security.

- *Environmental:* Ocean surface currents are of great importance in understanding and predicting the trajectories of contaminants, oil spills, and floatables.

- *Oceanographic:* Ocean current circulation influences the mixing processes and baroclinicity, and helps to estimate the mass and momentum transport. Ocean currents are also associated with upwelling and downwelling processes due to surface meteorology and air-sea interactions, resulting in enhanced ocean mixing and ocean production.

- *Maritime Structures:* Ocean current plays an important role in the design of marine structures. The understanding of the complex, non-linear ocean wave-current interaction helps to estimate the pressure distribution and the forces on the

marine structures and shore-connected structures such as breakwaters, groins, and sea walls.

- *Beach Morphodynamics:* Coastal current circulation is important with respect to sediment transport and the associated beach erosion/accretion and scouring of the marine structures. The coastal current circulation pattern helps to design the shore protection structures, scour protection, and beach nourishment programs.
- *Search and Rescue:* Ocean surface current information helps to improve the Search And Rescue (SAR) operations, especially during nights and extreme weather conditions with low visibility.

1.2 Objectives

The main objectives of the present work are to obtain real-time ocean surface current measurements in Raritan Bay, NJ; and the NYB Apex using novel shore-based HF radar system and its practical application by assimilating it into the New York Harbor Observing and Prediction System (NYHOPS) model. The complete objectives of the present work are listed below:

- To understand the working principles of the HF radar system. The present work utilizes CODAR seasonde HF radar system.
- To obtain the radial current measurements using HF radar system and to compute the total current field by combining the radial currents from two or more different HF radar systems.

- To validate the HF radar surface currents in the NYB Apex region using *in-situ* current measurements.

- To assimilate the surface currents measured using standard-range HF radar network in a tidally-dominated region of Raritan Bay and the NYB Apex into the NYHOPS model using a nudging assimilation scheme, and to study the three–dimensional variations of water parameters in the NYB.

- To assimilate the surface currents measured using long-range HF radar network covering the NYB into the NYHOPS model using nudging assimilation scheme and to study the three–dimensional variations of water parameters in the NYB with a focus on the extreme weather flooding event.

- To assess the effectiveness of HF radar DA by computing the *DA skill* score with respect to NYHOPS model hindcasts as well as forecasts (*DA skill* score is based on mean square error between non–assimilated/assimilated model simulations and *in-situ* observations of three-dimensional currents, temperature, and salinity).

1.3   Contributions

Major contributions of the present work are listed below:

- Understanding the sensitivity of the first-order Doppler peak settings of HF radar (CODAR) systems in a tidally-dominated region of NY/NJ Harbor Estuary (see Chapter 3).

- Validating the surface current data measured using HF radar (CODAR) in the NYB Apex using *in–situ* current measurements (see Chapter 4).

- Understanding the three-dimensional modifications of water parameters due to assimilation of surface currents into an estuarine and coastal ocean circulation model using idealized model study of long straight and curved channels (see Chapter 7).

- Assimilating HF radar surface currents into the NYHOPS model for the tidally - dominated region of Raritan Bay and the NYB Apex. Surface currents obtained using standard-range HF radar network as well as long-range HF radar network were assimilated into the NYHOPS model (see Chapters 8 and 9).

- Evaluating the HF radar DA scheme and its effectiveness based on *DA skill* with respect to NYHOPS model hindcasts as well as forecasts (see Chapters 8 and 9).

- Real-time assimilation of HF radar measured surface currents in Raritan bay and the NYB Apex into the NYHOPS operational forecast model.

1.4　Organization of the Thesis

The organization of this Thesis is as below:

Chapter 1 presents a brief overview of the ocean currents and the measurement platforms. This chapter also describes the motivation, objectives and contributions of the present work.

Chapter 2 describes the oceanographic features based on the previous observational and modeling studies in the present study domain, encompassing the regions of MAB, NYB, NY/NJ Harbor Estuary, Long Island Sound, Raritan Bay, and the East River.

Chapter 3 introduces the working principle of HF radar system and the measurement of surface currents. This chapter also reviews the evolution of HF radar technology and the earlier studies on the practical applications of HF radar data.

Chapter 4 discusses the validation of HF radar measured surface currents by comparing it with the *in-situ* current observations. This chapter also reviews earlier HF radar data validation studies.

Chapter 5 introduces the New York Harbor Observing and Prediction System (NYHOPS) model framework, model forcing functions, and the boundary conditions.

Chapter 6 briefly describes about DA technique, and explains about the HF radar DA scheme employed in the present study. This chapter also reviews the previous HF radar DA studies.

Chapter 7 describes the surface current DA into an idealized estuary with a long straight channel and one with a curved configuration, and explains the results with respect to realistic model forcings of river discharge, tide, and density stratification.

Chapter 8 describes the assimilation of surface current data measured in Raritan Bay and the NYB Apex using standard-range HF radar (CODAR) network into the NYHOPS model using a nudging assimilation scheme. This chapter also describes the effectiveness of the DA with respect to NYHOPS model hindcasts.

Chapter 9 describes the assimilation of surface current data measured in the NYB domain using long-range HF radar (CODAR) network into the NYHOPS forecast model using a nudging assimilation scheme. This chapter describes the effectiveness of the DA with respect to NYHOPS model forecasts. This chapter also discusses the NYHOPS model performance with and without HF radar DA during an extreme weather event of coastal flooding.

Chapter 10 summarizes the salient conclusions of this work

Chapter 2

Review of Oceanographic Features of the New York/New Jersey Harbor Estuary and the Adjoining Coastal Waters

2.1   Introduction

The present work is an attempt to study the oceanographic features in Raritan Bay and the NYB Apex using HF radar surface current measurements in conjunction with a three-dimensional ocean circulation model. The hydrodynamic circulation in Raritan Bay and the NYB Apex are interlinked with the estuarine circulation of the NY/NJ Harbor Estuary, and large scale continental shelf circulations of the NYB and the MAB. Previous research studies pertaining to the present study domain of Raritan Bay and the NYB Apex provides a detailed description of the various physical processes. The findings of earlier observational and modeling studies at the NY/NJ Harbor Estuary and adjoining coastal waters are summarized below with respect to each region.

2.2   The Middle Atlantic Bight

The Middle Atlantic Bight (MAB) refers to the curved section of the continental shelf off the eastern United States stretching between Cape Hatteras to the south and Cape Cod and Nantucket Shoals to the northeast. A topographic map showing the MAB region is presented in Figure: 2.1.

The drifter bottle studies by *Bumpus* [1973] in the MAB revealed that the flow was shoreward along the bottom off estuaries, consistent with the inflow of higher salinity near-bottom water into the estuary. Cape Cod (Nantucket Shoals) and Cape Hatteras (Diamond Shoals) appeared to be natural barriers limiting the alongshore flow, and near Cape Hatteras, the flow turned offshore and became entrained into the Gulf Stream. Research studies by *Bigelow* [1933] on the circulation of the MAB revealed that the dominant surface drift (known as "Coastal Drift") on the seaward side of the MAB was towards the southwest, with a mean flow of $O(0.02 \sim 0.1 \text{ m s}^{-1})$ and a mean transport of $\sim$ 250,000 $\text{m}^3 \text{ s}^{-1}$. Inshore of the "Coastal Drift" there is an area of complex hydrography where combined outflows from the Hudson River and other Rivers merged with the Atlantic Ocean. The prevailing southwest flow was found to be weaker in the summer than during winter. *Bigelow* [1933] also reported that a pool of cold water referred as "cold pool", resided on the middle and outer shelf in the summer during which a strong thermo-cline existed.
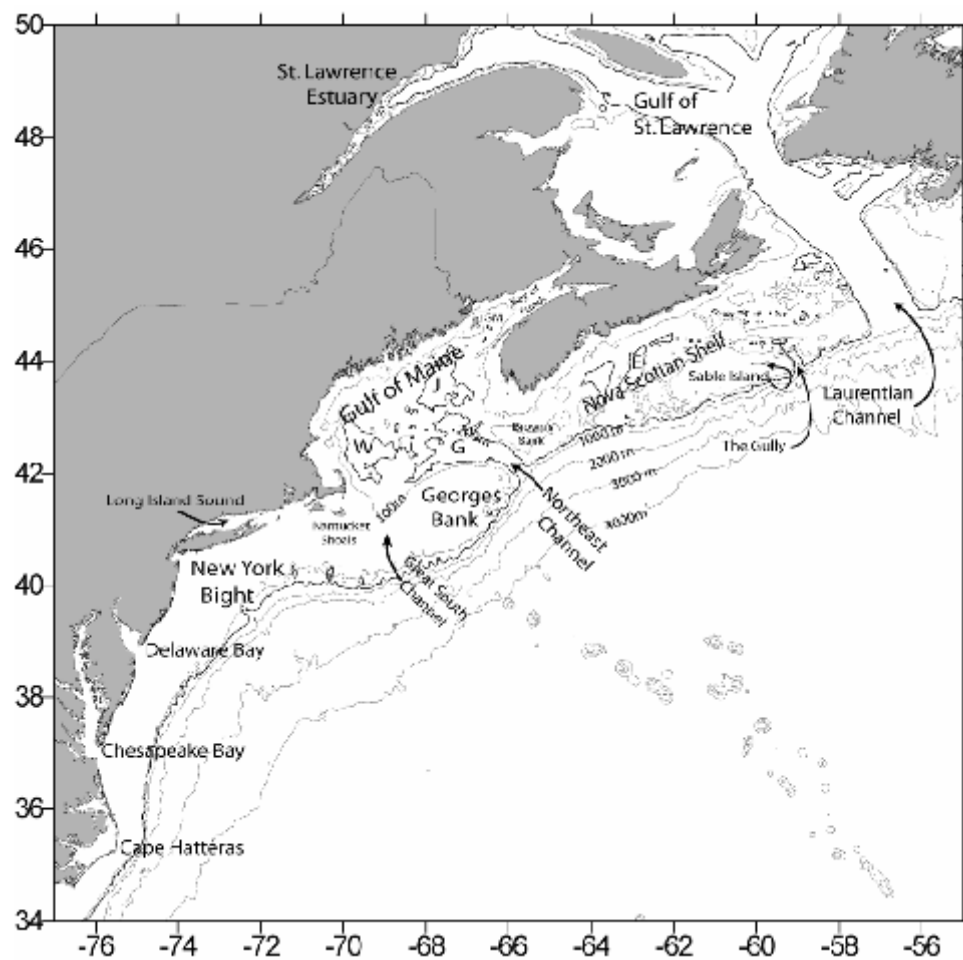
Figure: 2.1.   Topographic map showing the Middle Atlantic Bight

[*Townsend et al*., 2004].

Research studies by *Beardsley et al*. [1976] demonstrated that much of the sub-tidal current variability over the shallow portion of the MAB was directly wind driven in the synoptic scale of O(2 ~ 10 days). The average currents in the NYB generally increased in magnitude offshore and decreased with the depth. *Beardsley and Boicourt* [1981] provided a comprehensive discussion on the circulation in the MAB and the adjoining coastal waters.

Three-dimensional numerical model studies of the long-term mean circulation in the MAB by *Blumberg and Mellor* [1980], *Blumberg and Oey* [1985] found that the presence of the Gulf Stream was an important component of the circulation along the continental shelf of the NYB. Observational studies in the MAB by *Garvine et al*. [1988] reported the presence of eddy features along the continental shelf break. These eddies typically appeared either as plumes of less saline shelf water that protrude into slope water, curling "backwards" opposite to the direction of the mean shelf flow, or as eddies with warmer, saltier slope water within their cores, partly or wholly encircled by the plumes.

2.3   The New York Bight

The New York Bight (NYB) is a subsection of the MAB bounded by a line extending off-shore of Cape May, NJ; to the continental shelf, along the shelf, and off-shore of Montauk Point, NY; to the continental shelf. A topographic map showing the NYB limits is presented in Figure: 2.2.

Ketchum et al. [1951] reported that the water depth in the NYB region averages about 28 m, except at innermost part of the Hudson Canyon. *Geyer and Chant* [2003] reported that the mean volume transport leaving the NY Harbor was about 1000 m^3 s^{-1}, which comprises of 600 m^3 s^{-1} from the Hudson, Raritan, and Passaic Rivers, 300 m^3 s^{-1} from the East River, and 100 m^3 s^{-1} of sewage outflow. As the water passes the Sandy Hook - Rockaway Point (SHRP) transect, it flows along the NJ shore as a coastal current [*Geyer and Chant,* 2003]. This coastal current was observed south up to Cape May, NJ where mixing with waters from the Delaware Bay obscures the plume. *NYDEP* [2003] reported that an annual mean outflow of approximately 3500 m^3 s^{-1} of estuarine water (salt water and fresh water) exits the NY Harbor and enters the NYB, with approximately 2500 m^3 s^{-1} of saline waters from the NYB entering into the NY Harbor. These transports were significantly varied at weekly, monthly, seasonal and inter-annual time scales.

2.4   The New York/New Jersey Harbor Estuary

The New York/New Jersey (NY/NJ) Harbor Estuary is a drowned-river, partially mixed estuary located on the northeast coast of the United States. The NY/NJ Harbor Estuary comprises the tidal waters from the lower Hudson River Estuary from Piermont Marsh in NY to the SHRP transect. The geographic focus includes the Hudson, Passaic,
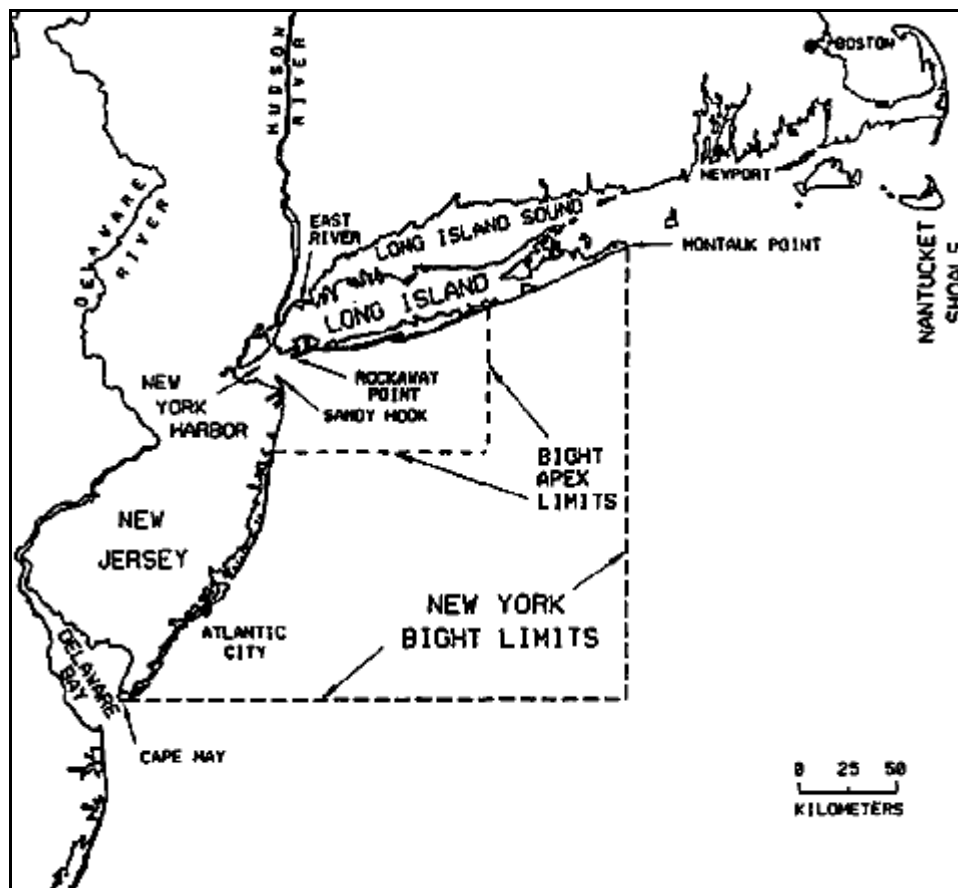
Figure: 2.2.   Topographic map showing the New York Bight [*CERC Report,* 1994].

East, Harlem, Hackensack, Raritan, Navesink and Shrewsbury Rivers, as well as the Raritan Bay, Newark Bay, Jamaica Bay, the Arthur Kill, the Kill Van Kull and the Upper and Lower New York Bays. The water depths are very shallow in the Raritan, Jamaica Bays, and very deep ~ 60 m in the vicinity of West Point, NY. A topographic map of the NY/NJ Harbor Estuary is shown in Figure: 2.3.

Oey et al. [1985a] reported that the major source of freshwater into the NY/NJ Harbor Estuary was from the Hudson River, which discharges through the Upper New York Bay at the Verazzano Narrows into Lower New York Bay and continues onto the NJ coast and the Atlantic Ocean. They reported that a portion of the discharge through the Verazzano Narrows flowed southwesterly along Staten Island into the eastern part of Raritan Bay. The monthly average discharge from the Hudson River Basin varied from 100 m^3 s^{-1} during dry summers to about 1800 m^3 s^{-1} during the springtime. The combined monthly average discharge from the Raritan, Passaic, and Hackensack Rivers varied from 10 m^3 s^{-1} to 100 m^3 s^{-1}. The NY/NJ Harbor Estuary was connected to the Atlantic Ocean through the SHRP transect and Long Island Sound through the East River. The tidal current amplitude was of O(1.0 m s^{-1}) during peak flow near the mouth of the NY/NJ Harbor Estuary. *Geyer et al*. [1996] reported that the estuary was strongly stratified during neap tides and weakly stratified during spring tides, except during peak discharge periods, when it remained stratified for the spring-neap cycle.

NJMSC [1997] reported that the net flow in the NY/NJ Harbor Estuary was a typical two layer flow similar to a partially mixed estuary, with a net outflow of lower salinity surface waters and an inflow of higher salinity waters along the bottom of the

estuary. This two-layer circulation pattern together with tide, wind, and fresh water discharge enhances the estuarine circulation resulting in greater flushing rate of $O(1 \sim 2$ weeks). The reversing tidal currents transported water over distances of $O(5 \sim 10$ km) on either a flood or ebb portion of a tidal cycle. Salinity was observed to be highest at that point where seawater enters into the estuary through the inlets and decreased away from the inlet. Salinity was found to be lower during the spring with increased freshwater inflow, and was found to be higher during the fall, when freshwater inflows were reduced and salt water penetrated further upstream into the estuary.

Research studies by *Ketchum et al*. [1951], *Bowman* [1978] on the Hudson River plume reported that the plume appeared to have two principle modes. During high river flow, the plume followed the NJ coast with a surface salinity front. During low river flow, the freshwater extended southward and eastward over the inner NYB surface.

2.5　Raritan Bay

Raritan Bay and Sandy Hook Bay form the southeastern portion of the NY/NJ Harbor between the northern shoreline of Staten Island, NY; and the southern shoreline of Monmouth County, NJ (see Figure: 2.3). Its head is located at the confluence of the Arthur Kill and the Raritan River, which flows into the bay from the west. The Arthur
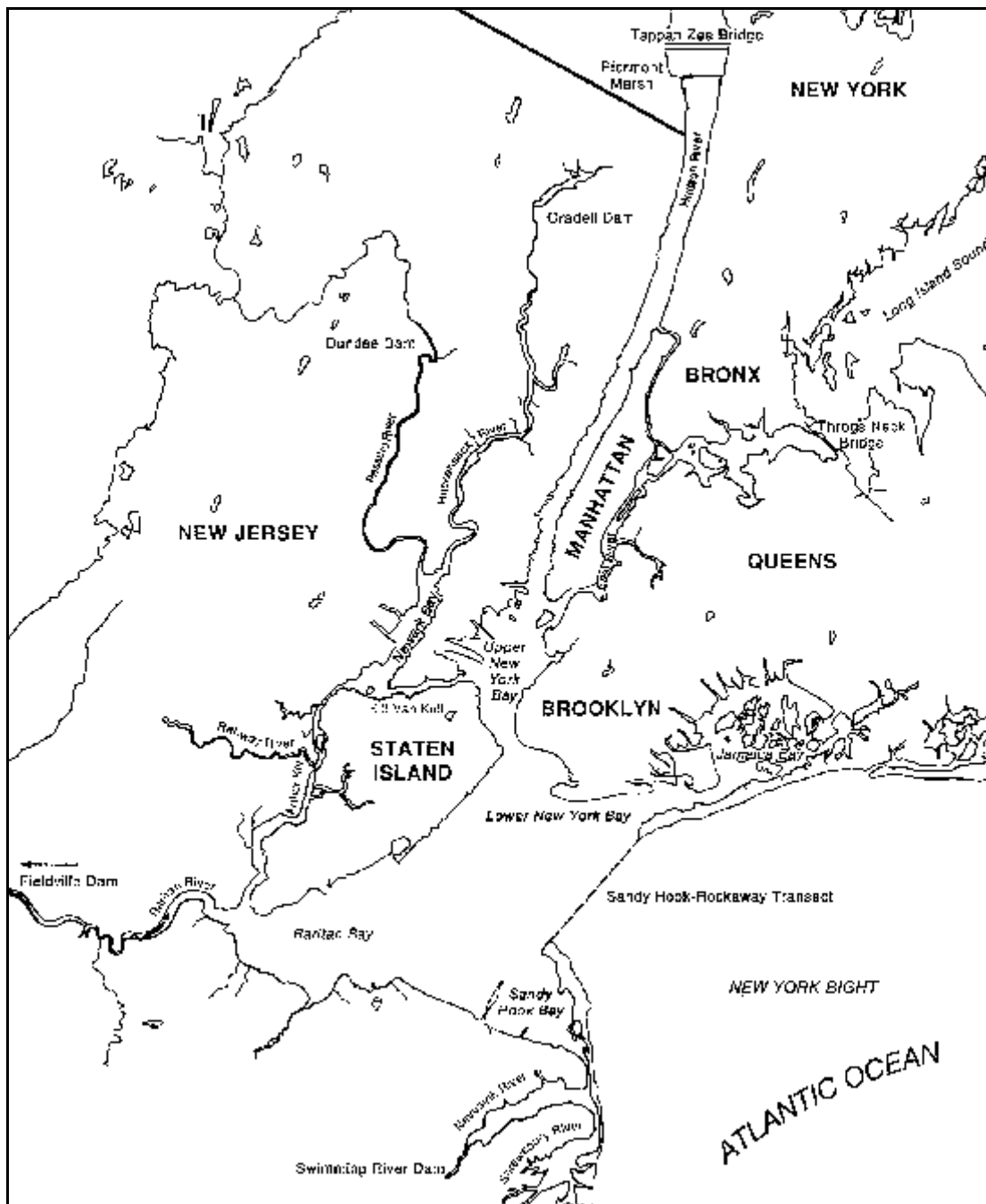
Figure: 2.3.   Topographic map of the NY/NJ Harbor Estuary

[*NY/NJ Harbor Estuary Program*].

Kill and Kill Van Kull are tidal straits that connects Newark, NJ; to Raritan Bay and to NY Harbor.

Jeffries [1962] reported that the Raritan Bay was formed by a system of Bays and Lagoons, which extended ~ 40 km in length and oriented in east-west direction. Raritan Bay can be divided into three parts progressing seaward as Raritan River, Raritan Bay, and Lower New York Bay. Water depths are relatively shallow, increasing gradually from either shore to 7 m in Raritan Bay and 9 m in Lower New York Bay. Raritan Bay has a triangular shape like a flattened funnel, forming an "ideal estuary" with fresh water source from Raritan River and saline water from Lower New York Bay entering the basin at opposite ends with a tendency for each to flow to its respective right side. Estuarine mixing produces a great counter-clockwise gyre of slow circulating water masses inside the Bay. The net currents in Raritan Bay and Lower Bay [*Jeffries,* 1962] (see Figure: 2.4) represented local clockwise eddies at the Great Kills Harbor Point of Staten Island shore and at the Monmouth shore. A net along shore current, directed eastward was observed along the Sandy Hook Bay, which flowed southward along the Sandy Hook and the NJ Shore. *Ketchum* [1950] reported that the flushing rate of Raritan Bay and Lower Bay was primarily dependent on the resultant of localized inequalities in duration and strength of the ebb and flood tides.

Oey et al. [1985b] reported that the hydrodynamic circulation inside Raritan Bay was primarily wind driven, due to its shallow water features. *Blumberg et al*. [1999], *Chant* [2002] reported that high westerly winds over Raritan Bay tend to push the water toward the eastern end of the Lower New York Bay resulting in higher net flows out of
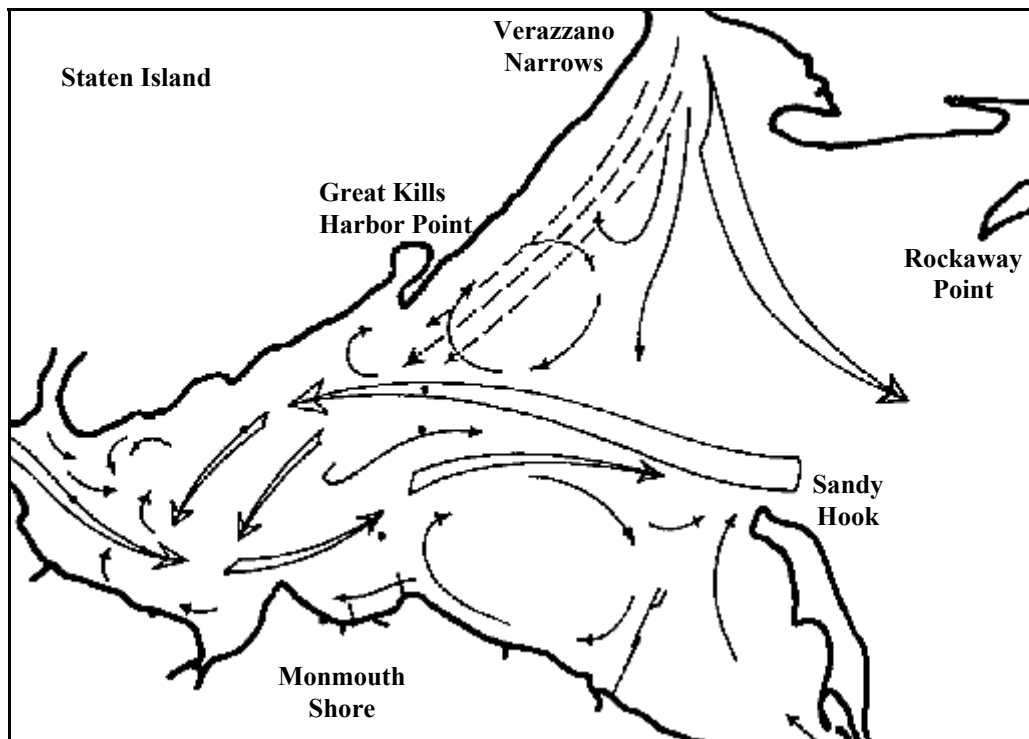
Figure: 2.4.   Schematic representation of net circulation pattern in the Raritan

and Lower Bays [*Jeffries* 1962].

the Kill Van Kull into the Raritan Bay, and these flows tend to last for several days resulting in net transfer of water from Newark Bay to Raritan Bay.

Geyer and Chant [2003] reported that the Kill Van Kull tidal motion was effective in mixing the waters of Newark Bay and NY Harbor while the tides in the Arthur Kill were ineffective in mixing the waters of Raritan Bay and NY Harbor. The Raritan and Passaic Rivers were the major sources of fresh water driving a two-layer exchange in the tidal kills and in the Bays. Wind and water level differences were the dominant forcing for the flow through the Kills and were responsible for the exchange of water between Newark Bay and Raritan Bay.

2.6   The East River

The East River is the conduit between NY Harbor at its southern end and Long Island Sound at its northern end (see Figure: 2.3). It is tidal strait and has no direct source of fresh water except sewage treatment plant effluents. *Geyer and Chant* [2003] reported that the tidal currents in the East River were among the strongest in the region because of a difference in the height and timing of the tide between Long Island Sound and NY Harbor. The flow in the East River fluctuates with the wind and was found to be weaker but more persistent than tidal currents. The salinity gradient in the East River was towards Long Island Sound due to its free connection with the Atlantic Ocean. They also reported that the strong tidal circulation in the East River results in well mixed water column at the Lower River, while stratified at the Upper River. *Blumberg and Pritchard*

[1997] investigated the volume flux through the East River which connects the Long Island Sound and the NY Harbor using a high-resolution estuarine model. This modeling study reported that the net long-term flux obtained from 18 months of model simulation was directed out of Long Island Sound and toward the NY Harbor. *NYDEP* [2003] reported that the tidal average in Western Long Island Sound is nearly 70% greater than that in NY Harbor, and the timing of high and low water occurs 3 hours later in the Harbor than Long Island Sound, which results in a tidal current of $O(2.0 \text{ m s}^{-1})$ in the East River, and can exceed to 3.0 m s^{-1} at Hell Gate, NY; where the East River confluence with the Harlem River.

Chapter 3

Surface Current Measurement Using High Frequency Radar

3.1 Introduction

Accurate measurement of ocean surface currents has been one of the more challenging endeavors in oceanography. The ocean surface exhibits high spatial and temporal variability due to various forcings of tides, river discharge, and surface meteorology. Conventional *in-situ* current measuring instruments such as ADCPs, S4 current meter, are capable of measuring the sub-surface Eulerian ocean currents, while surface drifters such as Argos (drouged/undrouged) measures the (sub-surface/surface) Lagrangian ocean currents. A surface drifter can only measure Lagrangian ocean currents with minimum accuracy due to its high dependence on the local wind shear. The dynamic sea state limits the ability of conventional *in-situ* current measuring instruments in obtaining a reasonably good surface current data set. Even the more advanced ADCPs can only measure ocean currents at the depth of measurement bin separated by few meters from the surface due to the sidelobe contamination. High frequency (HF) radar

system is a novel, land-based oceanographic tool capable of measuring ocean surface currents from the backscattered radar signal by ocean surface gravity waves. HF radar system works on the principle of Bragg scattering where the transmitted electromagnetic radio pulses were reflected by resonant ocean surface waves of one-half the incident radar wavelength. HF radar system consists of a transmitter antenna capable of transmitting high frequency (3 ~ 30 MHz) electromagnetic waves over electrically conductive ocean surface, and receiver antennas capable of capturing the signals backscattered by moving ocean surface due to waves and underlying currents. Using HF radar we can measure the spatial variations of near-surface ocean current field over a synoptic scale of O(200 km).

3.2   Review of High Frequency Radar Technology and its Applications

The ability to probe ocean surface currents from the resonant backscattered signals by ocean surface gravity waves was first documented by *Crombie* [1955]. The first-order (FO) Doppler peaks in the sea-echo Doppler spectra were due to Bragg scattering of HF radio pulses by the resonant ocean waves of one-half the incident radar wavelength. The actual relationship between the Doppler frequency shift and surface current was suggested by *Stewart and Joy* [1974], where small but finite Doppler frequency shift of the FO Doppler peaks were attributed to the underlying current flow. They developed a theoretical relationship between the average depth of HF radar measured surface currents and the HF radar transmitting frequency.

The theory of HF/very high frequency (VHF) propagation across the rough ocean surface and the interaction between HF/VHF radio pulses and the ocean surface was discussed by *Barrick* [1971]. The theory and analysis of the FO medium frequency (MF)/HF/VHF backscattered signals by ocean surface, where radio pulses propagating at grazing angles were intercepted by the rough ocean surface was studied by *Barrick* [1972]. Extensive studies on non-linear ocean surface gravity wave theories were done by *Barrick et al.* [1977], in which a general hydrodynamic solution was derived by extending Stokes original perturbation analysis for an arbitrary ocean surface wave field. The importance of measurement and analysis of the FO and second-order (SO) sea-echo Doppler spectra was reported by *Barrick* [1977], *Lipa* [1978], and a new methodology was developed by *Barrick* [1977] to extract the dominant wave parameters by analyzing HF radar sea-echo Doppler spectra.

The first compact HF radar system capable of measuring ocean surface currents was developed by *Barrick et al.* [1977]. This HF radar system utilized three-element collocated crossed-loop/monopole antennas and had greater advantages in ease of transportation and deployment in small, confined areas. This compact HF radar system was developed at the Wave Propagation Laboratory (WPL) of the National Oceanic and Atmospheric Administration (NOAA) and later became known as Coastal Ocean Dynamics Application Radar (CODAR). *Lipa and Barrick* [1983] developed an efficient method of least-squares to extract the surface current radial velocities from HF radar (CODAR) FO sea-echo Doppler spectra, and to compute the total vector field by combining the radial vectors measured by two different HF radar sites.

The correction procedure for the distorted antenna patterns of the CODAR system was reported by *Barrick and Lipa* [1986]. The distorted antenna patterns induce bearing errors and contaminate the radial data. This can be corrected by comparing the measured transponder signal on a different antenna channel with crossed-loop and monopole antenna patterns, where a boat with a transponder circled the receiver antenna at a constant radius.

The extraction of directional wave information from HF radar measurements was reported by *Barrick and Lipa* [1986]*, Lipa et al*. [2005] which showed how the HF radar system could be used to measure surface current fields and directional wave spectrum. The directional wave parameters were extracted from the SO Doppler spectrum using methods of integral inversion and fitting with a model of ocean wave spectrum [*Lipa et al*., 2005].

Barrick [2005] reported the influence of shallow water waves on the HF radar (CODAR) system which works with the underlying assumptions of linear wave theory and deep water condition. The shallow water effect highly influences the long-range CODAR systems (5 MHz), where the velocity error (deviation from the deep water velocity) was found to be less than 5 cm s^{-1} with depths greater than 13.2 m. While for standard-range CODAR systems (25 MHz), the velocity error was found to be less than 5 cm s^{-1} with depths greater than 2 m. A shallow water correction procedure was suggested where actual depths from the bathymetric charts were used for the computation of wave celerity at each radial location. This depth corrected wave celerity should be used rather than depth invariant deep water wave celerity in the frequency Doppler shift equation to

compute the surface current magnitude. A detailed discussion on the possible uncertainties in surface current velocities estimated using CODAR seasonde system was presented by *Lipa* [2003].

An important application of the HF radar system as a Tsunami warning system was originally reported by *Barrick* [1979] and later by *Lipa et al.* [2006]. HF radar system capable of measuring surface currents and wave fields can be used to detect the presence and magnitude of a Tsunami, by to and fro surface current variability due to orbital velocity of an approaching Tsunami wave. A good general overview of HF radar systems and a selection of results with respect to specific applications are presented in the *Special Issue on High Frequency Radars for Coastal Oceanography, The Oceanography Society* [1997].

3.3   Working Principle of High Frequency Radar

HF radar systems work on the principle of Bragg scattering by ocean surface gravity waves, in which HF radar transmitted signals of known wavelength are being scattered by moving ocean surface at a known resonant condition such that, the wavelength of scattering ocean waves will be equal to half of the transmitted radar wavelength. The resonant Bragg condition is given by

$$\lambda_{wave} = \frac{\lambda_{radar}}{2\cos(\theta)} = \frac{\lambda_{radar}}{2} \qquad\qquad (3.1)$$

where, θ is the grazing angle of HF radar which has a low value ($\sim 5^0$), hence $\cos(\theta) \approx 1$

λ_{radar} is the known wavelength of the HF radar transmit wave

λ_{wave} is the wave length of the resonant ocean surface wave

Using the resonant condition and the known transmitted wave length, the wavelength of the scattering ocean wave is obtained. The FO Doppler peaks in the sea-echo Doppler spectra due to Bragg scattering by ocean surface gravity waves are dominant with higher peaks than those due to other scattering surfaces. This Bragg scattering effect results in two discrete FO Doppler peaks in the sea-echo which can be precisely identified and its frequency determined. The Doppler frequency shift of the Bragg peak relative to the incident radar frequency is due to the ocean surface variations. The speed at which the ocean surface moves depends on the velocity of water and the velocity of the reflecting surface, which is the velocity of the resonant ocean surface wave. The HF radar system works on the underlying assumptions of linear wave theory and deep water conditions. The ocean surface wave celerity (velocity) at deep water condition according to the linear wave theory can be expressed as

$$C_o = \sqrt{\frac{g\lambda_{wave}}{2\pi}} \qquad (3.2)$$

where, g is the acceleration due to gravity (9.81 m s^{-2})

C_o is the deep water ocean wave celerity

In the absence of any surface current, the FO Doppler peaks are symmetric with respect to the Bragg frequency (f_b), offset from the origin given by

$$f_b = \pm \frac{2C_o}{\lambda_{radar}} \qquad\qquad (3.3)$$

Using (C_o) and the known transmitted radar wavelength (λ_{radar}), the contribution of the Doppler frequency shift (f_b) due to the resonant ocean surface wave is obtained. Any additional Doppler frequency shift (Δf) is attributed to the underlying currents upon which the ocean surface waves are riding. By measuring the additional Doppler frequency shift (Δf) from the sea-echo Doppler spectra, the radial component of the surface current can be computed.

$$\Delta f = \pm \frac{2V_r}{\lambda_{radar}} \qquad\qquad (3.4)$$

where, (V_r) denotes the radial component of the surface current, designated as positive when ocean waves moves toward the transmitting source and negative when waves move away from the source. A typical sea-echo Doppler spectrum is shown in Figure: 3.1.

The three parameters required to define a current vector in the ocean surface are the magnitude, direction, and range of the current vector. The magnitude of current vector is obtained by measuring the additional Doppler frequency shift (Δf). The direction (bearing) of the surface current is determined according to different approaches depending on the type of the HF radar system.

All HF radar systems are based on the principle of Bragg scattering by resonant ocean surface waves, and can be differentiated with respect to how the bearing is determined. Those are either beam-forming (BF) or direction-finding (DF) methods. For HF radar systems such as ocean Surface Current Radar (OSCR)
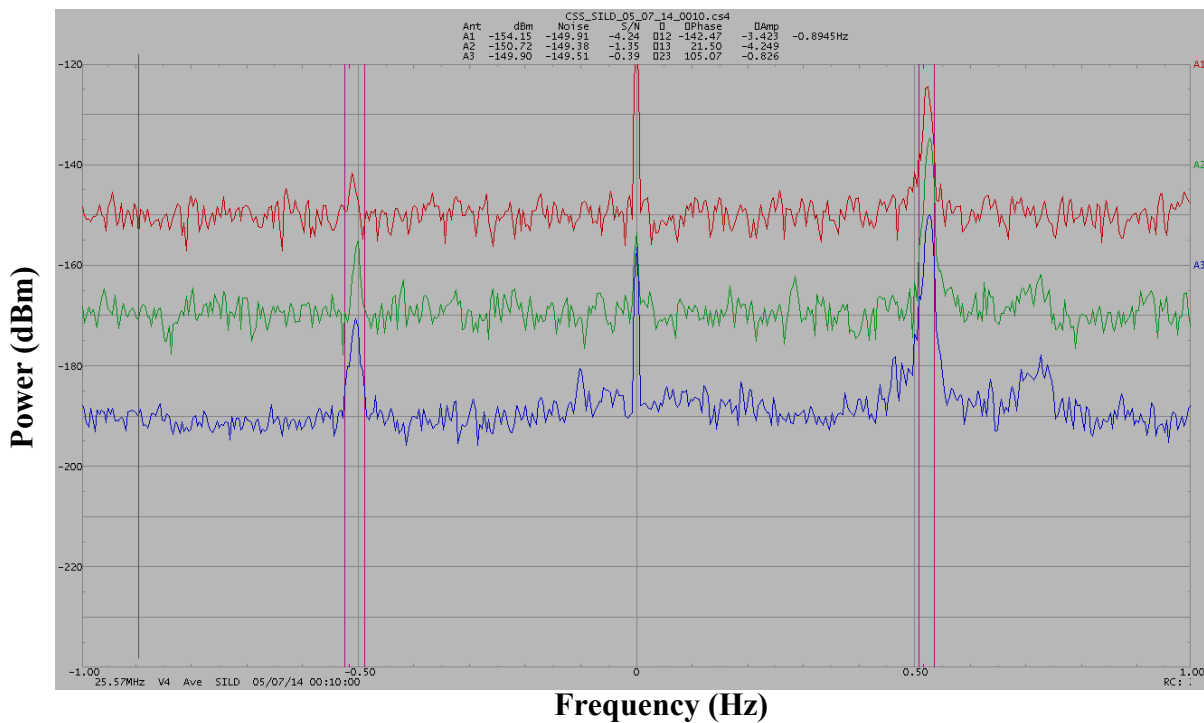
Figure: 3.1.   A typical HF radar (CODAR) sea-echo Doppler spectrum

[Loop 1 (red) & Loop 2 (green) and Monopole (blue) are

separated by 20 dBm].

(Marconi Company, U.K), WEllan RAdar (WERA) works with the BF technique, and consists of an array of receiver antennas [phased array system] along the beach real estate. The HF radar system employed in the present study the CODAR system, works on the DF algorithm. The CODAR system utilizes a single pole transmitter antenna and a compact system of collocated three-element receiver antennas (two orthogonal loops: loop-1 & loop–2, and a single omnidirectional monopole). A typical CODAR transmitter antenna and receiver antenna systems are shown in Figure: 3.2. The DF algorithm of the CODAR system is patented as MUltiple SIgnal Characterization (MUSIC) algorithm [*Schmidt,* 1986]. The basic idea of DF algorithm is to identify the bearings of the ocean patches having similar surface current magnitudes. The ratio of receiver signal strengths of the looped antennas (loop-1 & loop–2) gives the direction from which the scattered signal originated. The monopole antenna receives the same signal independent of the incoming direction, which is used to normalize the signals received by the looped antennas.

The range of the current vector is calculated by the time-lag between the transmitted and the received signals, and from the known speed of signal propagation. The CODAR system works with the frequency modulated (fm) signals, in which the frequency is linearly varying with respect to the time. Using the measured frequency difference between the transmitted and the received signals, the range of the target of HF radar system can be calculated. A higher frequency difference between the transmitted and the received signals represents a more distant target.

Transmitter antenna

Receiver antenna (Loop 1, loop 2, and monopole)

Figure: 3.2.   A typical HF radar (CODAR) antenna system.

[Acknowledgement: *http://marine.rutgers.edu/mrs/codar/pictures/SandyHook.html***]**

Surface currents measured using HF radar are near-surface and depth-averaged. The depth of influence is a function of the transmitting frequency of the HF radar system. The theoretical relationship between the depth of influence and the HF radar wave length [*Stewart and Joy,* 1974] is give by

$$d = (1/2k_{wave}) = (\lambda_{wave}/4\pi) = (\lambda_{radar}/8\pi) \tag{3.5}$$

where, d is the average depth of measurement

k_{wave} is the ocean wave-number $[k_{wave} = (2\pi/\lambda_{wave})]$

The quality and the range of HF radar data depends on the spectral characteristics of the sea-echo. The spectral quality of the sea-echo is dependent on the transmitted signal strength, which is a function of transmitting frequency and the seawater conductivity [*Shay et al.,* 2002]. The signal attenuation of the transmitted signal increases with increasing transmitting frequency. A higher range of O(200 km) is obtained for 5 MHz system and a lower range of O(10 km) for 45 MHz system. The conductivity of the seawater also plays an important role in the signal attenuation and the spectral quality of the sea-echo. The signal attenuation decreases with increasing sea water conductivity. This gives a larger range for saltier conditions and a smaller range for fresher water. The HF radar data quality also depends on the sea state, where the transmitted radio pulses were backscattered by resonant ocean surface waves. During extreme weather events and rough sea states, the significant wave height increases and the spectral quality of the sea-echo decreases.

3.4   Surface Current Measurement

A single HF radar site only measures the radial component of the surface current, in which the Bragg scattering is predominant. HF radar system measures the radial component of the surface current with respect to the spatial domain defined by a polar coordinate (r, θ) system. The spatial domain is divided into annular bins called range cells ($\Delta r \approx 1.5 km$, for standard-range CODAR system) extending circularly from the HF radar site as the origin, and the azimuth ranges from $0^0 \sim 360^0$, incremented at every $5^0 (\Delta \theta \approx 5^0)$. HF radar system measures the magnitude, direction, and the range of the radial current vector with respect to polar grid defined by the range cell and the azimuth. The CODAR system uses the MUSIC algorithm to obtain the direction of arrival of the signal, using either ideal or measured antenna patterns. Individual standard-range CODAR site is operated at 24.7 MHz with a sweep width of 100 KHz and a sweep rate of 2 Hz, giving an average range of 40 km and a range resolution of 1.5 km. Cross spectra files are a range and Doppler matrix of signal levels and phases received from the cross loop antennas. Each cross spectra file covers a specific period of time centered on a time stamp. The raw cross spectra were written every 256 seconds using a 512-point fast Fourier transform (FFT) and used to create 15 minute averaged files with an output every 10 minutes creating a 2.5 minute overlap between the previous and following cross spectra. The cross spectra files are processed to obtain the radial vectors and these 10 minute radial files were then averaged into 75 minute files with an output at every 30 minutes. This standard-range CODAR system resolves currents to 2.31 cm s^{-1} [*Kohut et*

al., 2006]. The total vector field of the surface currents is computed by combining the radial vectors measured by individual HF radar sites. This computation of the total vector field from the radial vectors follows a method of least squares suggested by *Lipa and Barrick* [1983]. A minimum of two or more radial vectors measured by the spatially separated HF radar sites, with at least one radial vector from each of the two different HF radar sites are combined to obtain the total surface current field. A flow diagram for the HF radar system representing the process of obtaining radial currents from the sea-echo Doppler spectra is shown in Figure: 3.3 and a typical radial current plot measured using a standard-range CODAR system is shown in Figure: 3.4.
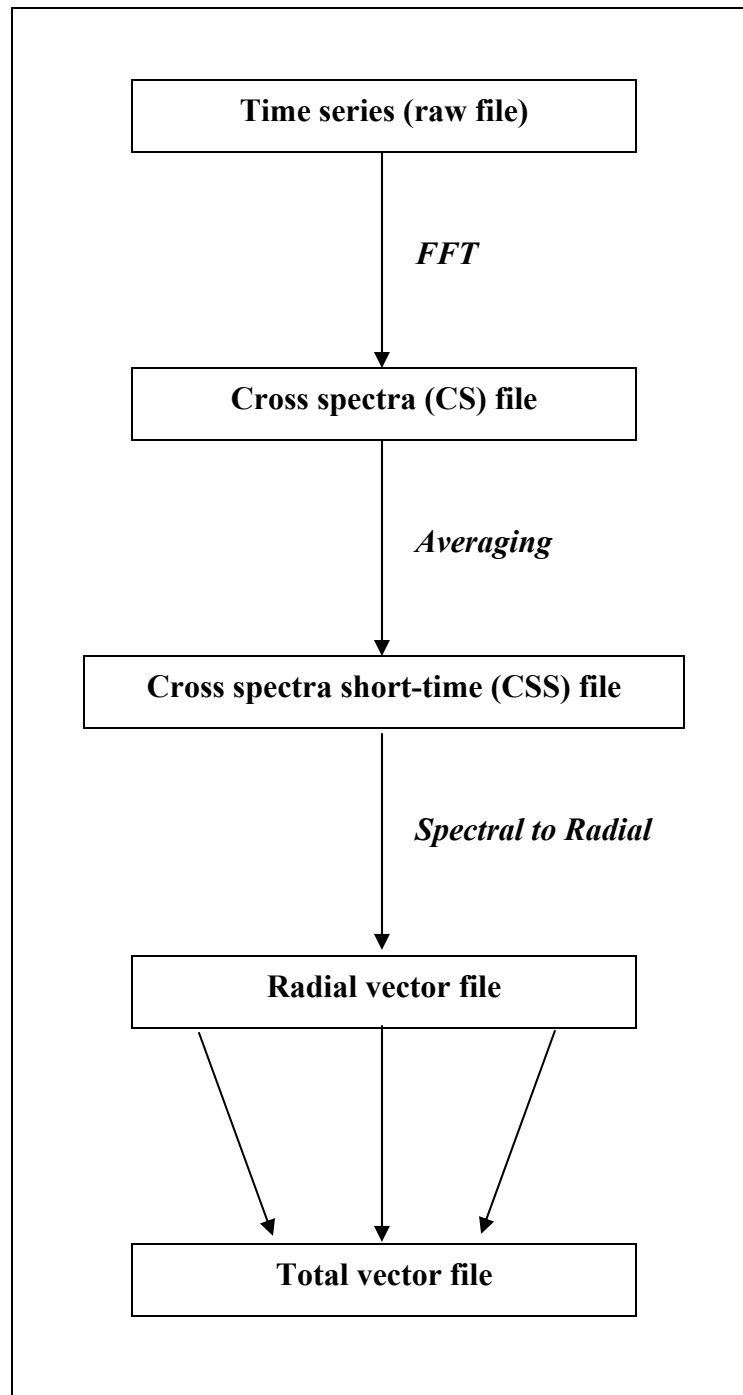
Figure: 3.3.   Flow diagram showing HF radar (CODAR) data processing.
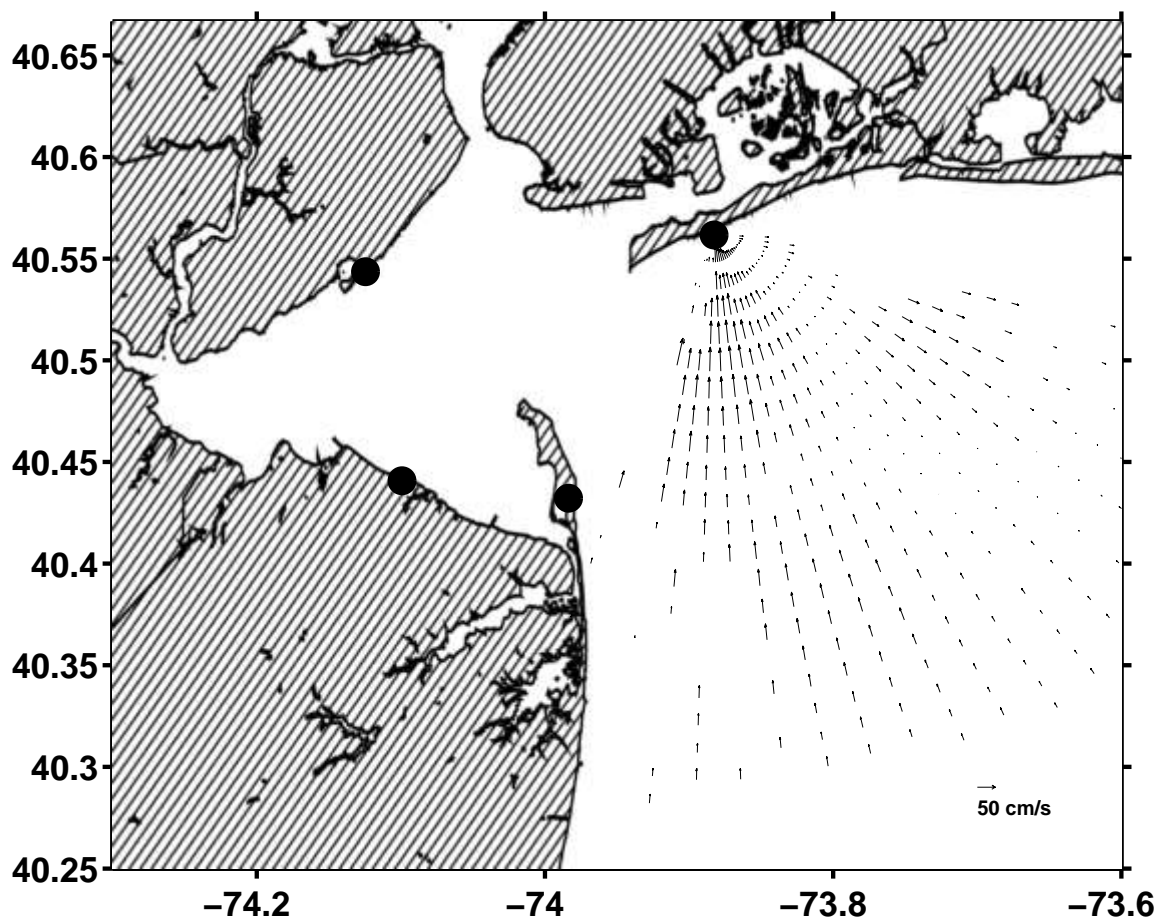
Figure: 3.4.   A typical HF radar radial vector plot (03/14/2007 - 19:30).

3.5   High Frequency Radar Network

A surface current observation system based on HF radar has been constructed for Raritan Bay, NJ; and the NYB Apex. The HF radar network employed in the present study consists of four monostatic standard-range CODAR systems, located at Sandy Hook, NJ [HOSR: owned and operated by Rutgers University]; Breezy Point, NY [BRZY: owned and operated by Rutgers University]; Bayshore Water Front Park, NJ [BSWP: owned and operated by NOAA]; and on the south shore of Staten Island, NY [SILD: owned and operated by Stevens Institute of Technology (SIT)]. A detailed description of the HF radar (CODAR) network for the New Jersey Shelf Observing System (NJSOS) can be found in *Kohut et al.* [2002], *Kohut et al.* [2001], *Kohut and Glenn* [2003]. The CODAR network runs from the Gulf of Maine to Cape Hatteras, providing real-time surface current patterns for the NYB. The CODAR network comprised of long-range, standard-range and medium-range seasonde systems, which were operated in monostatic as well as bistatic modes together forming the first nested multi-static HF radar array for measuring surface currents. The HF radar sites and the present study domain are shown in Figure: 3.5 and the site specifications of the four HF radar systems are tabulated and shown in Table: 3.1. The radial vector files generated by the four HF radar sites at every 30 minutes were combined with respect to a pre-defined surface grid using the method of least squares [*Lipa and Barrick* 1983] to generate the total vector field. A typical total vector plot for the present study domain is shown in Figure: 3.6.
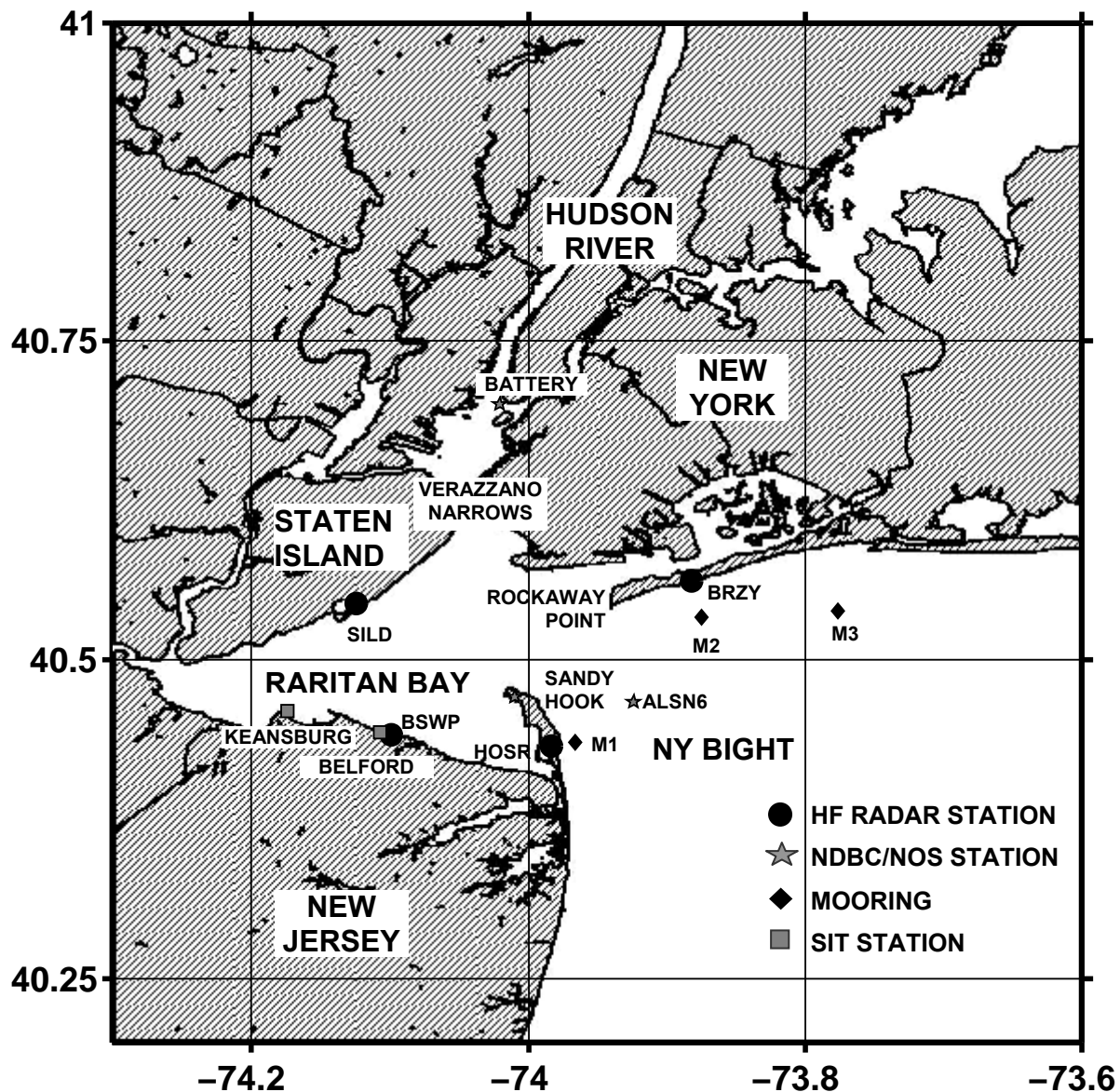
Figure: 3.5. HF radar network for the present study domain (black circle represents four monostatic HF radar stations, black diamond represents three mooring stations, gray stars represent NDBC/NOS stations, and gray square represents Stevens stations)

Table: 3.1.   Specifications of the standard-range HF radar network.

Site No	1	2	3	4
Deployment Site	*Staten Island (SILD)*	*Sandy Hook (HOSR)*	*Breezy Point (BRZY)*	*Bay Shore Water Front Park (BSWP)*
HF radar Type	*CODAR Seasonde Standard-Range*	*CODAR Seasonde Standard-Range*	*CODAR Seasonde Standard-Range*	*CODAR Seasonde Standard-Range*
Collaborator	*Stevens Institute*	*Rutgers University*	*Rutgers University*	*NOAA*
Latitude	*40.543617 N*	*40.432200 N*	*40.561683 N*	*40.440783 N*
Longitude	*74.124517 W*	*73.983650 W*	*73.882650 W*	*74.099233 W*
Transmitting Frequency	*24.65 MHz*	*24.65 MHz*	*24.65 MHz*	*24.65 MHz*
Resonant Bragg Condition	$\lambda_{radar} = 12\ m$ $\lambda_{wave} = 6\ m$	$\lambda_{radar} = 12\ m$ $\lambda_{wave} = 6\ m$	$\lambda_{radar} = 12\ m$ $\lambda_{wave} = 6\ m$	$\lambda_{radar} = 12\ m$ $\lambda_{wave} = 6\ m$
Grazing angle	5^0	5^0	5^0	5^0
Transmitted Power	*60 W*	*60 W*	*60 W*	*60 W*
Received Power	*5W - 7 W*	*5W - 7 W*	*5W - 7 W*	*5W - 7 W*
Sweep Rate	*2 Hz*	*2 Hz*	*2 Hz*	*2 Hz*
Sweep Width	*100 KHz*	*100 KHz*	*100 KHz*	*100 KHz*
Radial Range	*40 km*	*40 km*	*40 km*	*40 km*
Radial Coverage	$0^0 - 360^0$	$0^0 - 360^0$	$0^0 - 360^0$	$0^0 - 360^0$
Radial Bin	*1.5 km*	*1.5 km*	*1.5 km*	*1.5 km*
Radial Bearing Increment	5^0	5^0	5^0	5^0
Radial Interpolation for Gaps	*No Interpolation*	15^0 *Gaussian beam window*	15^0 *Gaussian beam window*	*No Interpolation*
Average Depth of Measurement	*0.5 m*	*0.5 m*	*0.5 m*	*0.5 m*
Radial Current Threshold	$1.5\ m\ s^{-1}$	$1.5\ m\ s^{-1}$	$1.5\ m\ s^{-1}$	$1.5\ m\ s^{-1}$
Total Current Threshold	$1.5\ m\ s^{-1}$			
GDOP Threshold	$1.5\ cm\ s^{-1}$			
Minimum number of Radials combined	*3*			
Minimum number of CODAR sites combined	*2*			
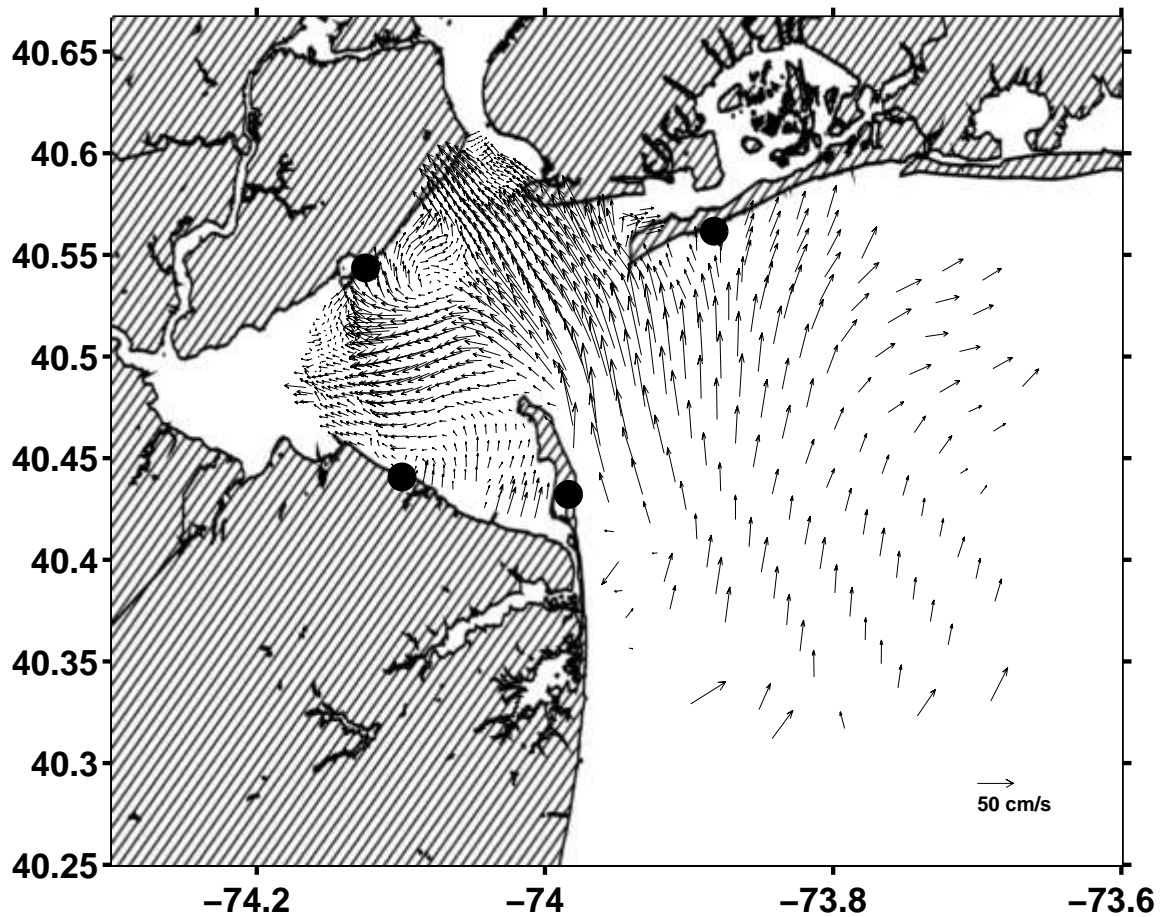
Figure: 3.6.   A typical HF radar total vector plot (03/14/2007 - 19:30).

HF radar network used in the present study has good coverage of surface currents inside NY Harbor, Raritan Bay, and the NYB Apex, with a temporal resolution of 30 minutes. In order to improve the reliability of the HF radar data, a temporal data coverage threshold value of greater than 50% were used in the present study. The HF radar data footprint for the period of January - April 2007 is shown in Figure: 3.7. The geometric dilution of precision (GDOP) is defined as the spatial error associated with geometric combination of the radial vectors [*Chapman et al.,* 1997]. The average GDOP error distribution of the present HF radar network for the period of January - April 2007 is shown in Figure: 3.8. The GDOP error distribution plot indicates an increase in the error with the distance from the HF radar stations, and along the baseline (line connecting the Staten Island and Bayshore Water Front Park sites). In order to improve the HF radar data quality, the present study used a GDOP error threshold value of lesser than 1.5 cm s^{-1} (see Table: 3.1). The pre-defined surface grid used for the total vector field computation is the NYHOPS model grid, and the radial current and total current magnitudes were limited to 1.5 m s^{-1} (see Table: 3.1).
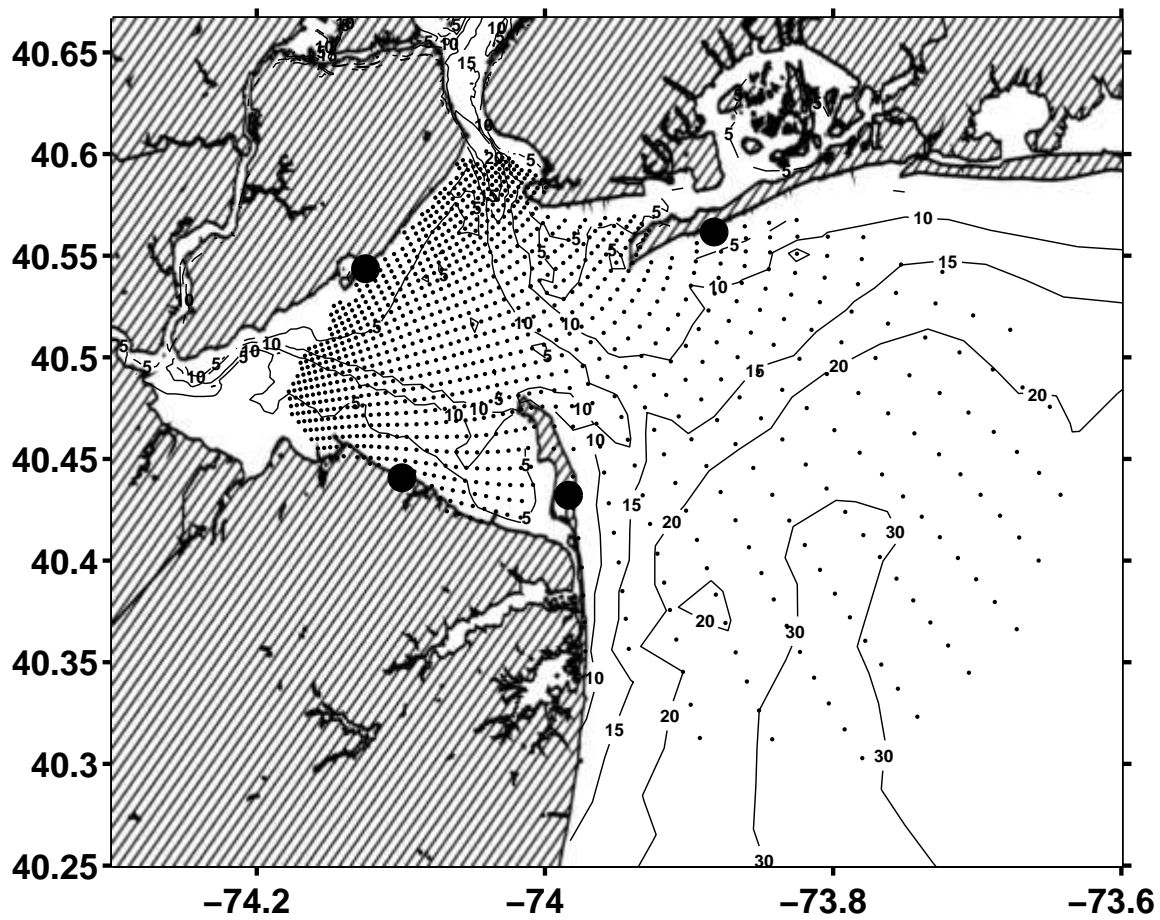
Figure: 3.7.   HF radar data foot print (depth contours in meters)

(Temporal coverage > 50 % for January - April 2007).
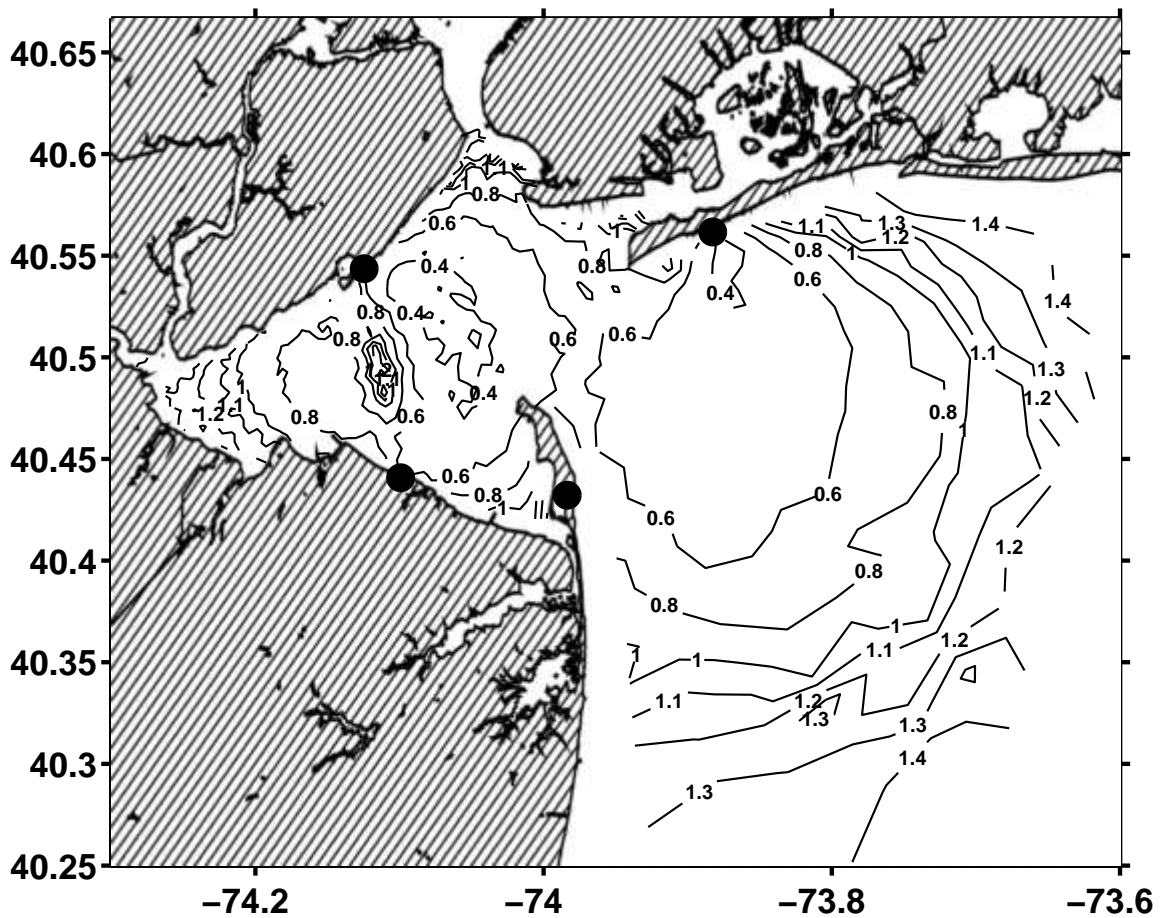
Figure: 3.8.   Average distribution of the Geometric Dilution Of Precision

(GDOP) Error

(Threshold value < 1.5 cm s^{-1} for January - April 2007).

3.6   Sensitivity of CODAR First-Order Doppler Region Settings

The empirical determination of the frequencies of FO Doppler peaks which defines the Bragg scatterance is important in the CODAR spectral analysis. The FO Doppler peaks are separated from the higher-order Doppler peaks by well defined minima which are referred as "nulls" [*CODAR, Inc.* 2004]. The FO sea-echo represents the energy contribution of ocean surface currents, while the SO sea-echo represents the energy contribution of ocean surface waves. A typical spectral plot representing FO and SO Doppler region, and the nulls are shown in Figure: 3.9. The FO Doppler peak settings are critical in the accurate measurement of surface current vectors. A wider FO setting will result in erroneous current vectors due to inclusion of higher-order spectral energy while a narrower FO setting will result in the elimination of good data. The FO empirical settings of the nulls are highly sensitive to the oceanographic circulation at a particular site. Occurrence of extremely strong currents will result in the spreading of FO region over the surrounding higher-order spectrum. The FO Doppler settings of the CODAR need to be precisely defined with a wider setting in tidally-dominated regions in order to capture the strong tidal currents. A typical spectral plot showing the spreading of FO region over the higher-order spectrum is provided in Figure: 3.10.

The standard-range HF radar network used in the present study provides good coverage for surface currents in the NY Harbor, Raritan Bay, and the NYB Apex. The hydrodynamic circulation in the present study domain of the NYB Apex is dominated by
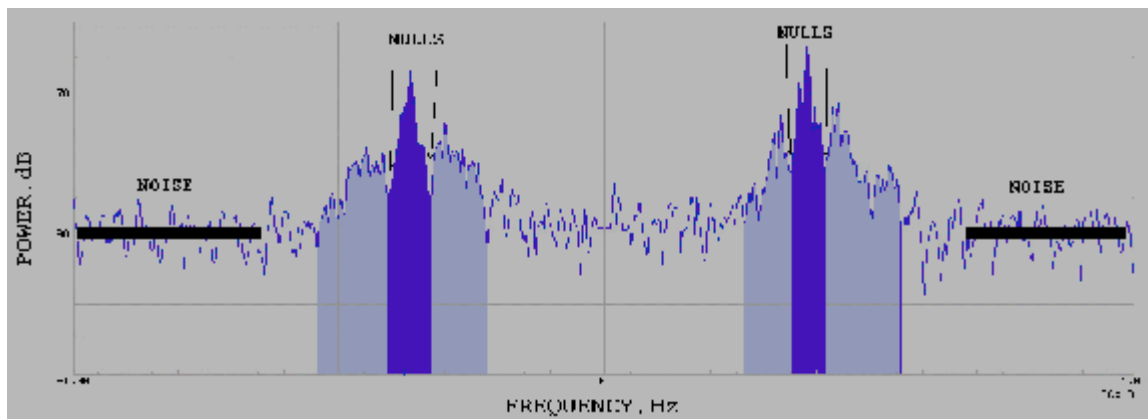
Figure: 3.9. **A typical sea-echo showing first-order and second-order Doppler regions [*First-order setting document, CODAR, Inc.* 2004].**
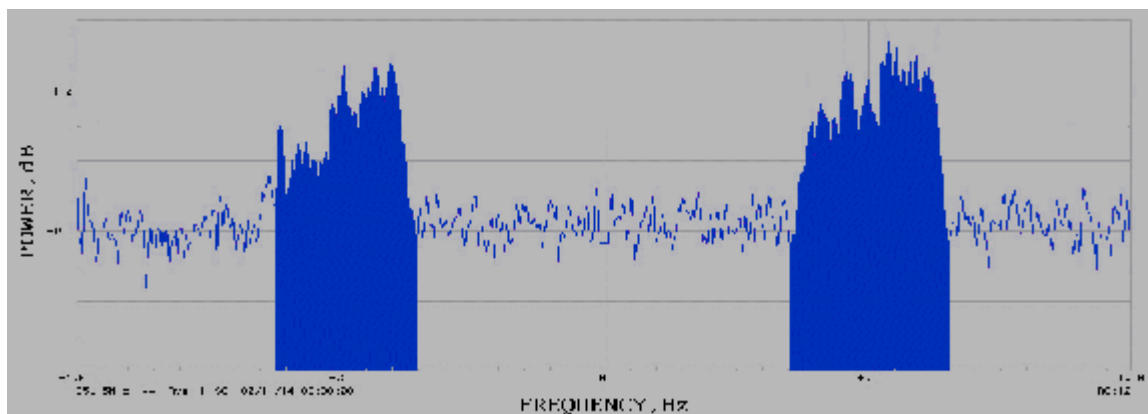
Figure: 3.10. **A typical sea-echo showing spreading of first-order spectrum due to extremely strong currents [*First-order setting document, CODAR, Inc.* 2004].**

tides, fresh water outflow from Hudson River and Raritan River, and surface winds. Out of the four CODAR systems, two of them; Staten Island (SILD) and Bayshore Water Front Park (BSWP) overlooks at extremely strong tidal currents of $O(1 \sim 2 \text{ m s}^{-1})$ at the mouth of the NY/NJ Harbor Estuary [Sandy Hook - Rockaway Point (SHRP) transect], and at the Verazzano Narrows. The SHRP transect falls at the 10th range cell from SILD site and the strong tidal currents across the SHRP transect introduces spreading of the FO Doppler spectrum. Similarly, the Verazzano Narrows falls at the 12th range cell from BSWP site and the strong tidal currents across the Verazzano Narrows introduces spreading of the FO Doppler spectrum.

The bathymetric features of deeper channels as well as the geographic formations of the SHRP transect and the Verazzano Narrows drives stronger tidal currents normal to the cross-sections. These strong tidal current patterns at the SHRP transect and the Verazzano Narrows get intensified during ebb tide when the Hudson River flows out as a jet into the Atlantic Ocean. Since the FO settings for the CODAR site remains the same for all range cells, SILD site and BSWP site fails to capture these strong tidal currents across the SHRP transect and the Verazzano Narrows, occurring only at a particular range cell surrounded by range cells representing weaker currents in Raritan Bay.

The total vector field computed by combining the radial vectors from the four CODAR sites (SILD, BSWP, BRZY, HOSR) initially represented an unusual flow pattern at the SHRP transect as shown in Figure: 3.11. The CODAR surface currents near the mouth of the NY/NJ Harbor Estuary were directed along the SHRP transect rather than flowing normal to it. This unusual flow pattern of the CODAR currents at the SHRP

47
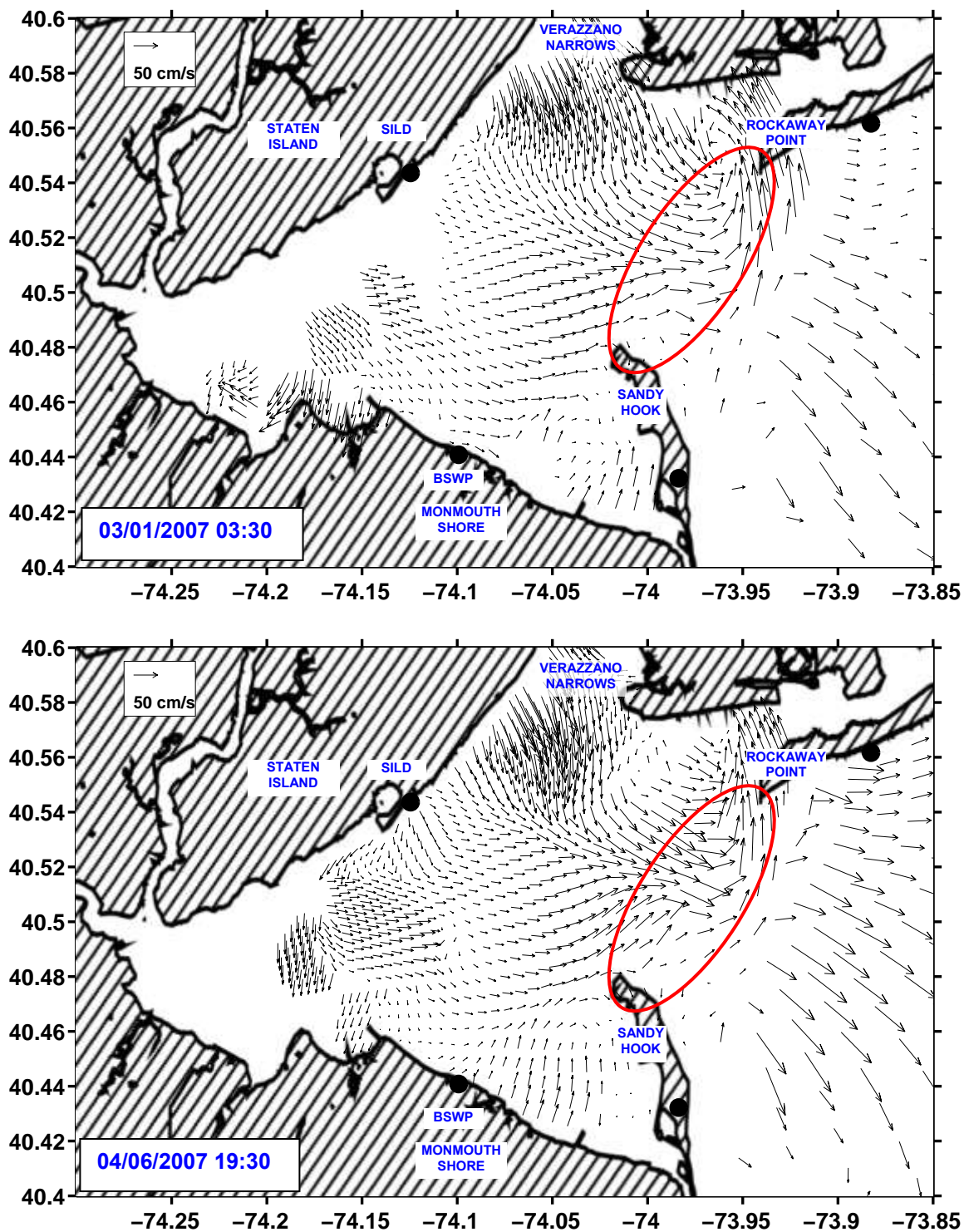
Figure: 3.11. Uncorrected CODAR total vector plots showing unusual flow pattern at the Sandy Hook – Rockaway Point transect.

transect are dominant during strong ebb tides. This peculiar CODAR current pattern can be due to the elimination of good data near the mouth of the NY/NJ Harbor Estuary, measured by the SILD site, owing to the spreading of the FO Doppler spectrum during strong ebb tidal currents. The ebb flow problem can also be related to the CODARs limited capability of resolving wave-current interaction where the ebb flow from the Hudson River Estuary interacts with incoming waves from the Atlantic Ocean.

An extensive comparison study of ocean model simulations and NOS observations in the NY/NJ Harbor Estuary and the NYB Apex by *Oey et al.* [1985b] reported a strong tidal current of $O(1.0 \text{ m s}^{-1})$ at the SHRP transect and the Verazzano Narrows, oriented normal to the cross-section. The locations of NOS [*Oey et al.,* 1985b] stations are shown in Figure: 3.12. A time-series comparison of currents normal to the SHRP transect obtained using CODAR at NOSO3 location [time: 03/17/2007 – 03/27/2007, average depth: 0.5 m] and NOSO3 [*Oey et al.,* 1985b] observation [time: 08/23/1980 – 09/02/1980, average depth: 5.5 m] for the spring tide is shown in Figure: 3.13. A similar comparison of CODAR currents at NOSO5 location [time: 03/17/2007 – 03/27/2007, average depth: 0.5 m] and NOSO5 [*Oey et al.,* 1985b] observation [time: 08/23/1980 – 09/02/1980, average depth: 4.6 m] for the spring tide is shown in Figure: 3.14. The CODAR current fails to represent a stronger outflow across the mouth of the NY/NJ Harbor Estuary at both the locations [NOSO3 and NOSO5] as indicated by the NOS observations [*Oey et al.,* 1985b].
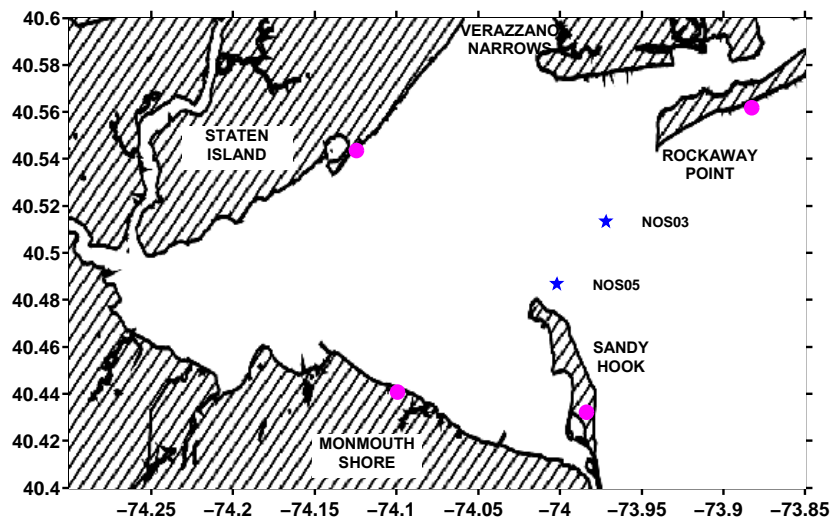
Figure: 3.12. Locations of NOS observations [*Oey et al.*, 1985b].
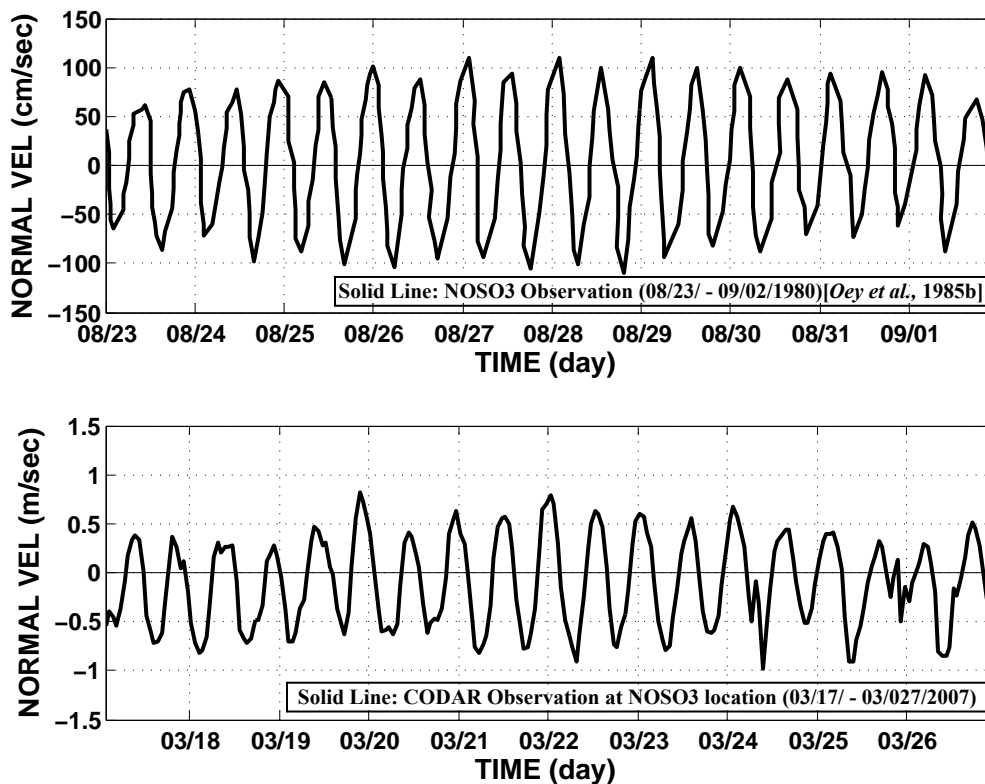
Figure: 3.13. Time-series comparison at NOSO3 location (SHRP transect)
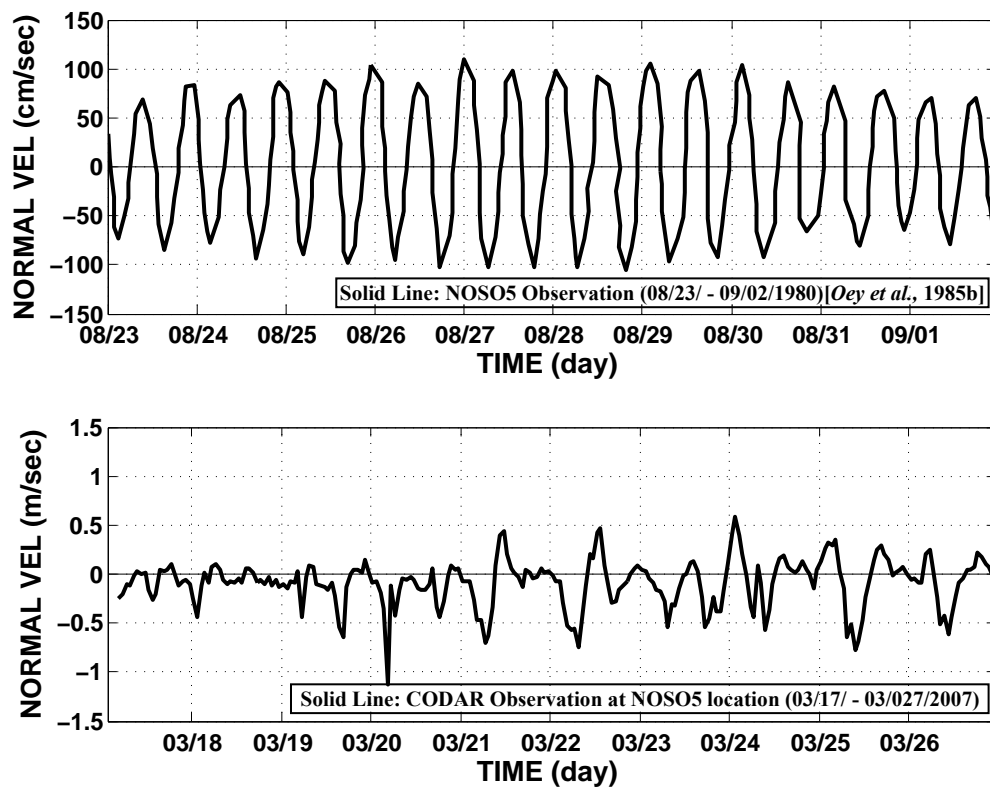
[*Oey et al.*, 1985b].

Figure: 3.14. Time-series comparison at NOSO5 location (SHRP transect)

[*Oey et al.*, 1985b].

A tidal analysis has been performed for the CODAR surface currents as well as NYHOPS model (see Chapter 5 for the NYHOPS model) surface currents of daily hindcasts for a period of 120 days (2nd March 2007 – 29th June, 2007). The tidal analysis is performed using MATLAB T_Tide toolbox [*Pawlowicz et al.,* 2002] and tidal ellipses for the predominant M_2 tidal constituent are plotted for the NYB Apex domain for both CODAR currents and NYHOPS model surface currents. The M_2 tidal ellipses for CODAR and NYHOPS are shown in Figure: 3.15. Tidal ellipses were plotted only for selected locations to improve figure clarity. The tidal ellipses for CODAR surface currents represents weaker amplitude of $O(0.6$ m s$^{-1})$ at the SHRP transect and the Verazzano Narrows, and mostly oriented in the east-west direction. The M_2 tidal ellipses for the NYHOPS model hindcasts represents stronger tidal amplitude of $O(1 \sim 2$ m s$^{-1})$ and oriented normal to the SHRP transect and the Verazzano Narrows.

The CODAR surface currents near the mouth of the NY/NJ Harbor Estuary were found to be weaker than the earlier observational findings [*Oey et al.,* 1985b], and oriented mostly along the SHRP transect. This can be due to the elimination of good data near the mouth of the NY/NJ Harbor Estuary, measured by the SILD site. This suggests the need of a more precise FO Doppler region setting for the SILD and BSWP CODAR sites. The sensitivity of the FO Doppler region settings for SILD and BSWP CODAR sites were not further investigated in the present research. Surface currents measured using present HF radar network at the corridor connecting the SHRP transect and the Verazzano Narrows WERE NOT considered for the assimilation experiments into the NYHOPS model, which are discussed in the Chapters 8 and 9 of this thesis.
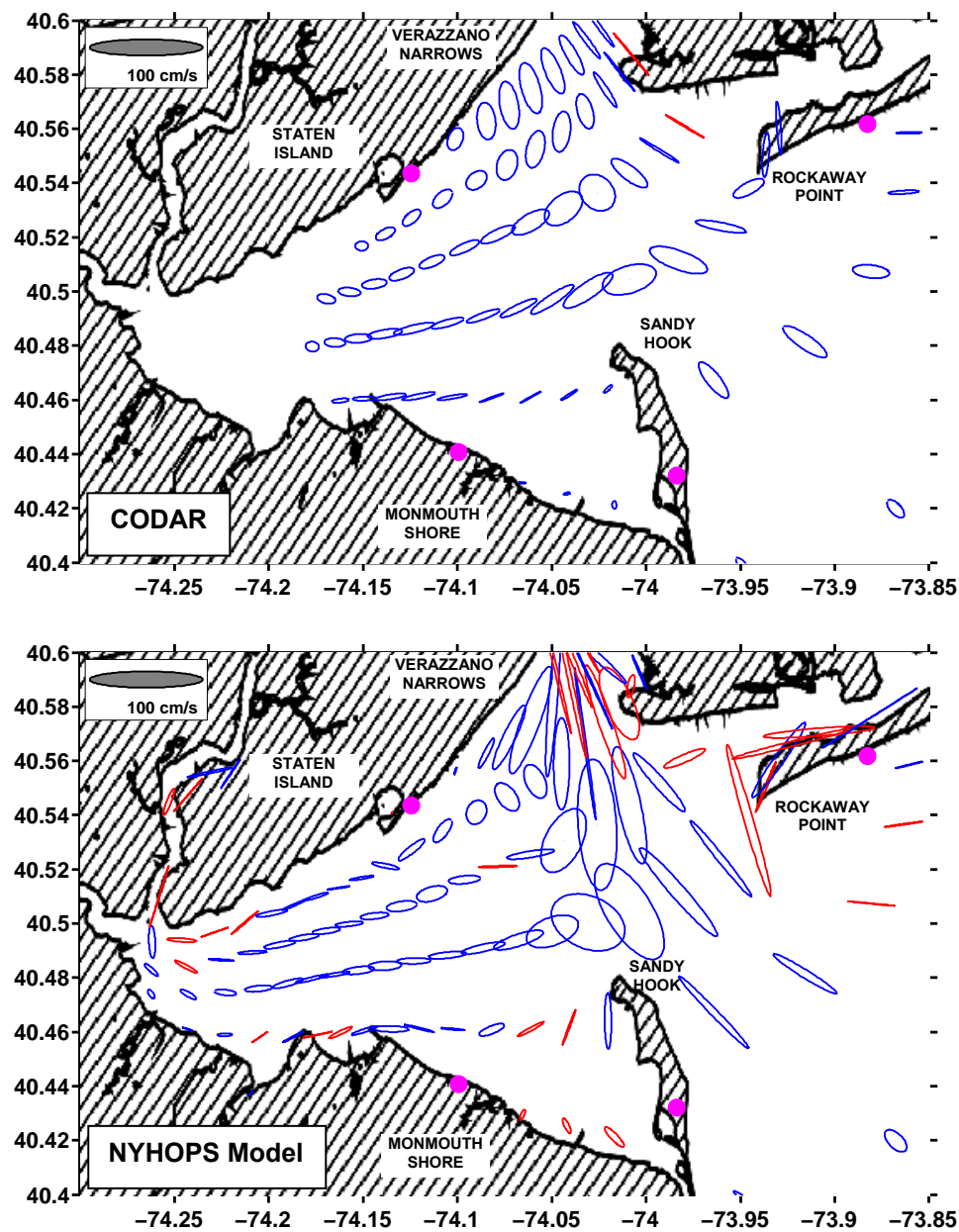
Figure: 3.15. Tidal ellipses (*M₂*) for CODAR surface currents (top) and NYHOPS daily hindcast surface currents (bottom) for the period of March – June, 2007. [Blue ellipses: clockwise component, red ellipses: counter-clockwise components].

3.7 Surface Current Circulation in Raritan Bay

The mean surface current circulation in Raritan Bay is obtained from the radial surface currents measured using HF radar systems located at Staten Island (SILD) and Bayshore Water Front Park (BSWP). The radial surface current data for the two sites were available for the period of January – June, 2007. HF radar radial currents from SILD and BSWP sites were combined using method of least squares [*Lipa and Barrick* 1983] with respect to NYHOPS model surface grid. The mean surface current field obtained from the HF radar observations for the period of spring 2007 (January – March) and summer 2007 (April – June) is shown in Figure: 3.16. This figure shows a mean flow ranges from $0 – 0.15$ m s^{-1} inside Raritan Bay. An anti-cyclonic eddy is observed inside Raritan Bay and this eddy feature is more prominent during summer 2007 than spring 2007. Tidal analysis was performed for the HF radar surface currents for the period of January – June, 2007. The tidal analysis was performed using MATLAB T_Tide toolbox [*Pawlowicz et al.,* 2002], in which five major tidal constituents [K_1, O_1, M_2, S_2, N_2], and were considered. Tidal ellipses for the predominant M_2 tidal constituent for the HF radar data were plotted and are shown in Figure: 3.17. Tidal ellipses were plotted only for selected locations to improve figure clarity. The tidal ellipses inside Raritan Bay are mostly oriented in the east-west direction following the Raritan channel and show a clockwise sense of rotation. The tidal ellipses shows a magnitude of ~ 0.2 m s^{-1} inside Raritan Bay and increases to a magnitude of ~ 0.5 m s^{-1} near the Verazzano narrows and near the SHRP transact.
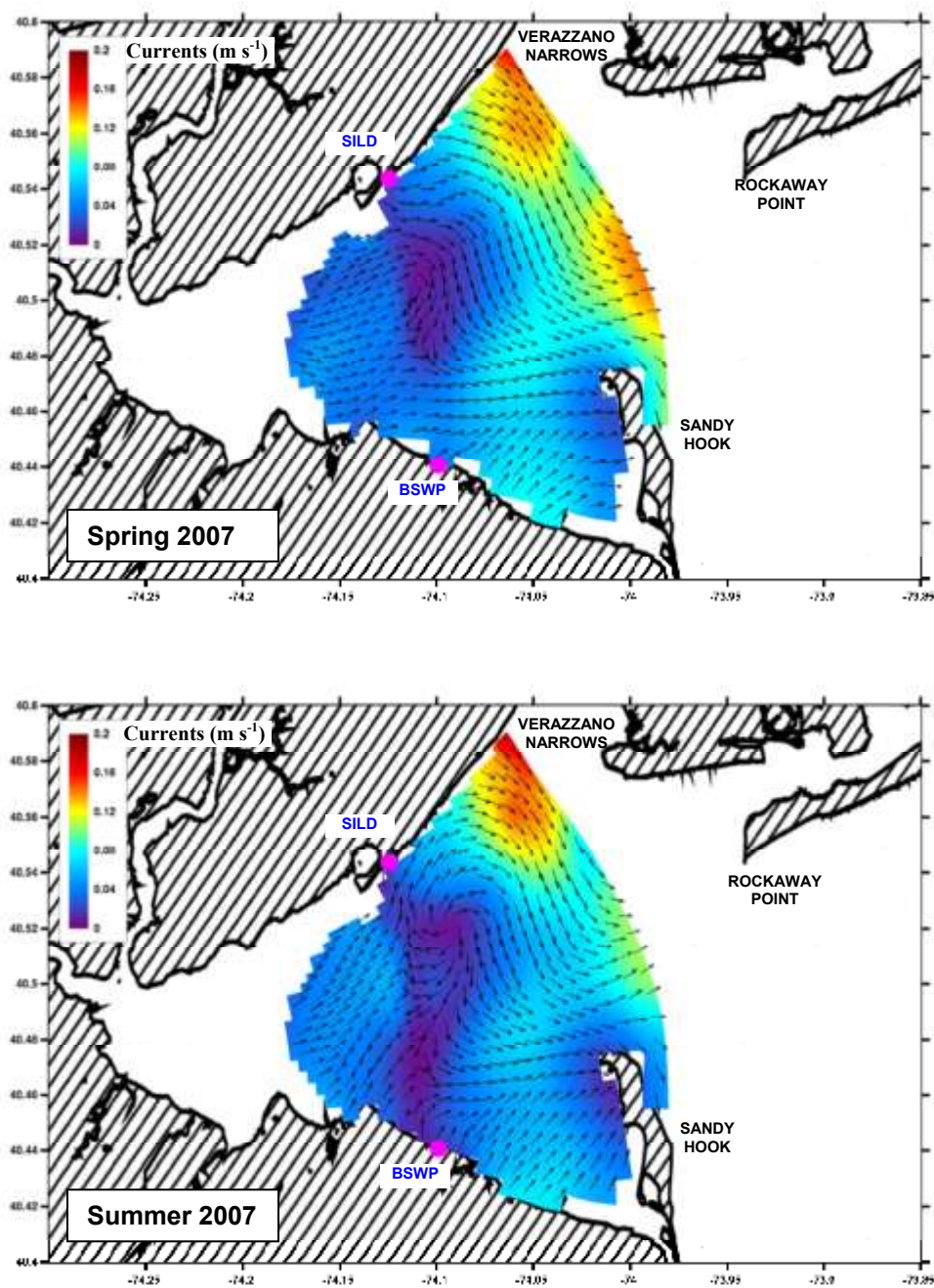
Figure: 3.16. Mean surface currents in Raritan Bay from HF radar for spring 2007: January – March (top) and summer 2007: April – June (bottom).
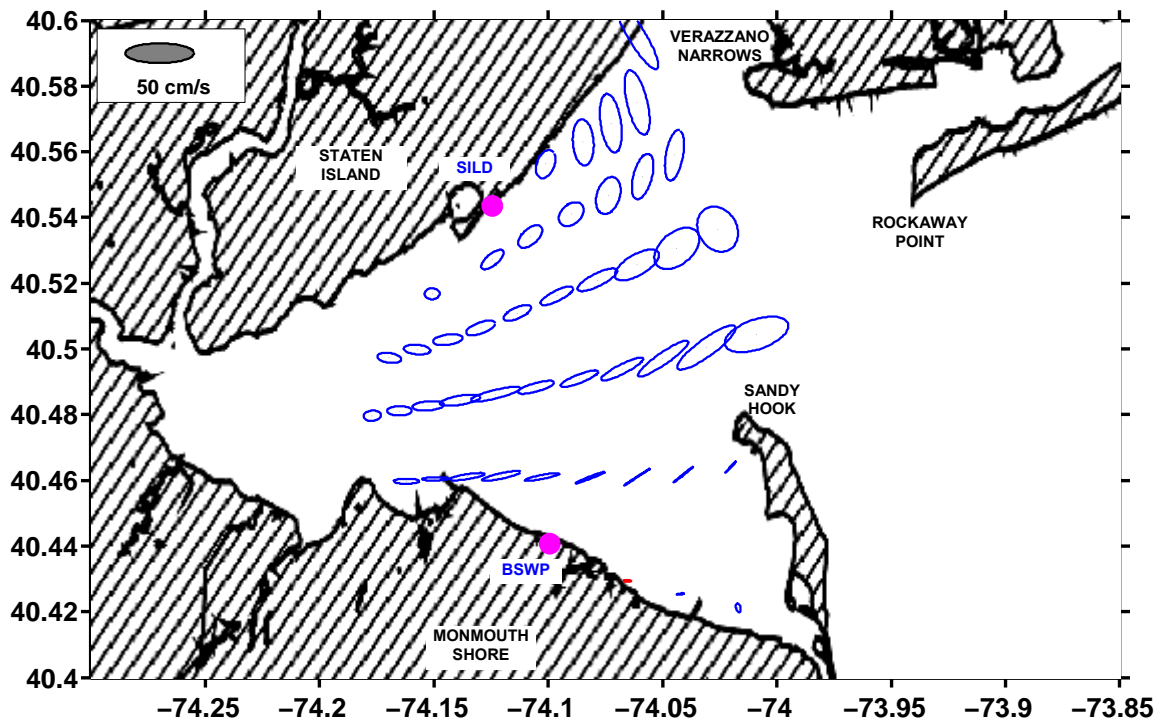
Figure: 3.17. Tidal ellipses (M_2) for HF radar surface currents in Raritan Bay for the period of January – June, 2007. [Blue ellipses: clockwise component, red ellipses: counter-clockwise components].

Chapter 4

Validation of High Frequency Radar Data

4.1 Introduction

The application of HF radar technology to remotely measure ocean surface variations has evolved over the past fifty years. The HF radar system has received considerable attention over the last two decades and wider acceptance by the oceanographic community as an efficient instrument for measuring near-surface ocean currents. Growing awareness of surface current mapping technique using HF radar and the increasing applications of real-time surface current maps makes HF radar an essential component of regional ocean observing systems. Since HF radar is a novel land based instrument measuring highly dynamic near-surface ocean flow it is important to validate surface currents measured using HF radar in order to provide a perspective of what is being measured, and how accurate are the measurements.

The measurement of near-surface currents is difficult due to the randomness of sea surface. The conventional current measuring instruments such as ADCP are capable of obtaining subsurface point measurements of currents which are averaged over the depth of measurement bin, throughout the water column. HF radar system is capable of measuring ocean surface currents which are spatially averaged over an ocean surface patch of $O(1 \sim 4 \text{ km}^2)$ and near-surface depth averaged with a depth of influence of about 0.5 m (for standard-range 24.7 MHz CODAR system). A direct comparison between HF radar measured surface current and *in-situ* surface current observation is rather difficult due to the lack of instrument capable of measuring spatial and temporal variations of surface currents. A comparison study between HF radar measured surface currents and subsurface ADCP current observations will provide a general trend in the flow pattern, depth dependence of the flow, and the vertical shear in the near-surface water column.

4.2   Review of Studies on the Validation of High Frequency Radar Data

The review of earlier studies on the validation studies of HF radar data with *in-situ* current measurements are summarized and presented in the Table: 4.1.

Table: 4.1.   Review of previous HF radar data validation studies.

Title	Salient Conclusions
Paduan, J.D. and L. K. Rosenfeld [1996]	• Comparison of CODAR measurements with moored ADCP data, wind observations, vessel-mounted ADCP data, satellite surface temperature imagery, and surface drifter velocities. • Comparison of filtered CODAR data and ADCP data yielded an *rms* speed differences of O(6 - 11 cm s^{-1}) and *rms* direction differences of 51^0. • Comparison of unfiltered CODAR data and drifter data yielded an *rms* speed differences of O(10 - 17 cm s^{-1}) and *rms* direction differences of 64^0. • Accuracy of CODAR measurement was less than 7 cm s^{-1} for about 50% of the time under the assumption of error-free *in-situ* measurements.
Chapman, R. D., and H. C. Graber [1997]	• Comparison of OSCR measurements with vessel-mounted sensors. • Described the predominant sources of the error in the different type of measurements and its spatial variability. • Comparison study yielded an upper bound of accuracy of O(7 - 8 cm s^{-1}) for the OSCR radial currents and *rms* differences of O(9 - 16 cm s^{-1}).
Graber et al. [1997]	• Validation of OSCR data with near-surface moored current measurements. • Analysis of numerous sources of the errors in the measurements. • Detailed analysis of the contribution of various geophysical processes like Ekman Drift, Stokes Drift, and baroclinicity in the measured differences between OSCR surface currents and near-surface moored current measurements. • Error sources of instrument noise, collocation and concurrence differences, and geophysical processes contributed 40% - 60% of the observed *rms* differences. • Comparison of OSCR data and *in-situ* current measurements yielded an *rms* speed differences of O(11 - 20 cm s^{-1}) and averaged direction differences of O(11^0 - 25^0).

Chapman et al. [1997]	• Comparison study of OSCR data with drifter and ADCP data.
	• An *rms* difference of O(8 - 15 cm s^{-1}) was observed between OSCR data and ship-mounted ADCP measurements.
	• A detailed analysis of the Geometric Dilution of Precision (GDOP) error, which is defined as the error associated with the geometric combination of the radial vectors for the estimation of the total vector field.
Emery et al. [2004]	• A comparison study of CODAR radial currents with the mooring data.
	• Comparison study yielded an *rms* speed difference of O(7 - 19 cm s^{-1}) and r^2 value of O(0.39 - 0.77).
	• Spectral analysis yielded high coherence during lower frequencies than higher frequencies.
Kaplan et al. [2005]	• A comparison study of CODAR observations with ADCP and drifter data.
	• The comparison study yielded an *rms* difference of O(5 - 15 cm s^{-1}) with respect to ADCP, and average drifter-HF radar track separation rate of O(5 ± 3 km day^{-1}).
	• The subtidal fluctuations accounted for 45% - 75% of the variance.
	• Wind-driven dynamics accounted for 67% of the subtidal variability.
Kelly et al. [2002]	• A short term comparison study of CODAR data with ADCP data.
	• Comparison study yielded a scalar correlation R of O(0.8 - 0.9) for along-shelf components and 0.6 and less for cross-shelf components.
	• Complex vector correlation magnitude of O(0.76 - 0.9) and phase of O(1.3^0 - 5.2^0) representing a clockwise veering of current vectors along the depth.
Kohut et al. [2006]	• Studied the influence of the environmental variability on the observed differences between CODAR data and ADCP data.
	• Comparison statistics were calculated based on various combinations such as, between different vertical bins on the same ADCP, between different ADCP, and between ADCP and different HF radars.

	• Computed *rms* differences were characterized as vertical and horizontal shears.
	• Comparison study concluded that the environment significantly influences in the observed differences between CODAR data and ADCP data and both vertical and horizontal shears contribute to the observed differences.
Prandle [1987]	• Near-shore tidal and residual circulation study using OSCR systems. • Detailed tidal analysis of OSCR data were performed. • Statistical comparisons concluded that the standard error for the OSCR system was less than 4 cm s^{-1}.
Shay et al. [2002]	• Comparison study of OSCR observations with moored and ship-mounted ADCP data. • Comparison study revealed a bias of $O(4 - 8$ cm s$^{-1})$ between the surface and the subsurface measurement. • Complex vector correlation magnitude of 0.8 and phase of $O(10^0 \sim 20^0)$ representing a clockwise veering of current vectors along the depth.
Essen H. H., [1993]	• Surface current observational study using CODAR and its dependence on wind. • A good correlation was found between surface current and wind. • Linear wind forcing explained 35% - 60% of the surface current variance. • Surface current to wind velocity ratio was of $O(0.015 - 0.025)$ and a clockwise veering of the current vector with respect to the wind was observed. • Detailed analysis of Ekman and Stokes Drift using the measured surface currents and wind stress.
Essen et al. [2003]	• Comparison study of WERA measurements with ADCP data. • A good agreement between WERA and ADCP currents was observed. • Comparison between WERA currents and wind velocities revealed that ~ 30% of the current variance was due to local wind forcing.

Kohut et al. [2001], *Kohut, J. T. and S. M. Glenn* [2003]	• A series of direct measurements of CODAR receiver antenna beam patterns for the NJSOS. • Distortion of the antenna pattern was observed when the antenna was deployed in the field, and the distortion was mainly due to the local environment. • Direct measurements of antenna beam patterns and comparisons with ADCP currents revealed that the compact CODAR antenna provided accurate direction estimates for radial current vectors even in the cluttered environments.
Kohut et al. [2004]	• Ocean current variability of the inner NJ Shelf was studied using CODAR data along with *in-situ* and meteorological observations. • The hydrographic variability of the inner NJ shelf was largely bimodal between summer stratification and winter mixing. • Correlations between wind and surface currents were observed to be high during stratified season and low during mixed season.
Harlan J. A., [2005]	• The CODAR observations for short time scales and the effects of long ocean waves and winds on HF radar observations were studied. • A new method of Empirical Mode Decomposition (EMD) was employed to analyze HF radar observations for high frequencies, which also incorporated the wave breaking and Stokes Drift. • The results concluded that wave field interactions account for a significant portion of the short time scale fluctuations which were previously attributed as inherent noise of the radar measurement.
Laws K., [2001]	• An evaluation study of direction finding MUSIC algorithm and beam forming approach for Multi-frequency Coastal Radar (MCR) systems. • This study used simulations and comparison with *in-situ* measurements, and concluded that direction finding MUSIC algorithm was more efficient than beam forming technique for MCR systems, especially for the lower frequencies.

4.3 Statistical Measures

Statistical measures for both scalar and vector correlations are used in the present study to validate the HF radar data. The scalar correlation measures include co-efficient of determination (r^2), root mean squared error *(rmse)*, mean square error *(mse)*, mean, and standard deviation. The scalar correlation measures between any two data sets $x = x_1,$ $x_2, x_3 \ldots \ldots x_n$ and $y = y_1, y_2, y_3 \ldots \ldots \ldots y_n$ are given below

The mean is defined as
$$\left(\overline{x}\right) = \frac{1}{n}\sum_{i=1}^{n} x_i \qquad (4.1)$$

The standard deviation is defined as
$$(s_x) = \sqrt{\frac{1}{n-1}\sum_{i=1}^{n}(x_i - \overline{x})^2} \qquad (4.2)$$

The correlation co-efficient is defined as
$$(r) = \frac{1}{n-1}\sum_{i=1}^{n}\left[\left(\frac{x_i - \overline{x}}{s_x}\right)\left(\frac{y_i - \overline{y}}{s_y}\right)\right] \qquad (4.3)$$

The co-efficient of determination is defined as (r^2), which explains the percentage of the total variance.

The root mean squared error is defined as
$$(rmse) = \sqrt{\frac{1}{n}\sum_{i=1}^{n}(x_i - y_i)^2} \qquad (4.4)$$

The mean square error is defined as
$$(mse) = \frac{1}{n}\sum_{i=1}^{n}(x_i - y_i)^2 \qquad (4.5)$$

The vector correlation between any two vector fields is computed following the formulations of complex correlation suggested by *Kundu* [1976]. The complex correlation coefficient between two vector series $w_1(t) = u_1(t) + iv_1(t)$ and $w_2(t) = u_2(t) + iv_2(t)$ is defined as

$$\rho = \frac{\langle u_1 u_2 + v_1 v_2 \rangle}{\langle u_1^2 + v_1^2 \rangle^{\frac{1}{2}} \langle u_2^2 + v_2^2 \rangle^{\frac{1}{2}}} + i \frac{\langle u_1 v_2 - u_2 v_1 \rangle}{\langle u_1^2 + v_1^2 \rangle^{\frac{1}{2}} \langle u_2^2 + v_2^2 \rangle^{\frac{1}{2}}} , \theta = \tan^{-1} \frac{\langle u_1 v_2 - u_2 v_1 \rangle}{\langle u_1 u_2 - v_1 v_2 \rangle} \tag{4.6}$$

where ρ represents the magnitude of the complex correlation ($<$ 1.0 by *Schwartz inequality*) which is independent of any co-ordinate system and gives the overall measure of correlation, and θ represents the phase of the complex correlation, representing the average veering of second vector with respect to the first. The phase correlation is meaningful only if the magnitude of the correlation is high. The values of $\rho \sim 1.0$ and $\theta \sim 0.0$ denotes an excellent comparison between the two vector series.

4.4   Comparison of HF Radar Data and Mooring Data

In order to assess whether the HF radar data is capable of representing the true surface current circulation, near-surface current data remotely measured using HF radar were statistically compared with the *in-situ* current measurements obtained from the moored current profilers.

4.4.1 Mooring Data

Rutgers University deployed three moorings: Mooring: 1 (M1), Mooring: 2 (M2), and Mooring: 3 (M3) for the period of February 22nd – April 27th, 2007, located in the vicinity of the Sandy Hook and the Breezy Point HF radar stations. The main focus of

these current profiler deployments is to study the performance of HF radar (CODAR) system in a near-shore environment dominated by shallow water waves and wave-current interaction. This mooring experiment was conducted as part of ongoing research to improve the HF radar (CODAR) processing algorithms. The M1 is deployed at a mean water depth of 7.5 m and at a radial distance of ~ 1.5 km from the Sandy Hook HF radar station, while M2 is deployed at a mean water depth of 12.3 m and at a radial distance of ~ 3.25 km from the Breezy Point HF radar station. The M3 is deployed at a mean water depth of 16.7 m and at a radial distance of ~ 9.5 km from the Breezy Point HF radar station. The M3 mooring failed to provide a reliable data set above 10 m from the head of the instrument and was not used in this validation study. The locations of M1, M2, and M3 are shown in the Figure: 3.4 (see Chapter 3) and the details of the moorings were tabulated and shown in Table: 4.2. The mooring data consists of u (east–west) and v (north–south) velocity components, which are averaged over the depth of each measurement bin along the water column (see Table: 4.2).

4.5   Results and Discussion

4.5.1 Time-series Comparison

Surface current data obtained using HF radar are compared with the near-surface bin data of M1 and M2 for the period of February 24th – April 24th, 2007. The various correlation measures of this comparison study are tabulated and shown in Table: 4.3. The

Table: 4.2.   Specifications of moorings.

Mooring No:	M1	M2	M3
Deployment Site	*Near-shore of Sandy Hook*	*Near-shore of Breezy Point*	*Offshore of Breezy Point*
Mooring Type	*Acoustic Wave and Current profiler : AWAC (NORTEK)*	*Acoustic Doppler Current Profiler : RDI (TELEDYNE)*	*Acoustic Doppler Profiler : ADP (SONTEK)*
Agency	*Rutgers University*	*Rutgers University*	*Rutgers University*
Latitude	*40.435 N*	*40.533 N*	*40.538 N*
Longitude	*73.967 W*	*73.875 W*	*73.777 W*
Transmitting Frequency	*1 MHz*	*1200 kHz*	*1500 kHz*
Number of Depth Cells	*16*	*24*	*32*
Cell Size	*0.5 m*	*0.5 m*	*0.5 m*
Blanking Distance	*0.4 m*	*0.59 m*	*0.5 m*
Mean Depth	*7.5 m*	*12.3 m*	*16.7 m*
Temperature	*Yes*	*Yes*	*Yes*
Salinity	*No*	*No*	*Yes*
Comments	*Topmost bin data @ 0.6m from MSL*	*Topmost bin data @ 1.2m from MSL*	*Topmost bin data @ 6.0m from MSL*

Table: 4.3.   Correlation between HF radar data and near-surface bin data of moorings.

Mooring No:	Depth Location	HF radar					
		r^2 (*u*)	r^2 (*v*)	rmse(*u*) (m s^{-1})	rmse(*v*) (m s^{-1})	rho (ρ)	theta: θ (degrees)
Mooring: 1	*@ 1.6m from MSL*	*0.33*	*0.42*	*0.15*	*0.26*	*0.63*	*-22.7*
Mooring: 2	*@ 1.7m from MSL*	*0.79*	*0.06*	*0.14*	*0.14*	*0.82*	*-18.9*
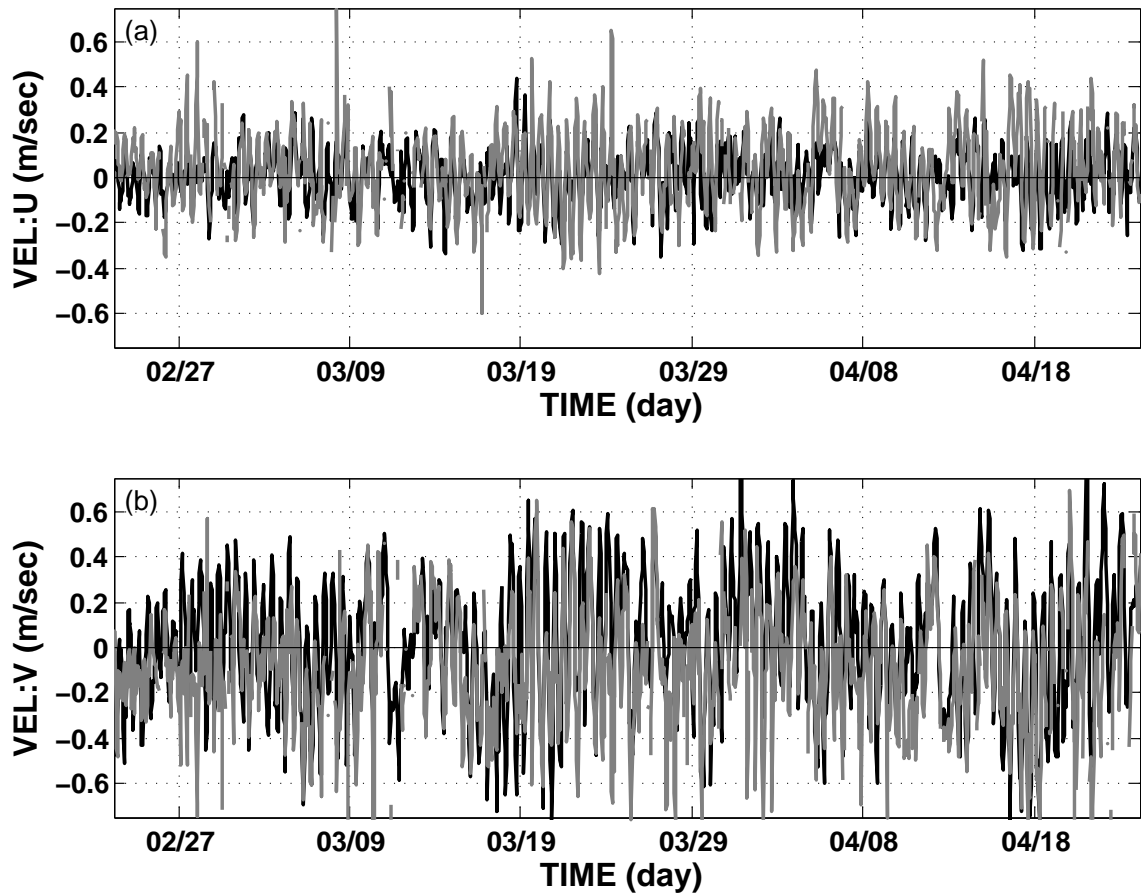
Figure: 4.1. Time-series comparison for the *u* (a) and *v* (b) components of Mooring: 1 data at the depth of 1.6 m from the surface and HF radar data at M1 location. (Black lines indicate Mooring: 1 data and gray lines indicate HF radar data).

time-series plots for the u and v components of the HF radar and M1 data at the depth of 1.6 m from the surface are shown in Figure: 4.1. The M1 data at the depth of 1.6 m from the surface were regressed to the HF radar data for both u and v components and the scatter plot is shown in Figure: 4.2. The time-series plot shows that the surface current obtained using HF radar marginally compares with the M1 data for both u and v components, with an r^2 value of 0.33 for u component and 0.42 for v component, and *rmse* of 0.15 m s^{-1} for u component and 0.26 m s^{-1} for v component. A complex correlation magnitude ρ of 0.63 and a clockwise veering θ of 23^0 were found between M1 currents and HF radar currents. The scatter plot along with the line of regression shows a slope of 0.86 and bias of 0.03 m s^{-1} for the u component, and a slope of 0.59 and a bias of -0.11 m s^{-1} for the v component.

The time-series plots for the u component and v component of the HF radar data and M2 data at the depth of 1.7 m from the surface are shown in Figure: 4.3. At this location, the predominant current is the u component and the time-series plot shows a better correlation for the u component than the v component, with an r^2 value of 0.79 for u component and 0.06 for v component, and *rmse* of 0.14 m s^{-1} for u component and 0.14 m s^{-1} for v component. The complex correlation between the two vector series shows a magnitude ρ of 0.82 and a clockwise veering θ of 19^0. The M2 data at the depth of 1.7 m from the surface were regressed to the HF radar data for both u and v components and the scatter plot is shown in Figure: 4.4. The scatter plot along with the line of regression shows a slope of 1.08 and bias of 0.06 m s^{-1} for the u component, and a slope of 0.34 and a zero bias for the v component.
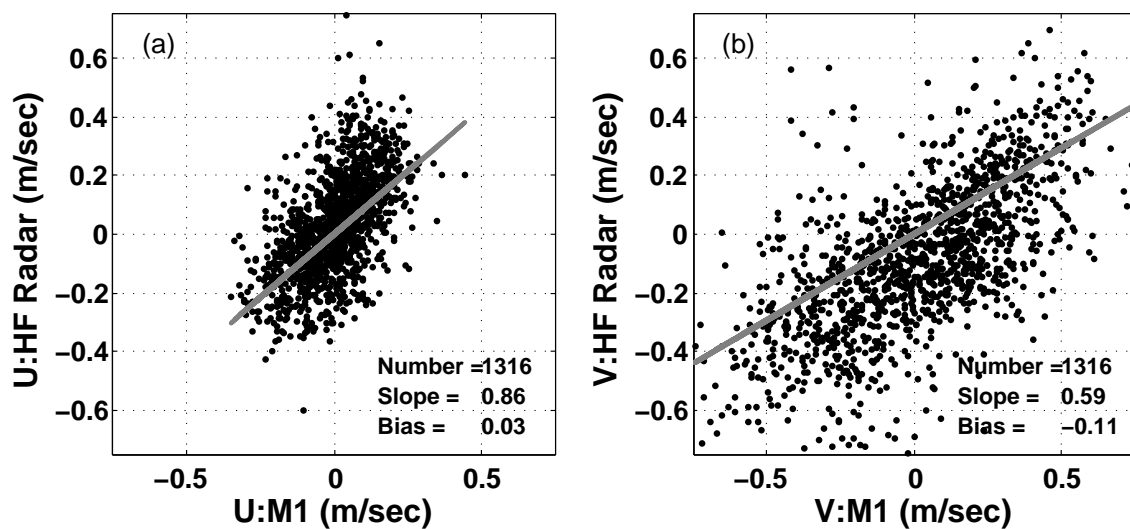
Figure: 4.2. **Scatter plots for the *u* (a) and *v* (b) components of Mooring: 1 data at the depth of 1.6 m from the surface and HF radar data at M1 location. (Gray line indicates regression fit).**
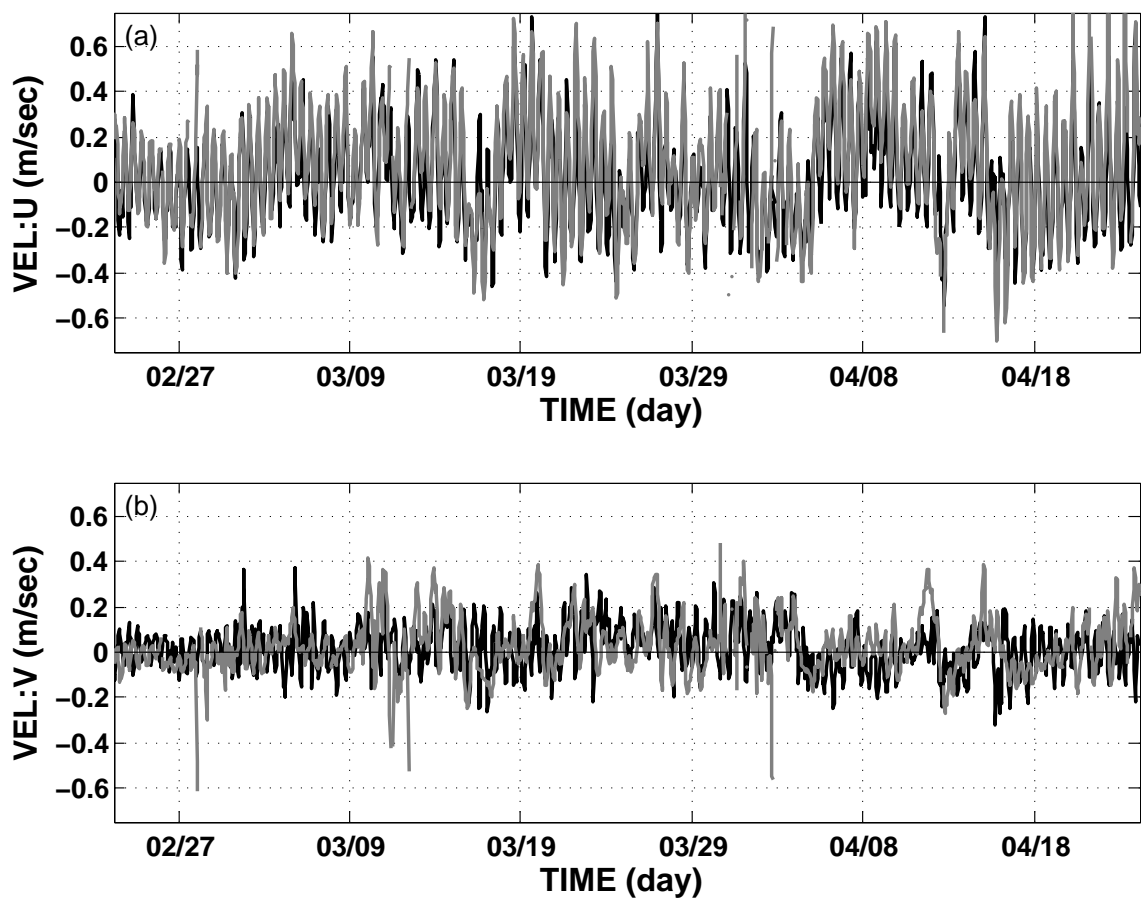
Figure: 4.3. Time-series comparison for the *u* (a) and *v* (b) components of Mooring: 2 data at the depth of 1.7 m from the surface and HF radar data at M2 location. (Black lines indicate Mooring: 2 data and gray lines indicate HF radar data).
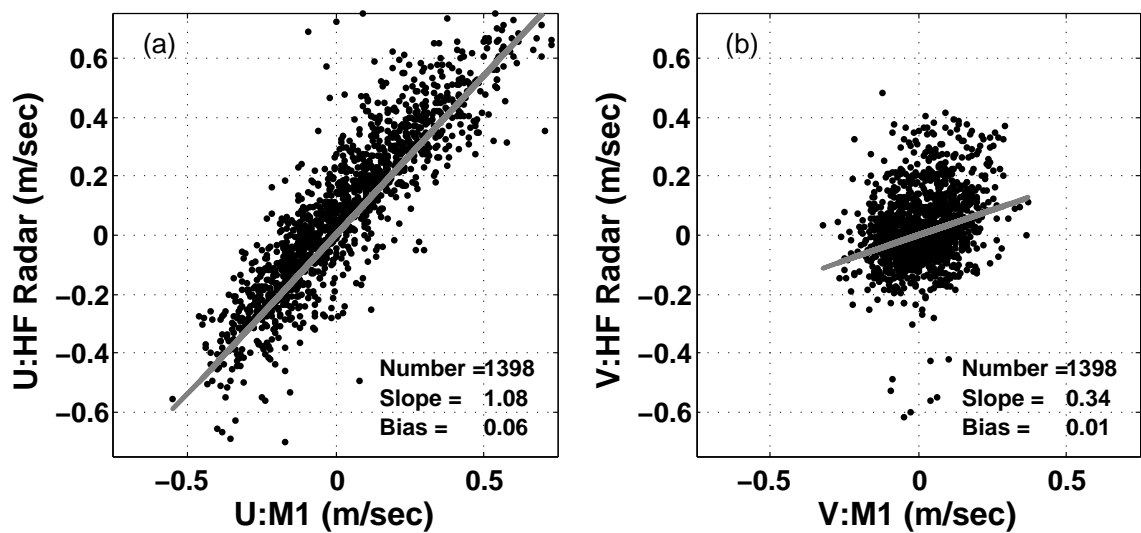
Figure: 4.4. Scatter plots for the *u* (a) and *v* (b) components of Mooring: 2 data at the depth of 1.7 m from the surface and HF radar data at M2 location. (Gray line indicates regression fit).

The mean (Equation 4.1) and standard deviation (Equation 4.2) were computed for the HF radar surface currents and M1 and M2 near-surface bin currents with respect to u component and v component respectively and shown in Table: 4.4. The mean error is defined as the difference between the mean value of the HF radar data and the M1 and M2 near-surface bin data, and standard deviation error is defined as the difference between the standard deviation of the HF radar data and the M1 and M2 near-surface bin data. A mean error of 0.11 m s^{-1} is observed for v component between HF radar data and M1 near-surface bin data, and a mean error of 0.06 m s^{-1} is observed for u component between HF radar data and M2 near-surface bin data. This mean error values results in higher *rmse* values for v component at the M1 location and for u component at the M2 location (see Table: 4.3).

The time-series for the u component and v component of the HF radar surface currents and M1 and M2 near-surface bin currents were least-square fitted using tidal constituents [K_1, O_1, Q_1, K_2, M_2, S_2, N_2, M_4, M_6] for the period of February 24th - April 24th, 2007. The reconstructed time-series using least-squares tidal fitting of HF radar surface currents and M1 and M2 near-surface bin currents were statistically compared with respect to u component and v component respectively. The comparison between tidally-fitted HF radar data and M1 near-surface bin data shows a good correlation for u component (r^2 value of 0.78 and *rmse* of 0.06 m s^{-1}) as well as for v component (r^2 value of 0.88 and *rmse* of 0.10 m s^{-1}). A good complex correlation (magnitude ρ of 0.96 and a clockwise veering θ of 26^0) is achieved between the two tidally-fitted vector series of HF

Table: 4.4. **Mean and standard deviation of HF radar data and near-surface mooring data.**

Description	Mean (m s⁻¹)		St: Dev (m s⁻¹)		Mean Error (m s⁻¹)		St: Dev Error (m s⁻¹)	
	u	*v*	*u*	*v*	*u*	*v*	*u*	*v*
Mooring: 1 *(@ 1.6m from MSL)*	*0.01*	*0.01*	*0.12*	*0.29*	*0.03*	*-0.11*	*0.06*	*-0.02*
HF radar *(@ M1 Location)*	*0.04*	*-0.10*	*0.18*	*0.27*				
Mooring: 2 *(@1.7m from MSL)*	*0.02*	*0.02*	*0.23*	*0.10*	*0.06*	*0.01*	*0.04*	*0.03*
HF radar *(@ M2 Location)*	*0.08*	*0.02*	*0.27*	*0.13*				

radar data and M1 near-surface bin data. The comparison between tidally-fitted HF radar data and M2 near-surface bin data shows a better correlation for u component (r^2 value of 0.93 and *rmse* of 0.06 m s^{-1}) than for v component (r^2 value of 0.39 and *rmse* of 0.08 m s^{-1}). The complex correlation between the two tidally-fitted vector series of HF radar data and M2 near-surface bin data shows a magnitude ρ of 0.93 and a clockwise veering θ of 23^0. The various correlation measures for the comparison between tidally-fitted HF radar data and M1 and M2 near-surface bin data are tabulated and shown in Table: 4.5.

4.5.2 Tidal Analysis

Tidal analysis has been performed for the HF radar surface currents and the near-surface bin currents of M1 and M2 for the period of February 24th – April 24th, 2007. The tidal analysis was performed using MATLAB T_Tide toolbox [*Pawlowicz et al.,* 2002], in which seven major tidal constituents [K_1, O_1, Q_1, K_2, M_2, S_2, N_2], and two overtides ('shallow water' tide [M_4, M_6]) were considered. Tidal ellipses for the predominant M_2 tidal constituent for the HF radar data and the M1 and M2 near-surface bin data were plotted and are shown in Figure: 4.5. The tidal ellipses of the HF radar data and the M1 near-surface bin data shows a good comparison with respect to the sense of rotation, and phase [see Figure: 4.5a], while M1 data shows a higher magnitude than HF radar data, and a difference in orientation of $\sim 26^0$ is observed between the two ellipses. The tidal ellipse of the HF radar data and the M2 near-surface bin data shows a moderate comparison [Figure: 4.5b]. Even though both the ellipse shows a comparable magnitude,

Table: 4.5. **Correlation between HF radar data and near-surface bin data of moorings (Tidal fit).**

Mooring No:	Depth Location	HF radar					
		r^2 (*u*)	r^2 (*v*)	rmse(*u*) (m s^{-1})	rmse(*v*) (m s^{-1})	rho (ρ)	theta: θ (degrees)
Mooring: 1	*@ 1.6m from MSL*	*0.78*	*0.88*	*0.06*	*0.10*	*0.96*	*-26.2*
Mooring: 2	*@ 1.7m from MSL*	*0.93*	*0.39*	*0.06*	*0.08*	*0.93*	*-23.2*
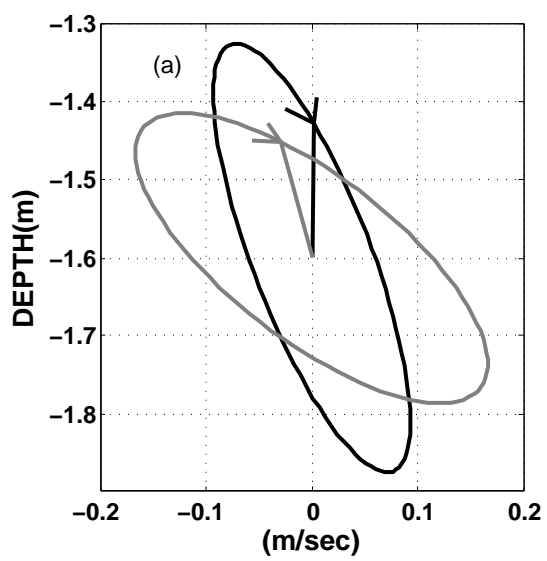
HF radar data and M1 at the depth of 1.6 m
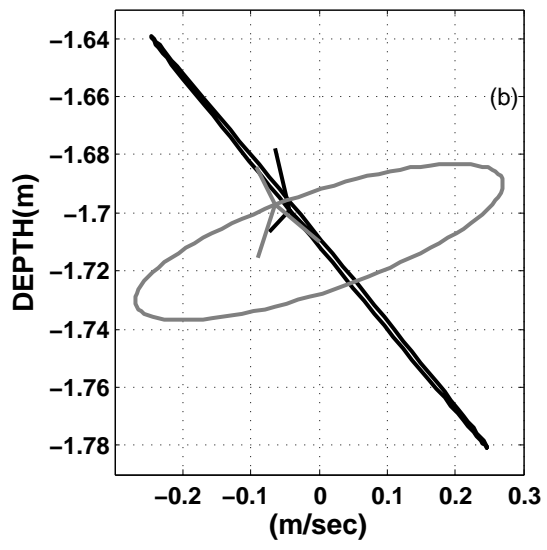
HF radar data and M2 at the depth of 1.7 m

Figure: 4.5. **The *M₂* tidal ellipses for HF radar data (gray line) and mooring data (black line).**

Table: 4.6   Tidal analysis results for HF radar data and near-surface bin data of moorings.

Description	M_2 Tide (Frequency = 0.0805114 cph)			
	semi-major axis (m s^{-1})	semi-minor axis (m s^{-1})	orientation (degrees)	phase (degrees)
Mooring: 1 *(@ 1.6m from MSL)*	0.29	-0.06	105	306
HF radar *(@ M1 Location)*	0.23	-0.09	131	305
Mooring: 2 *(@1.7m from MSL)*	0.26	0.00	164	280
HF radar *(@ M2 Location)*	0.27	-0.02	4	103

they exhibit a difference in sense of rotation, in phase of $\sim 177^0$, and in orientation of $\sim$ 160^0. The tidal analysis results are tabulated and shown in Table: 4.6.

4.5.3 Rotary Spectral Analysis

Rotary spectral analysis has been carried out for the HF radar surface current data, and the near-surface bin data of M1 and M2 following the method suggested by *Gonella* [1972]. The spectral estimates were computed for three-day segments and the results were then averaged over the entire study period of 60 days. The spectral density plots for the clockwise and the counter-clockwise components of the HF radar data and the M1 near-surface bin data is shown in Figure: 4.6. The spectral energy level of HF radar data and M1 data are comparable at the semi-diurnal peaks for the clockwise component, while for the counter-clockwise component, HF radar data shows less energy at semi-diurnal and inertial frequencies than M1 data. The HF radar fails to capture the high frequency, low energy fluctuations represented by M1 data. The spectral density plots for the clockwise and the counter-clockwise components of the HF Radar data and the M2 near-surface bin data is shown in Figure: 4.7. The spectral characteristics of HF radar data and M2 data are comparable. HF radar data shows higher energy inertial peaks than M2 data for the clockwise component.
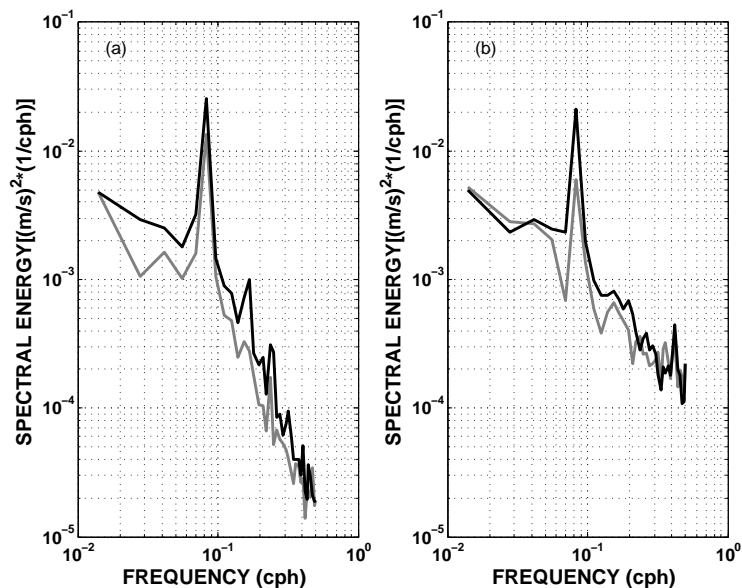
Figure: 4.6.   Rotary spectra for M1 data (a) and HF radar data (b)

(Gray line: counter-clockwise component, black line: clockwise component).
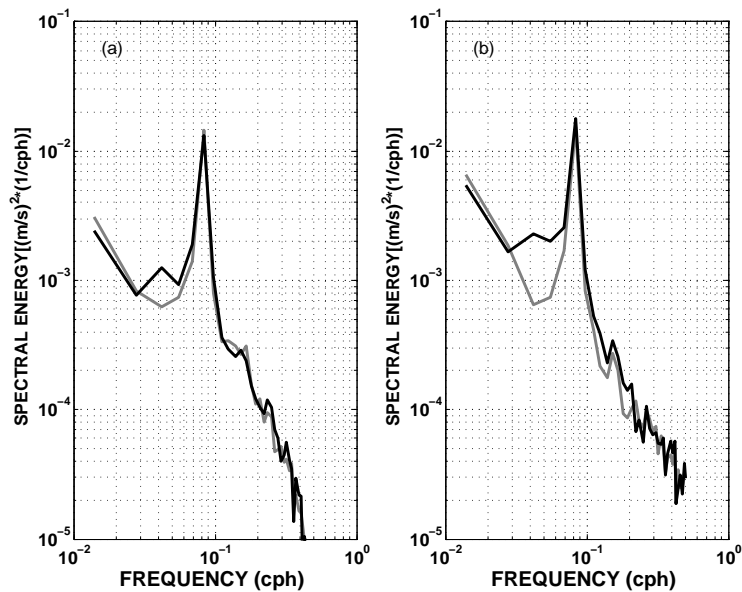
Figure: 4.7.   Rotary spectra for M2 data (a) and HF radar data (b)

(Gray line: counter-clockwise component, black line: clockwise component).

4.6   Conclusions

HF radar measured surface currents were statistically compared with near-surface current measurements obtained from the two moorings. The comparison of HF radar surface currents and M1 near-surface bin currents reveals a moderate correlation. At M1, the along-shore component *v* shows a better correlation than the cross-shore component *u* (see Table: 4.3), and this suggest the influence of cross-shore processes in the near-surface layers. The comparison of HF radar data and M2 near-surface bin data reveals a good correlation for the along-shore component *u* and a poor correlation for the cross-shore component *v* (see Table: 4.3). Even though the along-shore current *u* is predominant at M2, the cross-shore processes in the near-surface layers affect the comparison results resulting in very low *v* correlation.

Most of the earlier HF radar validation studies dealt with comparison of HF radar radial vectors with *in-situ* current measurements. Some of the earlier HF radar validation studies compared HF radar total vectors, obtained by combining radial vectors form two different sites, with near-surface current measurements obtained from mooring located at the center of the HF radar footprint with maximum temporal data coverage and data quality (see Table: 4.1).

The present validation study uses HF radar total vectors obtained by combining radial vectors from four different standard-range CODAR sites of the HF radar network. HF radar total vectors can be considered as spatially averaged over an ocean surface patch of $O(1 \sim 4 \text{ km}^2)$ and near-surface depth averaged of $O(0.5 \text{ m})$. The mooring data

represents a point measurement of subsurface currents and is averaged over the depth of measurement bin of $O(0.5$ m$)$. This difference in the spatial averaging of the current measurement highly influences the validation results. The estimation of the total vector field from the radial vectors introduces inherent errors due to the geometric combination of the radials (see Chapter 3, Section 3.5) which can possibly affect the validation results. The poor correlation between HF radar data and M1 data can also be due to high GDOP error (see Chapter 3, Section 3.5) of about 0.8 (see Figure: 3.8). While a lower GDOP error of about 0.4 (see Figure: 3.8) at M2 improves the correlation between the HF radar data and M2 data.

The comparison between tidally-fitted HF radar data and M1 near-surface bin data shows a good correlation for both u and v component with higher r^2 values and lower *rmse* (see Table: 4.5). The M_2 tidal ellipse for the HF radar data and M1 near-surface bin data (see Figure: 4.5a) show a good comparison as indicated by the correlations for the tidally-fitted data. The rotary spectral density plots for HF radar data and M1 near-surface bin data shows similar characteristics with respect to semi-diurnal peaks for the clockwise component (see Figure: 4.6). The comparison between tidally-fitted HF radar data and M2 near-surface bin data shows a good correlation with higher r^2 values and lower *rmse* for the u component and a poor correlation for the v component (see Table: 4.5). This poor correlation with respect to v component is also observed in the M_2 tidal ellipse plots (see Figure: 4.5b). The rotary spectral density plots for HF radar data shows higher energy inertial peaks than M2 data for the clockwise component (see Figure: 4.7).

The improved correlation for the tidal fit comparison between HF radar and M1 and M2 near-surface bin data suggests that horizontal and vertical shear in the near-surface water column are responsible for the observed *rmse* differences between the two current vectors. The influence of the environmental variability on the observed *rms* differences between HF radar radial currents and ADCP near-surface currents at the inner NJ shelf have been reported by *Kohut et al.* [2006].

The proximity of M1 and M2 location to the HF radar station (M1 falls within the first HOSR range cell, M2 falls within second BRZY range cell) and the shallow water conditions influences the HF radar data quality at M1 and M2 location. The HF radar data in the first range cell were generally neglected owing to poor data quality. These factors contribute to the observed differences between HF radar data and mooring data.

Since HF radar works on the basic assumptions of linear wave theory and deep water conditions, the influence of shallow water waves and wave-current interaction are not well resolved by the generic HF radar processing algorithm. A site specific HF radar algorithm should be employed which uses the actual depth corrected wave celerity rather than the depth invariant deep water wave celerity for the computation of surface current from the frequency Doppler shift equation [*Barrick,* 2005]. The mooring experiment (February – April, 2007) was conducted as part of ongoing research between Rutgers University and CODAR, Inc. to improve the HF radar (CODAR) processing algorithms incorporating near-shore environment. The developments in the HF radar (CODAR) processing algorithm based on shallow water conditions may improve the validation results.

Chapter 5

The New York Harbor Observing and Prediction System (NYHOPS)

5.1   Introduction

The NYHOPS [http://stevens.edu/maritimeforecast] is an estuarine and coastal ocean forecast system based on an extensive real-time observational network of distributed sensors, which is designed, supported, and maintained by Stevens Institute of Technology [*Bruno et al.,* 2001; *Bruno et al.,* 2006] since the beginning of 2004. The system is designed to simulate the water parameters, weather, and environmental conditions of the NY/NJ Harbor Estuary, Raritan Bay, Long Island Sound, NY Bight, and the NJ coastal ocean in real-time, and forecast the conditions in near and long-term.

The NYHOPS forecast model is a three–dimensional, time-dependent hydrodynamic model, based on the estuarine coastal and ocean model (ECOM), a shallow water version of the Princeton ocean model (POM) [*Blumberg and Mellor,* 1987]. This numerical model is based on an Arakawa-C grid, and solves a coupled system of differential, prognostic equations describing the conservation of mass,

momentum, heat, and salt. The model is based on orthogonal curvilinear co-ordinate system in the horizontal plane and sigma co-ordinate system in the vertical plane. The vertical eddy viscosity coefficients were calculated using Mellor–Yamada level 2.5 turbulence closure scheme [*Mellor and Yamada,* 1982] with subsequent modifications by *Galperin et al*. [1988], and *Blumberg et al.* [1992]. The model uses the shear dependent Smagorinsky formulation [*Smagorinsky,* 1963] for the calculation of horizontal eddy viscosity. The model recognizes fast, barotropic external waves and slow, baroclinic internal waves, and solves corresponding barotropic and baroclinic equations with different time steps using a mode splitting technique.

5.2   The NYHOPS Model Domain

The high-resolution model domain consists of 147 x 452 (I x J) curvilinear segments in the horizontal plane, and 11 sigma levels in the vertical plane. The model domain encompasses the entire NY/NJ Harbor Estuary, Long Island Sound, and the NJ and Long Island coastal ocean. The model domain includes the tidal Hudson River up to the federal dam at Troy, NY; at its northern boundary. The open ocean boundary of the model domain is bound: *(a)* southeast, at the continental shelf to depths smaller than the 200 m isobath, *(b)* southwest, by a line extending from coastal Maryland south of Delaware Bay, and *(c)* east, to a line extending from Nantucket Island, MA. The model grid resolution varies throughout the domain ranging from approximately 7.5 km at the open ocean boundary to less than 50 m in several parts of the NY/NJ Harbor Estuary. The

depth of the water column varies from approximately 200 m at the open ocean boundary to less than 1 m near the shore and in several parts of the NY/NJ Harbor Estuary. The external barotropic mode assumes a constant temperature and salinity and uses a computational time step of 1 second, while the internal baroclinic mode uses a computational time step of 10 seconds. The model uses a spatially varying bottom friction coefficient for the bottom boundary layer.

The NYHOPS model was calibrated by comparing water levels at 14 locations, current velocities at six locations, salinity and temperature at 35 locations over a period of one year (October 1988 - September 1989) and successfully validated for a period of one year (October 1994 - September 1995) against elevation data at 13 locations, current data at five locations and salinity and temperature data at 27 locations [*Blumberg et al.,* 1999]. A recent NYHOPS model validation for the year of 2004 was reported by *Fan et al.* [2006]. The model domain and the orthogonal curvilinear grid system are shown in Figure: 5. 1.

5.3   The NYHOPS Model Forcing

The model forcing functions consist of *(a)* ocean boundary conditions of sea surface elevation, temperature and salinity fields along the open boundary, *(b)* surface meteorology, and *(c)* freshwater inflows from rivers, streams, wastewater treatment plants, and point sources from combined sewer overflows and surface runoffs.
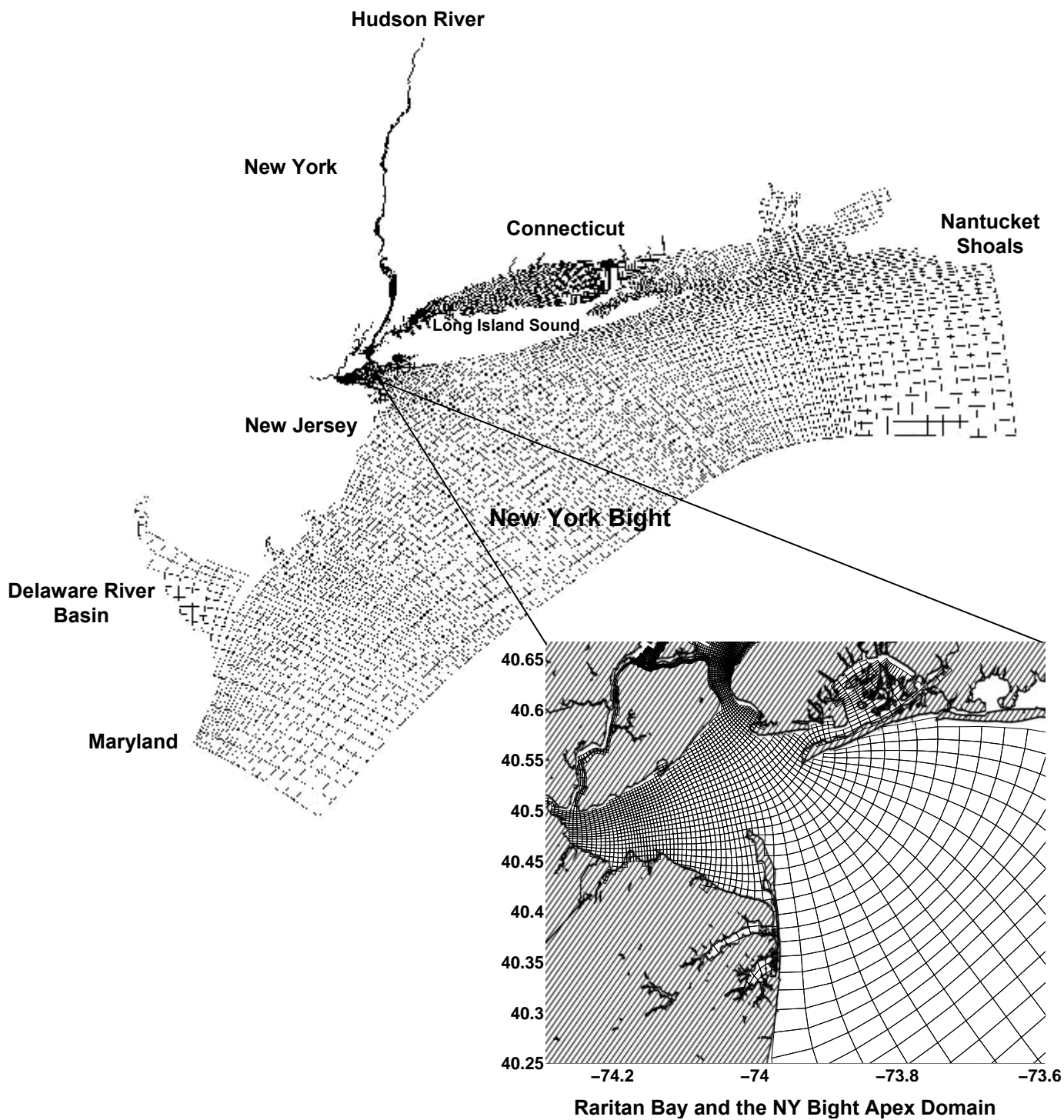
Figure: 5.1.   The New York Harbor Observing and Prediction System (NYHOPS)

high-resolution model grid [Acknowledgement*: Mr. Nickitas Georgas*].

5.3.1 Ocean Boundary Conditions

The open ocean boundary conditions are specified along the entire southern boundary of the model, from the coast of Maryland to the coast of Massachusetts, using the information extracted from regional ocean models. The sea surface elevation boundary condition includes the cross-shelf climatological slope, astronomical tides, and the sub-tidal component. Tidal sea level forcing along the open boundary is created by superposition of seven major tidal constituents [K_1, O_1, Q_1, K_2, M_2, S_2, N_2], two overtides ('shallow water' tide [M_4, M_6]) constituents, and a steady constituent (Z_0). The harmonic constants for each of these tidal constituents are extracted from the East Coast 2001 database, created using US Army Corp of Engineers application of the ADCIRC tidal model [*Mukai et al.,* 2002]. Sub-tidal (meteorological storm surge and barometric effects) sea level is provided by an extratropical storm surge forecasting model created by NOAA's Meteorological Development Lab [http://www.nws.noaa.gov/mdl/etsurge/]. Based on earlier modeling experience in the NY/NJ Harbor Estuary and the system wide eutrophication model (SWEM) [*HydroQual, Inc.,* 2001], a constant sea level tilt of 11 cm (western boundary) and 13 cm (eastern boundary) is also added at the cross-shelf open boundaries to resolve the long term alongshore ocean currents. Temperature and salinity (baroclinic) climatological open boundary conditions are based on long-term monthly averages of 97 years of record (1900-1997) [*NODC (Levitus) World Ocean Atlas,* 1998] provided by the NOAA-CIRES, climate diagnostics center, Boulder, Colorado, USA, at their website at [http://www.cdc.noaa.gov/cdc/data. nodc.woa98.html].

5.3.2 Surface Meteorological Boundary Conditions

The relative humidity, cloud cover, wind speed and direction, and barometric pressure are provided by the operational NOAA-NCEP North American Meso (NAM) model forecast which uses a weather research and forecasting non-hydrostatic mesoscale model (WRF-NMM) on a 12 km Lambert conformal grid [218-NAM-12 version, ftp://ftpprd.ncep.noaa.gov/pub/data/nccf/com/nam/prod/]. The temporal resolution of NAM is three hours. The NAM meteorological forecasts are then optimally interpolated to the NYHOPS model grid. Incoming solar radiation is computed based on latitude and day of the year. Heat fluxes across the ocean surface are based on solar radiation, relative humidity, cloud cover, and winds input to the sub-model of *Ahsan and Blumberg* [1999]. The response of surface currents to surface wind stress and barometric pressure gradients is also incorporated.

5.3.3 Fresh Water from Rivers, Steams, and Non-Riverine Sources

The freshwater forcing from rivers and streams are based on inflows from 92 rivers and tributaries including 74 gauged USGS stations, NOAA/NOS water level stations, non-riverine freshwater discharges from 280 wastewater treatment plants obtained from the interstate sanitation commission, and storm water runoffs.

The NYHOPS forecast system is designed, based on the operational protocol developed by *Kelley et al.* [1997] for the NOAA/NWS regional ocean forecast system

(ROFS). The NYHOPS system provides accurate and comprehensive realizations of meteorological and oceanographic conditions in the past (hindcasts), present (nowcasts) and future (forecasts). The schematic diagram of NYHOPS prediction cycle is shown in Figure: 5.2.

The NYHOPS prediction system for each day is scheduled to run for 72 hours, in which 0 to 24 hours represent the past (hindcast mode), 25 to 48 hours represents the first day forecast, and 49 to 72 hours represent the second day forecast. The hindcast mode uses observed forcing functions and a startup file is written out at the end of 24 hours, which is used for the smooth and seamless restart of the next prediction cycle. The forecast simulations are performed using forecasted forcing functions, except for the freshwater forcing which are based on daily persistence. The model simulations of water parameters such as water level elevation, current, salinity, temperature, were hourly averaged and archived at every 30 minutes for each prediction cycle.
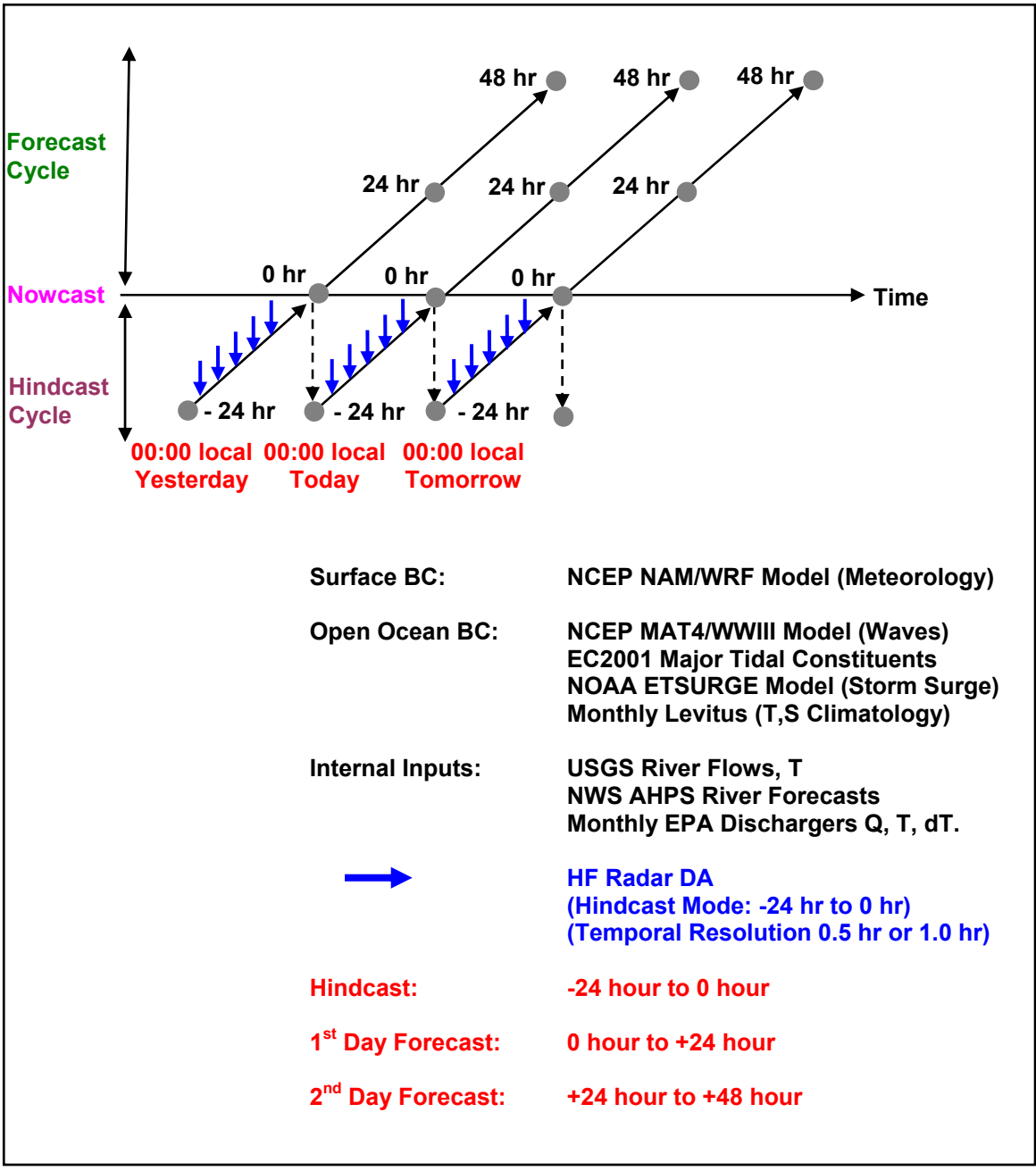
Figure: 5.2. The New York Harbor Observing and Prediction System (NYHOPS) model hindcast / nowcast / forecast cycle (HF radar data assimilation is also indicated).

Chapter 6

Data Assimilation

6.1   Introduction

Data assimilation (DA) is a sophisticated combination of observational data and a numerical model. An optimal description of the dynamic state of the ocean can be achieved by combining ocean observational data with a numerical model. Initially DA was more widely applied in the meteorology and climate models than in oceanography due to the paucity of large scale ocean observational data sets. Research and development in the fields of instrumentation and technology over the last three decades have substantially improved coastal ocean observation systems. These have provided an enormous amount of real-time ocean measurements, which has addressed the insufficiency of the observational data. The increasingly available ocean observational data are appropriate for the DA to obtain the best possible representation of the ocean truth, which is better, than could be obtained using just the numerical model or the observational data alone [*Anderson et al.,* 1996].

The atmospheric and ocean forecast models are based on the non-linear, partial differential primitive equations solved using the given initial conditions and the model

boundary conditions. The observational data, which are considered as the "ground truth", are introduced into the numerical model by DA techniques in order to enhance the performance and the forecasting capability of the model. The real time observations can be used as the initial conditions in an efficient numerical model to improve the model skill. Since the ocean surface is not completely measured, there is a need to combine the measured data and the ocean model in order to extract the maximum available information and its spatial and temporal variability. The DA must extract and filter the useful information from noisy and potentially inaccurate data and then to combine it with the model. The goal is for the model to forecast more efficiently and accurately. The DA can be used to compensate the model errors as well as the errors associated with the forcing functions. The DA methods such as Optimal Interpolation (OI), Successive Correction, and Nudging are fairly simple with a low computational burden. The Kalman Filter (KF), Ensemble Kalman Filter (EnKF), Extended Kalman Filter (EKF), Variational methods in 3 or 4 Dimensions (3DVAR, 4DVAR), Adjoint Model, and Multivariate Optimal Interpolation (MVOI) are more advanced and complex DA methods requiring longer computational time.

6.2   Brief Description of Data Assimilation Methods

The DA methods can be generally classified as passive assimilation and active assimilation.

6.2.1 Passive Assimilation

In this approach, the modeled fields are synthesized with the measurements without a feedback to the model state. Synthesis is performed by using only the model output and the observed data, giving a finishing touch. The passive assimilation is not model intrusive, and does not deal with the primitive equations and the boundary conditions of the model. Laplace smoothing and Kriging are good examples of the passive assimilation.

6.2.2 Active Assimilation

In this approach, the modeled fields are synthesized with a feedback to the model state. This method uses the causal relationships between the model and the data, and updates the model state at each time. The active assimilation works with the model primitive equations and the boundary conditions. The DA methods such as KF, OI, 3DVAR, 4DVAR are good examples of the active assimilation. The DA methods can be further classified as either sequential or model trajectory methods.

6.2.3 Sequential Methods

Sequential assimilation only considers the observations made in the past until the time of analysis, which is the case of real-time assimilation systems. The assimilation can

be carried out continuously or intermittently depending upon the availability of the observational data (continuous at all times or intermittent at specific time intervals). In the sequential method, the model and the data are combined at a given time (analysis) whenever new observations are available. In the analysis step, forecast and new observations are combined to obtain a better state estimation. Once the analysis step is carried out, a forward integration is made to the next assimilation time using the analysis as the initial conditions for the model. There are different sequential methods depending upon the level of the complexity of algorithms which are described in the following sections.

6.2.3.1   Direct Insertion Approach

The simplest sequential assimilation method in which the model variables are directly substituted by their corresponding observed values, whenever available. This method assumes that the observational data are good. This method is inefficient when the data and the model are not compatible. It can even contaminate the model forecast by direct insertion of bad data. This method provides no error control on the observational data.

6.2.3.2   Nudging Approach

The sequential assimilation steps can be summarized as

$$x_a = x_f + K(y_o - Fx_f) \tag{6.1}$$

where, x is the model state variable (temperature/salinity/velocity)

                       subscript 'a' represent analysis and 'f' represent previous forecast

        y_o is the observational vector

        K is the gain matrix or weight matrix or Kalman gain, converting

                       observed – model differences to model variable space

                       incorporating the errors

        F is the forward model, converts the model variable to observation

                       variable (interpolation operator) where the error analysis is most

                       easily performed

        $(y_o - Fx_f)$ is the innovation vector

All sequential assimilation methods follow the above equations assuming a linear relationship between the model variable and the observed data. The main difference between different methods depends on the estimation of the $[K]$ matrix or the Kalman gain matrix.

In the Nudging method, the analysis is effectively performed on every time step and the term $K(y_o - Fx_f)$ appears as a forcing to the model equations which nudges the model toward the observations, and the gain matrix $[K]$ is empirically predetermined constant.

6.2.3.3 *Successive Correction Approach*

Successive Correction (SC) is a less intrusive on the model dynamics. The analysis is performed intermittently and a weighting function $[K]$ that decays monotonically with the distance in space and/or time between the model variable and the observation position is used. Several observations influence the analyzed value depending on the spatial and the temporal decay scales of the weighting function.

6.2.3.4 *Optimal Interpolation Approach or*

[Statistical Interpolation (SI) or Best Linear Unbiased Estimate (BLUE)]

In the Optimum Interpolation (OI) method, the gain matrix $[K]$ is obtained by time variant error covariances procedure. The method initially assumes that the error covariances of the model forecast and the observation fields are known. The gain matrix $[K]$ is estimated from the assumed (static) error covariance.

$$K = C_f F^T \left[FC_f F^T + C_o \right]^{-1} \tag{6.2}$$

Where, C_f is the error covariance matrix for the forecast

C_o is the error covariance matrix for the observation

F is the interpolation operator

The difficult part of the assimilation process is to obtain the error covariance matrix of the observations and the forecast model. The forecast model error covariance

matrix can be obtained by long-time (~ 10 year) prognostic integration of the model results. Even with appropriate statistical data processing, it is difficult to get information about the probabilistic distribution of the errors that affect the observational data. SC and OI method quantify the analysis error covariance and can be represented as the error bars of the forecast.

6.2.3.5   *Kalman Filter*

The Kalman Filter (KF) follows the interpolation equation (Equation 6.2) of the OI method, but includes an extra step besides the forecast and analysis steps for the calculation of the analysis error covariance matrix $[A]$, which involves an evolution equation for the forecast error covariance matrix $[C_f]$.

The information about estimation accuracy can be represented by analysis error covariance matrix $[A]$ for any $[K]$, defined as

$$A = [1 - KF] * C_f \tag{6.3}$$

The difficult part of the KF is with defining the weights for the present, past, and future information to obtain the best analysis and KF provides those weights by using the evolving forecast error covariance. This step increases the computational demand as the model domain is of the order of $10^4 \sim 10^6$ grid points, and makes KF very difficult for real-time applications. The different modifications of KF are

Extended Kalman Filter (EKF): in which $[K]$ derived from the error covarinaces are propagated in time using a linearized or simplified forecast model. The input fluctuations and the measurement errors are additive.

Ensemble Kalman Filter (EnKF): In which $[K]$ derived from a ensemble of random replicates propagated with a nonlinear model. The form of input fluctuations and measurement   errors is unrestricted.

6.2.4 Model Trajectory Methods (Variational Methods)

In this method, the observed data are fitted into the model by optimization which will give the best model trajectory that fits the data at the time of observation. The problem reduces to a search for optimal values of the control variables, which gives the best fit of model trajectory and data. For each subsequent time interval the model state at the beginning is modified to fit the new data, and the process is repeated. In the variational method, future observations can be used. Assimilation can be done continuously or intermittently depending upon the availability of the observed data.

The variational approach is a minimization problem of a function defined as "cost function" or "objective function"$[J]$, which measures the difference between the model trajectory (for a particular time) and the observed data. The observations are both temporally and spatially varying. The problem is to find the solution to the model equations which will be the best fit to the observed data, by minimizing the cost functions

with respect to model boundary conditions or well defined constraints. The governing equation will be normally quadratic, represented as

$$J = \sum \left([F(x) - y_o]^T W [F(x) - y_o] \right) \tag{6.4}$$

Where, y_o is the observed data at various location and time

      $F(x)$ is the model equivalent (*x* represent the model state variable)

      W is the relative weights of different observations

     The variational method allows a non-linear relation between the model and the data, but estimation of $[W]$ makes this method extremely difficult in real-time applications. The different extensions of the variational methods are 1DVAR, 3DDAR, 4DVAR.

6.3   Review of Studies on Oceanographic Data Assimilation

     The DA research in oceanography was initiated with the availability of global satellite altimetry data for the ocean surface topography, and has been significantly improved with the launching of the TOPEX/Poseidon satellite altimeter in 1992. Earlier oceanographic DA studies, in which sea surface height (SSH) and sea surface temperature (SST) measurements were successfully assimilated into numerical ocean models, demonstrated the need for the DA in enhancing the performance of the models [*Holand and Malanotte-Rizolli,* 1989; *Mellor and Ezer,* 1991; *Ezer and Mellor,* 1994; *Ezer and Mellor,* 1997; *Ishikawa et al.,* 1996; *Fukomori et al.,* 1995]. Research studies in

which ocean surface currents measured using surface drifters were successfully assimilated into primitive equation ocean circulation models, showed the importance of the DA in representing the features of Eulerian ocean circulation and small scale eddies, which are normally unresolved by the satellite data [*Molcard et al.,* 2003; *Ozgokmen et al.,* 2003; *Fan et al.,* 2004; *Lin et al.,* 2006].

The HF radar observation system provides a continuous stream of ocean surface current data, which makes it appropriate for the DA. Assimilation of the surface currents measured using HF radar normally follows a two step procedure. The first step deals with the development of a particular minimization scheme which includes the specification of error covariance functions. The next step involves the projection of the surface only HF radar observations to three-dimensional model variables. These two steps of the assimilation procedure are not needed to be mutually exclusive and can be combined into a single step assimilation procedure, once the three-dimensional error covariance functions were defined.

One of the earlier DA studies using HF radar data was reported by *Lewis et al.* [1998] for Monterey Bay, in which a pseudo-shearing stress, defined as the difference between the surface current of the model and data was used as a forcing function. A series of DA studies using HF radar data for the Innovative Coastal-ocean Observing Network (ICON) in Monterey Bay, [*Shulman et al.*, 2002; *Paduan and Shulman,* 2004], used a Physical-Space Statistical Analysis system (PSAS) [*Cohn et al.*, 1998] scheme based on data dependent velocity covariance functions. Corrections were incorporated to the model surface currents and these corrected currents were then projected down into the

water column based on physical arguments of energy conservation and Ekman theory. An HF radar DA study for the Oregon Coast was reported by *Oke et al.* [2002], which used a sequential OI scheme, based on PSAS and the corrections to the model state were implemented by a Time-Distributed Averaging Procedure (TDAP). Assimilation of temperature, salinity, and HF radar data into Regional Ocean Modeling System (ROMS) as a part of Long-term Ecosystem Observatory (LEO) for the New Jersey inner shelf was reported by *Wilkin et al.* [2005], in which an OI approach was used for temperature and salinity, and a statistically based extrapolation by melding/nudging approach is used for HF radar data. Assimilation of Real-time HF Radar (WERA) data into a nested ocean model at coastal waters of southern Norway was reported by *Breivik and Saetra* [2001], which used a modified OI scheme based on EnKF ideas and the spatial covariances were derived from an ocean model rather than by simplified mathematical formulations.

Earlier HF radar DA studies were more focused towards the low frequency circulation patterns, in which the higher frequency tidal signals were eliminated by low-pass filtering of the HF radar data prior to their assimilation into the numerical ocean models. In some of the studies, the tidal forcing and surface heat fluxes were not considered in the ocean models. The present work is an attempt to assimilate a continuous stream of HF radar data into a primitive equation ocean model, incorporating tidal fluctuations, along with forcing from surface elevation, temperature/salinity fields, surface meteorology, and freshwater inflows, for the urban estuaries of the New York/New Jersey (NY/NJ) Harbor Estuary and the NY Bight.

6.4   Data Assimilation Method for the Present Study

Assimilation of the HF radar (CODAR) measured surface currents into the NYHOPS model is performed using an active and passive DA approach.

6.4.1 Passive Assimilation

A passive assimilation method based on the Laplace smoothing is used to assimilate HF radar data into the NYHOPS forecast model. The observed HF radar data were considered as the "ground truth" and the NYHOPS model results are synthesized using HF radar data in real-time, depending on the location of the data with respect to model grid. A Laplace smoothing algorithm [*Blumberg and Bruno,* 2004] is used to blend the HF radar observations and the NYHOPS model results. The Laplace smoothing process is controlled by the weighting factor, threshold, and the number of iterations. A typical plot showing the surface current field obtained by passive assimilation is shown in Figure: 6.1.

6.4.2 Active Assimilation

An active assimilation method based on the nudging scheme is used to assimilate the HF radar measured surface currents into the NYHOPS forecast model. In the nudging or Newtonian damping scheme, a forcing term is added to the dynamic model, which
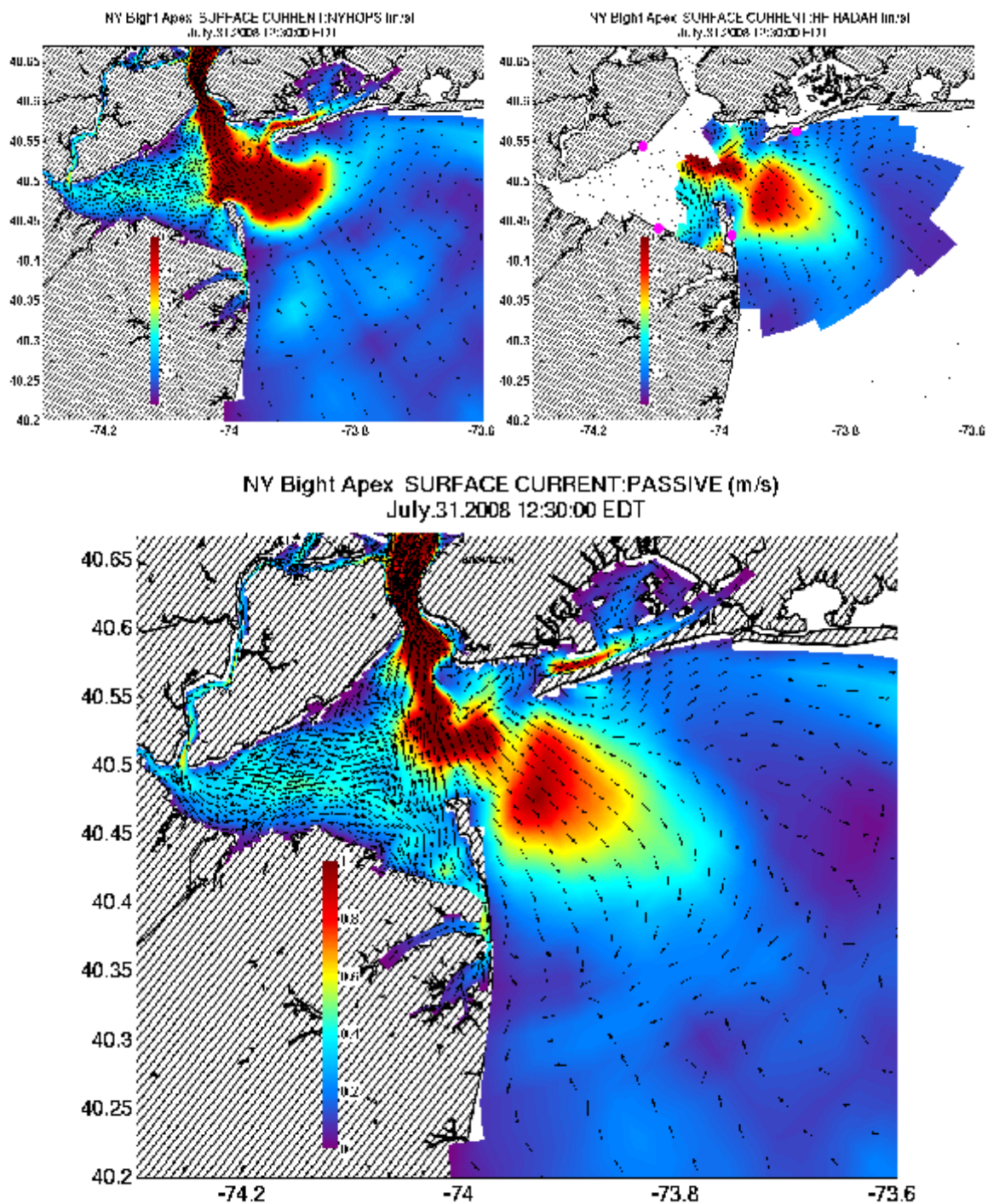
Figure: 6.1. Surface current field of NYHOPS model and by passive assimilation of HF radar data.

drives the model toward the observations. The rate of nudging must be small and should have a smooth variation with respect to spatial and temporal fields of the ocean model. Following the formulations of *Fan et al.* [2004], a nudging term is introduced in the equation of motion as

$$\frac{\partial u}{\partial t} = (physics) - \lambda(u - u^o) \tag{6.5}$$

Where u represents the model velocity, u^o represents the observed velocity, and (*physics*) includes Coriolis, pressure gradients, vertical divergence of shear stress, non-linear advection, and other terms like horizontal and vertical mixing. The empirical equation of the nudging parameter (λ) proposed by *Ishikawa et al.* [1996] can be represented as

$$\lambda_{(i,j)} = \left(1/t_a\right) * e^{\left(\frac{-r^2}{R_{NUDGE}^2}\right)} * e^{\left(\frac{-(t-t^o)}{t_d}\right)} * e^{\left(\frac{z}{z_d}\right)} \tag{6.6}$$

Where r is the distance between grid point in the model and observed data location, $t - t^o$ is the difference between assimilation and observation time, t_a is the assimilation time-scale (determines the strength of the nudge factor λ), t_d is the damping time-scale for the nudging term, R_{NUDGE} is the length-scale, $e^{(z/z_d)}$ is the exponential decay parameter which controls the depth of influence of the nudging parameter ($z = 0$ at the mean sea–surface, and z_d is the depth of influence).

The method generates sources and sinks near the observational locations. Model dynamics are get affected by these 'forces' and the data is imparted to neighboring (three-

dimensional) grid points. The present nudging assimilation method is a special case of standard OI scheme, in which the gain matrix $[K]$ is empirically predetermined, rather than derived by minimizing the square of the analysis error covariances [*Daley,* 1991].

The nudging parameter (λ) can be approximated as $\lambda_{(i,j)} = (1/t_a) * e^{\left(\frac{z}{z_d}\right)}$, where $e^{\left(\frac{-r^2}{R^2_{NUDGE}}\right)} = 1$, and $e^{\left(\frac{-(t-t^o)}{t_d}\right)} = 1$, since HF radar data is continuously assimilated and is spatially and temporally interpolated to the NYHOPS model grid location and time-step. The nudging parameter $\lambda_{(i,j)} = 0$ at all other model grid points with no HF radar measurements.

In this nudging or Newtonian relaxation scheme, the nudging parameter (λ) must be optimized in such a way that it should be large enough to make an impact while should small enough to have a smooth spatial and temporal variation with respect to three-dimensional fields of the ocean model. A series of preliminary HF radar DA experiments were conduced on the NYHOPS model for a period of 10 days to optimize the nudging parameter (λ) with respect to assimilation time-scale (t_a) and depth of influence (z_d). The comparison studies of assimilated model simulations with *in-situ* observations for these preliminary HF radar DA experiments helped to optimize the nudging parameter (λ), and an assimilation time-scale (t_a) of 1800 seconds and the depth of influence (z_d) of 2.0 m provided satisfactory results. The HF radar DA experiments discussed in the following chapters (see Chapters 7, 8, and 9) of this thesis uses an

assimilation time-scale (t_a) of 1800 seconds and the depth of influence (z_d) of 2.0 m in order to restrict the DA to near-surface layers.

Chapter 7

Surface Current Data Assimilation: An Idealized Study Using Long Straight and Curved Channels

7.1   Introduction

Prior to the assimilation of HF radar measured surface currents into the NYHOPS operational forecast model, a series of sensitivity experiments were conducted using idealized channels to study the implications of the surface current DA on the three-dimensional circulation pattern. A long straight channel configuration and a curved configuration were considered for the sensitivity experiments. The effect of the data assimilation is studied with respect to realistic estuarine forcing conditions of freshwater, tide, and density stratification. The nudging assimilation scheme explained in Chapter 6 has been used to assimilate the synthetic surface current data into the numerical ocean

model. In this idealized study, an assimilation time scale t_a of 1800 seconds is used, and the depth of influence (z_d) of 2.0 m is used in order to restrict the DA to near-surface layers

7.2   Idealized Model Configuration

7.2.1   Long Straight Channel

In order to study how well the numerical model physics responds to the DA scheme, a numerical experimental study was carried out with an idealized configuration resembling the Hudson River Estuary. A long straight channel with dimensions of 1.5 km in width, 240 km in length, and 10 m of constant depth, was discretized into 5 x 100 horizontal grid segments and 11 vertical sigma levels. This idealized estuary is shown in Figure. 7.1. Freshwater forcing of 5000 m^3 s^{-1} was introduced at the upstream end. Two different forcing conditions were considered at the downstream end for the salinity, *case (1)*: an ocean with no salinity and no tide, and *case (2)*: an ocean with a salinity of 20 psu and M_2 tide with 1.0 m amplitude. The model is simulated for 30 days, in which the following two cases were considered for the DA: an along-channel surface current of magnitude 1.0 m s^{-1} directed opposite to the river flow (+1.0 m s^{-1}), and an along-channel surface current of magnitude 1.0 m s^{-1} directed in the direction of the river flow (-1.0 m s^{-1}).

UPSTREAM

Long Straight Channel

Horizontal grid: 5 x 100 (I x J)
Vertical grid: 11 sigma levels
Length: 240 km
Width: 1.5 km
Depth: 10 m
River discharge: 5000 m^3 s^{-1}

DA Domain

Horizontal grid: 5 x 10 (I x J)

DA Domain

DOWNSTREAM
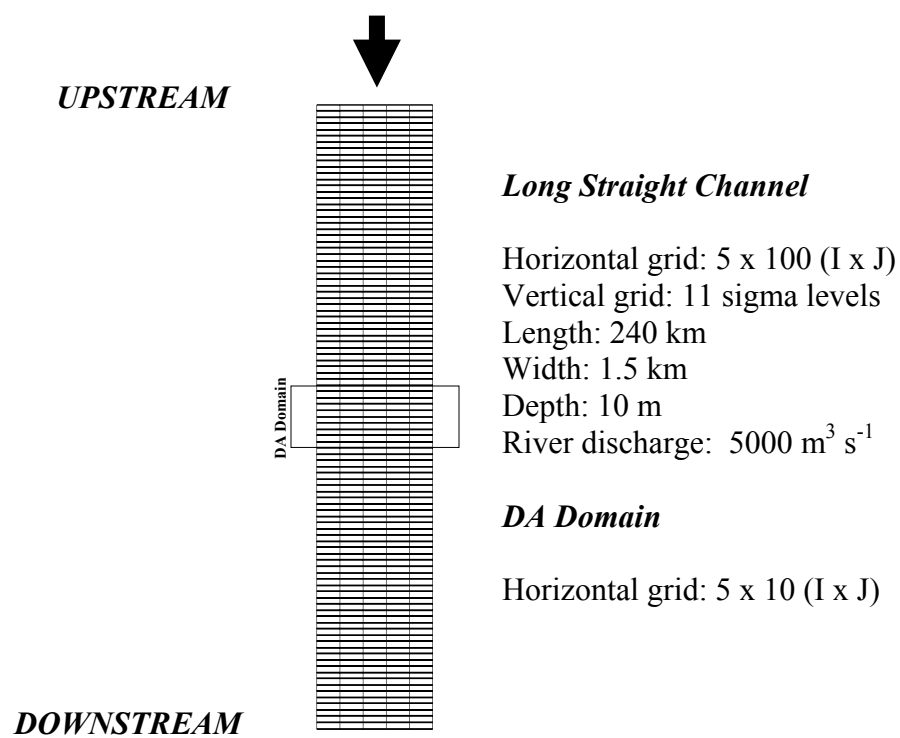
Figure: 7.1.   Idealized long straight channel estuary with flat bottom.

7.2.2 Curved Channel

In order to study the effect of DA in a more realistic estuarine configuration, an idealized estuary of curved configuration with dimensions of 5 km in width, 240 km in length, 10 m of constant depth, and R/W (R: radius of curvature, W: width) ratio of 16 was considered. The curved channel configuration was discretized into 15 x 100 horizontal curvilinear grid segments and 11 vertical sigma levels. The idealized estuary with curved configuration is shown in Figure. 7.2. The model forcing conditions for the curved estuary configuration is *case (2):* freshwater forcing of 15000 m^3 s^{-1} at the upstream end, and an ocean with a salinity of 20 psu and M_2 tide with 1.0 m amplitude at the downstream end. The model is simulated for 30 days, in which the following two cases were considered for the DA: an along-channel surface current of magnitude 1.0 m s^{-1} directed opposite to the river flow (+1.0 m s^{-1}), and an along-channel surface current of magnitude 1.0 m s^{-1} directed in the direction of the river flow (-1.0 m s^{-1}).

7.3 Results and Discussion

7.3.1 Data Assimilation in an Idealized Estuary: Long Straight Channel

Along-channel surface current of 1.0 m s^{-1} directed opposite to the river flow (+1.0 m s^{-1}) and in the direction of the river flow (-1.0 m s^{-1}), were assimilated into the

DA Domain

Curved Channel

Horizontal grid: 15 x 100 (I x J)
Vertical grid: 11 sigma levels
Length: 240 km
Width: 5 km
Depth: 10 m
River discharge: 15000 m^3 s^{-1}
Radius of curvature/Width (R/W): 16

DA Domain

Horizontal grid: 15 x 10 (I x J)

DOWNSTREAM

UPSTREAM
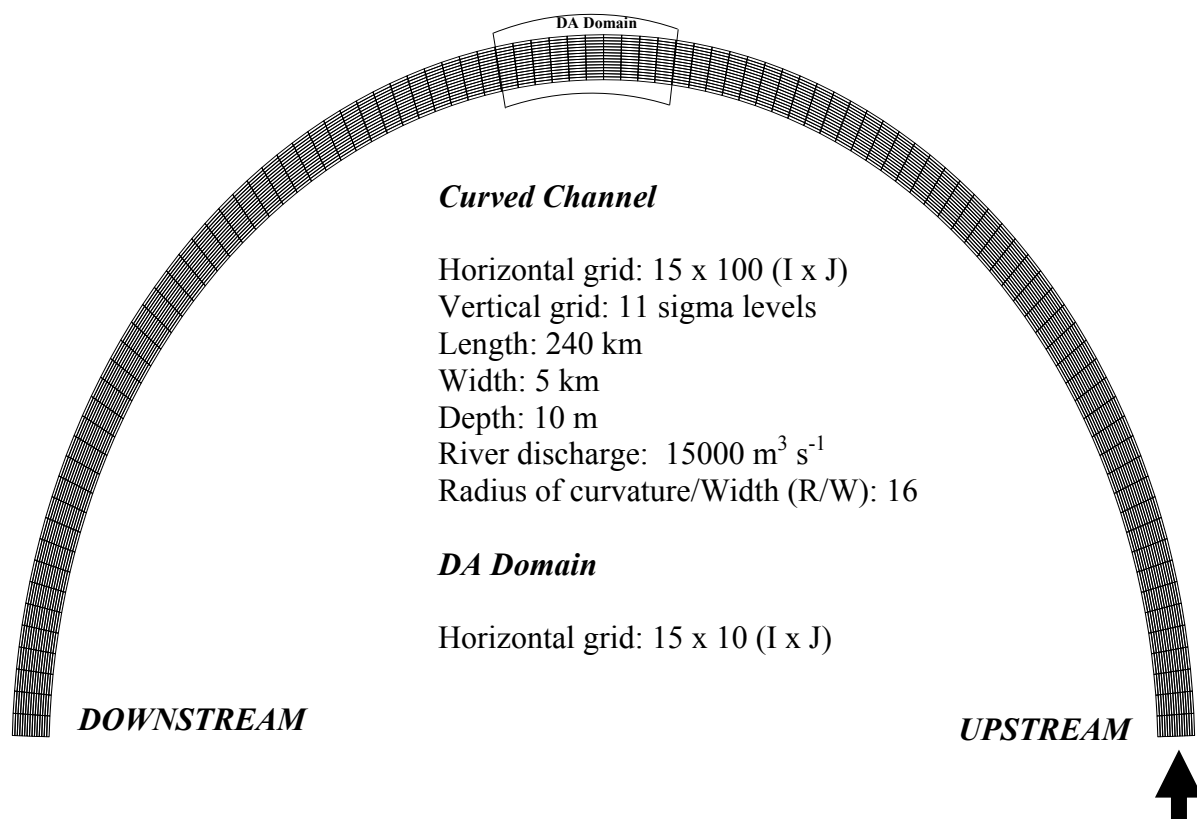
Figure: 7.2.   Idealized curved estuary with flat bottom.

model for the *case (1)* and *case (2)* forcing conditions, starting from the 5th day of model simulation and continued for another 23 hours. The current field plots for *case (1),* for the centerline section along the straight channel within the DA domain are shown in Figure: 7.3. These plots represent along-channel sectional currents with no DA, and with DA of ($+1.0$ m s^{-1}) and (-1.0 m s^{-1}) at the 10th hour from the beginning of DA. In this case, river discharge is the only predominant forcing and Figure: 7.3a with no DA shows a strong near-surface downstream flow of magnitude 0.45 m s^{-1}. The flow gradually decreases along the depth following a logarithmic profile. Figure: 7.3b represents along-channel sectional current with DA of ($+1.0$ m s^{-1}). The DA introduces a clockwise eddy circulation with a downwelling flow at the upstream end of the DA domain and an upwelling flow at the downstream end of the DA domain following a closed cell circulation, reinstating the laws of conservation. This clockwise eddy circulation is forced by the barotropic pressure gradient, and a stronger near-bottom downstream flow of 0.8 m s^{-1} is observed. In this case, the observed surface current is directed opposite to the model surface current and a strong clockwise cell circulation is introduced which affects the subsurface as well as near-bottom layers of the water column. Figure: 7.3c represents along-channel sectional currents with DA of (-1.0 m s^{-1}). In this case, the observed surface current is directed in the direction of the model surface current and no distinct anti-clockwise cell circulation was observed within the DA domain and there was no significant modification to the near-bottom flow field. The near-surface flow field shows a downstream flow of magnitude 0.8 m s^{-1}.
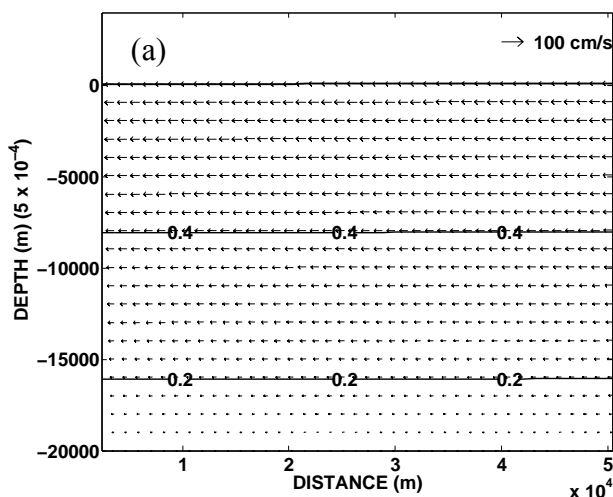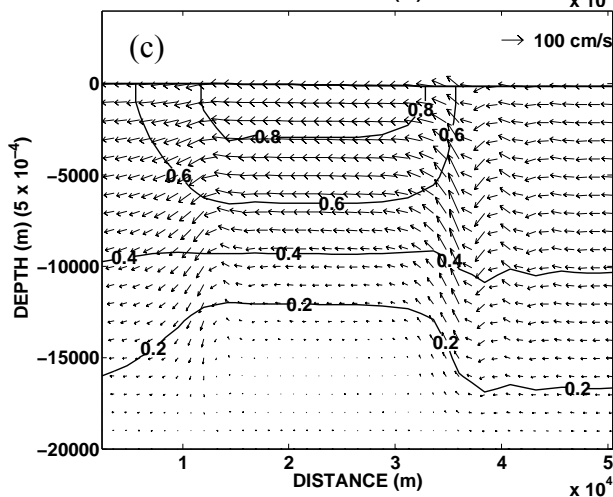
Figure: 7.3. **Long straight channel: along-channel sectional currents**
(Vertical scale exaggerated by 2000).

It should be noted that, in this case of DA of (-1.0 m s^{-1}), the barotropic pressure gradient is less prominent compared to the previous case of DA of (+1.0 m s^{-1}) and a weak three-dimensional circulation is observed.

The realistic estuarine forcing conditions of river discharge, stratification, and tides were studied in the *case (2)* simulation, and the current field plots for this case for the centerline section along the straight channel within the DA domain are shown in Figures 7.4 to 7.6. These plots represent the current field during ebb tide and flood tide within the total DA period of 23 hours. Along-channel sectional currents with no DA are shown in Figure: 7.4. During ebb tide, a weak downstream flow is observed with a magnitude of 0.3 m s^{-1} at the surface, while during flood tide, a classical two layer estuarine flow is observed with a strong near-bottom upstream flow of magnitude 0.3 m s^{-1}. Along-channel sectional currents for ebb tide and flood tide with DA of (+1.0 m s^{-1}) are shown in Figure: 7.5. The ebb tide condition represents a dominant barotropic pressure gradient and a clockwise cell circulation with a strong near-bottom downstream flow of magnitude 0.6 m s^{-1}, while during flood tide, the barotropic pressure gradient is less significant and a strong clockwise cell circulation with a near-surface upstream flow of magnitude 0.8 m s^{-1} is observed. In both ebb tide and flood tide conditions, intense vertical mixing is observed at the upstream and downstream ends of the DA domain. Along-channel sectional currents for ebb tide and flood tide with DA of (-1.0 m s^{-1}) are shown in Figure: 7.6. During ebb tide, a strong anti-clockwise cell circulation with a near-surface downstream flow of magnitude 1.0 m s^{-1} is observed, while

Figure: 7.4. **Long straight channel: along-channel sectional currents**
(Case: 2 - River Discharge + Stratification + Tides)
(Left: Ebb, Right: Flood, NO Data Assimilation)
(Vertical scale exaggerated by 2000).

Figure: 7.5. **Long straight channel: along-channel sectional currents**
(Case: 2 - River Discharge + Stratification + Tides)
(Left: Ebb, Right: Flood, Data Assimilation: +1.0 m s^{-1})
(Vertical scale exaggerated by 2000).

Figure: 7.6. **Long straight channel: along-channel sectional currents**
(Case: 2 - River Discharge + Stratification + Tides)
(Left: Ebb, Right: Flood, Data Assimilation: -1.0 m s^{-1})
(Vertical scale exaggerated by 2000).

during flood tide, a weak anti-clockwise cell circulation with a near-surface downstream flow of magnitude 0.4 m s^{-1} is observed.

The salinity profiles for the centerline section along the straight channel within the DA domain for *case (2)* forcing conditions*,* with no DA and with DA of along-channel surface currents of (+1.0 m s^{-1}) and (-1.0 m s^{-1}) are shown in Figures 7.7 to 7.9. These plots represent the salinity profile during ebb tide and flood tide within the total DA period of 23 hours. In this case, salt is being pushed out of the estuary over the simulation period of 30 days due to strong river discharge. Along-channel salinity profiles for ebb tide and flood tide conditions with no DA are shown in Figure: 7.7. The ebb tide condition shows a weak stratification with salinity difference of 1 psu between surface and bottom layers, while during flood tide, the stratification is increased and the isohalines follow a typical 'S' profile and a salinity difference of 4 psu is observed between surface and bottom layers within the DA domain. Along-channel salinity profiles for ebb tide and flood tide conditions with DA of (+1.0 m s^{-1}) are shown in Figure: 7.8. During ebb tide and flood tide, the isohalines are shifted towards upstream in the near-surface layers and downstream in the near-bottom layers, and a weakly stratified water column is observed within the DA domain. This shifting of isohalines is due to the strong clockwise cell circulation which effectively decreases the stratification within the DA domain. Along-channel salinity profiles for ebb tide and flood tide conditions with DA of (-1.0 m s^{-1}) are shown in Figure: 7.9. During ebb tide, the vertical stratification is increased due to strong anti-clockwise cell circulation, and a salinity difference of 5 psu is observed between surface and bottom layers within the DA domain.

Figure: 7.7. Long straight channel: along-channel salinity profile
(Case: 2 - River Discharge + Stratification + Tides)
(Left: Ebb, Right: Flood, NO Data Assimilation).

Figure: 7.8. Long straight channel: along-channel salinity profile
(Case: 2 - River Discharge + Stratification + Tides)
(Left: Ebb, Right: Flood, Data Assimilation: +1.0 m s^{-1}).
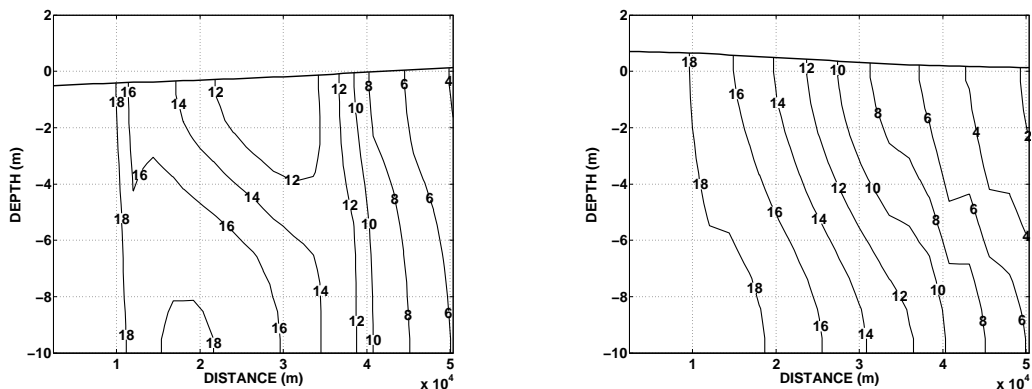
Figure: 7.9. Long straight channel: along-channel salinity profile
(Case: 2 - River Discharge + Stratification + Tides)
(Left: Ebb, Right: Flood, Data Assimilation: -1.0 m s^{-1}).

During flood tide, the salinity profile is observed to be similar to that of no DA case as a result of weak anti-clockwise cell circulation. The temperature profiles (not shown) follow similar pattern as that of the salinity profiles for all the cases of model simulation.

7.3.2 Data Assimilation in an Idealized Estuary: Curved Channel

The present study with respect to a curved estuary configuration for the *case (2)* forcing conditions is to understand the effects of DA on the circulation and density stratification in a more realistic estuarine condition. The effect of the centrifugal and coriolis forces on lateral circulation and mass transport on a curved estuary has been reported by *Georgas and Blumberg* [2003]. The present DA study incorporates the centrifugal effect due to the curvature in addition to the *case (2)* forcing conditions. Along-channel surface currents of magnitude 1.0 m s^{-1} directed opposite to the river flow (+1.0 m s^{-1}) and in the direction o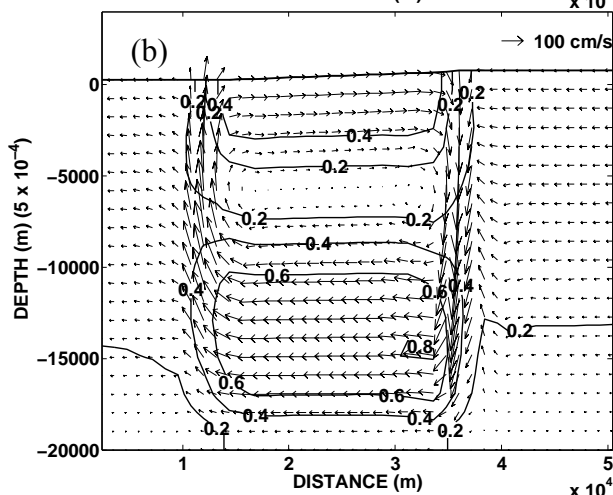f the river flow (-1.0 m s^{-1}) were assimilated into the model, starting from the 6th day of model simulation and continued to another 23 hours. The current fields with no DA, and with DA of (+1.0 m s^{-1}) and (-1.0 m s^{-1}) for the centerline section along the curvature of the estuary within the DA domain are shown in Figures 7.10 to 7.12. These plots represent the current field during ebb tide and flood tide within the total DA period of 23 hours. Along-channel sectional current fields for ebb tide and flood tide conditions with no DA are shown in Figure: 7.10 and the current fields follow similar pattern as that of the long straight channel configuration (Figure: 7.4), with a stronger flow field. Along-channel sectional current fields for ebb tide and flood tide

with DA of ($+1.0$ m s^{-1}) are shown in Figure: 7.11. The ebb tide and flood tide current fields follow similar pattern as that of the long straight channel configuration (Figure: 7.5), representing a strong clockwise cell circulation within the DA domain. Along-channel sectional current fields for ebb tide and flood tide with DA of (-1.0 m s^{-1}) are shown in Figure: 7.12, also represents a similar current field pattern as that of the long straight channel configuration (Figure: 7.6) with a stronger anti-clockwise cell circulation for ebb tide than during flood tide.

The current fields for *case (2)* forcing conditions for a section at the apex of the channel across the curved estuary are shown in Figures 7.13 to 7.15, where current field during the ebb tide and flood tide within the total DA period of 23 hours are plotted. Across-channel current field with no DA during ebb tide and flood tide conditions are shown in Figure: 7.13. During ebb tide, across-channel currents follow a weak anti-clockwise cell circulation at the channel boundaries, and a clockwise cell circulation at the center of the channel, while during flood tide, the circulation reverses its direction at the boundaries and a higher magnitude of currents were observed. Across-channel current fields with DA of ($+1.0$ m s^{-1}) are shown in Figure: 7.14. During ebb tide, a fully developed strong clockwise cell circulation with a maximum current magnitude of 0.08 m s^{-1} was observed, while during flood tide, the clockwise cell circulations were stronger at the boundaries with a magnitude of 0.04 m s^{-1} than at the center of the channel. Across-channel current fields with DA of (-1.0 m s^{-1}) are shown in Figure: 7.15. During ebb tide and flood tide, a weak circulation is observed, directed anti-clockwise during ebb tide and clockwise during flood tide.

Figure: 7.10. Curved estuary: along-channel sectional currents
(Case: 2 - River Discharge + Stratification + Tides)
(Left: Ebb, Right: Flood, NO Data Assimilation)
(Vertical scale exaggerated by 2000).

Figure: 7.11. Curved estuary: along-channel sectional currents
(Case: 2 - River Discharge + Stratification + Tides)
(Left: Ebb, Right: Flood, Data Assimilation: +1.0 m s^{-1})
(Vertical scale exaggerated by 2000).
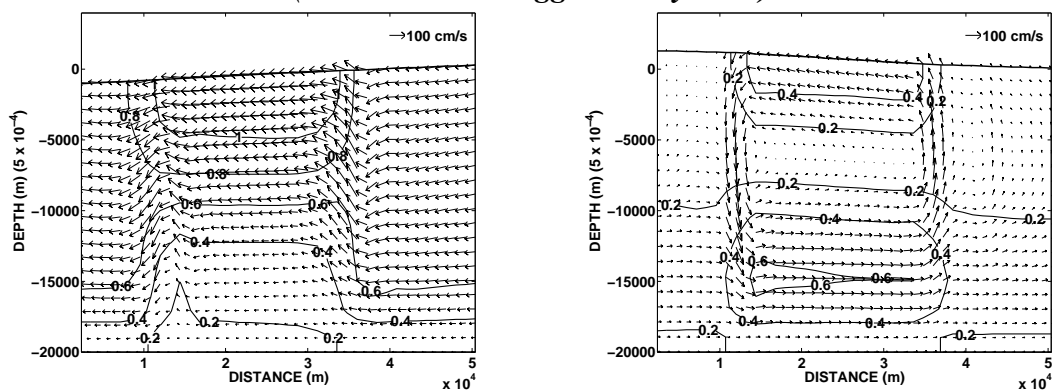
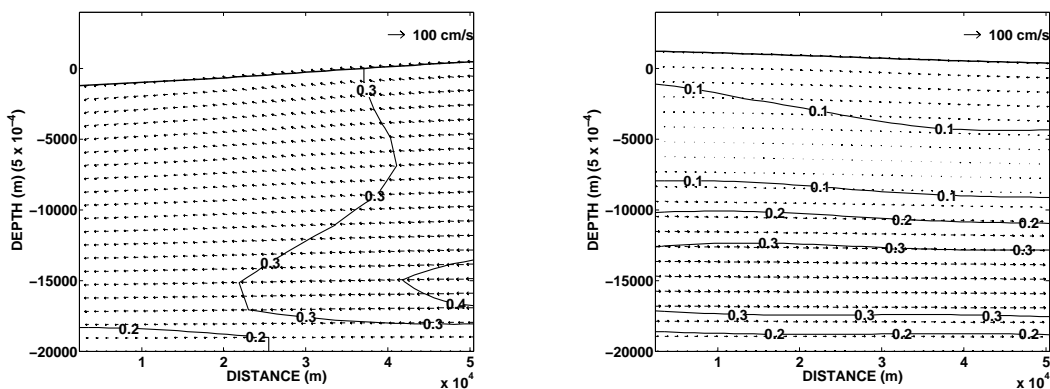**Figure: 7.12. Curved estuary: along-channel sectional currents**
(Case: 2 - River Discharge + Stratification + Tides)
(Left: Ebb, Right: Flood, Data Assimilation: -1.0 m s^{-1})
(Vertical scale exaggerated by 2000).
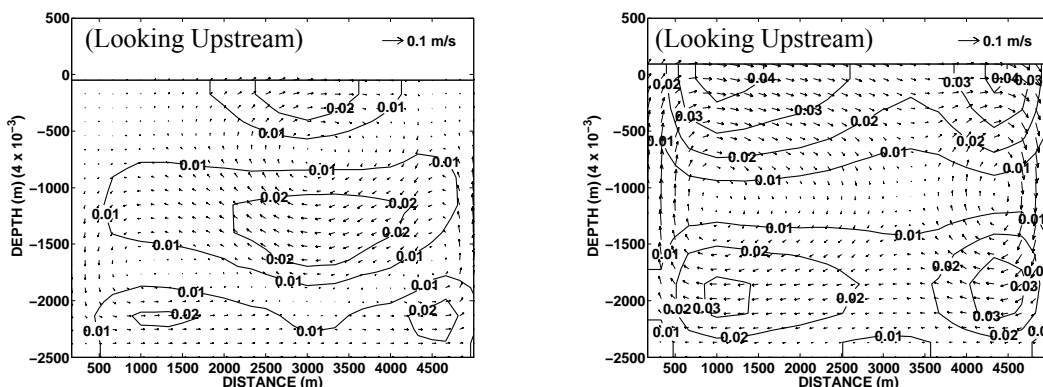
Figure: 7.13. Curved estuary: across-channel sectional currents
(Case: 2 - River Discharge + Stratification + Tides)
(Left: Ebb, Right: Flood, NO Data Assimilation)
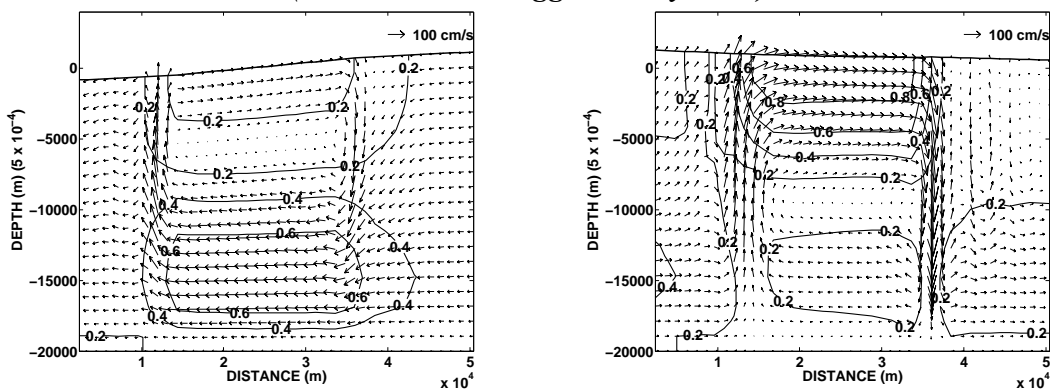*(Vertical scale exaggerated by 250).*
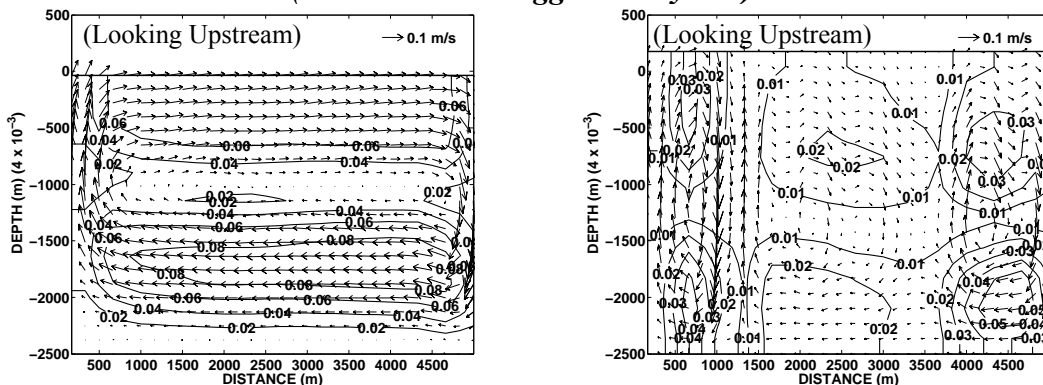
Figure: 7.14. Curved estuary: across-channel sectional currents
(Case: 2 - River Discharge + Stratification + Tides)
(Left: Ebb, Right: Flood, Data Assimilation: +1.0 m s^{-1})
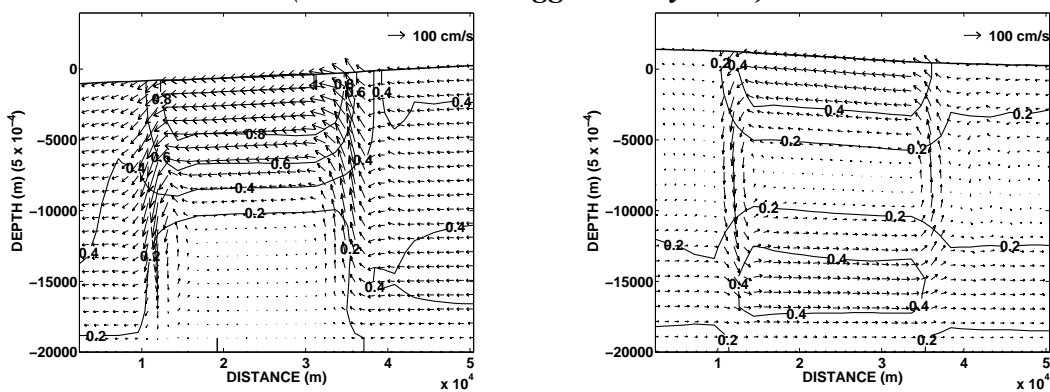*(Vertical scale exaggerated by 250).*
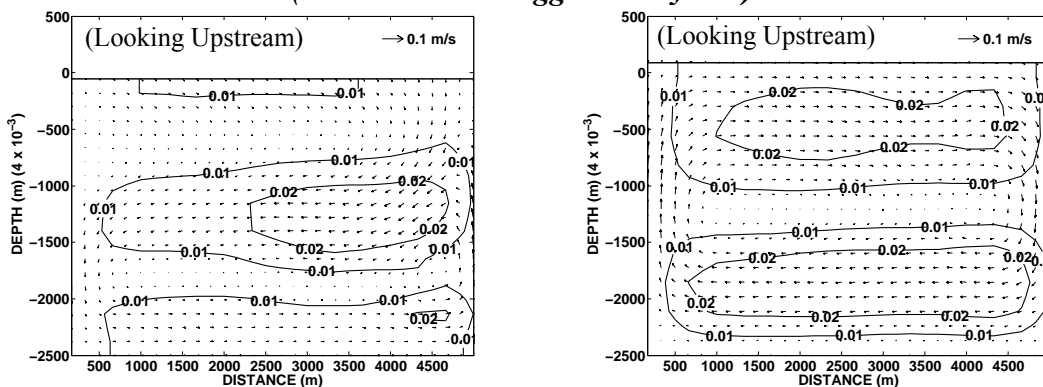
Figure: 7.15. Curved estuary: across-channel sectional currents
(Case: 2 - River Discharge + Stratification + Tides)
(Left: Ebb, Right: Flood, Data Assimilation: -1.0 m s^{-1})
(Vertical scale exaggerated by 250).

The salinity profiles for *case (2)* forcing conditions for the centerline section along the curvature of the estuary within the DA domain, with no DA, and with DA of (+1.0 m s^{-1}) and (-1.0 m s^{-1}) are shown in Figures 7.16 to 7.18. These plots represent the salinity profile during ebb tide and flood tide within the total DA period of 23 hours. Along-channel salinity profiles for the ebb tide and flood tide condition with no DA are shown in Figure: 7.16 and the profiles follow similar pattern as that of the long straight channel configuration (Figure: 7.7). Along-channel salinity profile during ebb tide and flood tide condition with DA of (+1.0 m s^{-1}) are shown in Figure: 7.17 and these profiles represent a weakly stratified condition within the DA domain due to strong vertical circulation. The vertical mixing is found to be more intense and a weaker vertical stratification is observed in the curved configuration than that of the long straight channel configuration. This increased effect on the stratification for the curved configuration can be attributed to the effect of secondary circulation across the curved estuary. Along-channel salinity profiles for ebb tide and flood tide conditions with DA of (-1.0 m s^{-1}) are shown in Figure: 7.18 and the profiles follow similar pattern as that of the long-straight channel configuration (Figure: 7.9) representing no significant effect on the vertical stratification.

The salinity profiles for *case (2)* forcing conditions for a section at the apex of the channel across the curved estuary are shown in Figures 7.19 to 7.21, where salinity profile during the ebb tide and flood tide within the total DA period of 23 hours are plotted. Across-channel salinity profile with no DA during ebb tide and flood tide
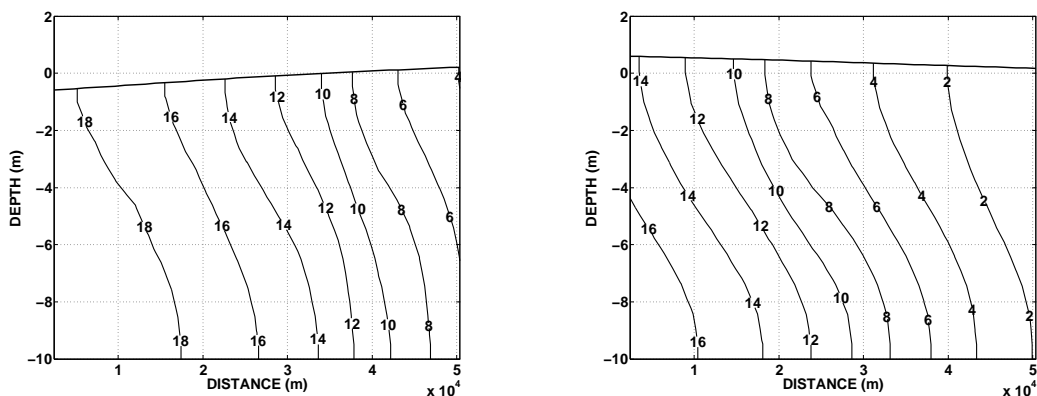
Figure: 7.16. **Curved estuary: along-channel salinity profile**
(Case: 2 - River Discharge + Stratification + Tides)
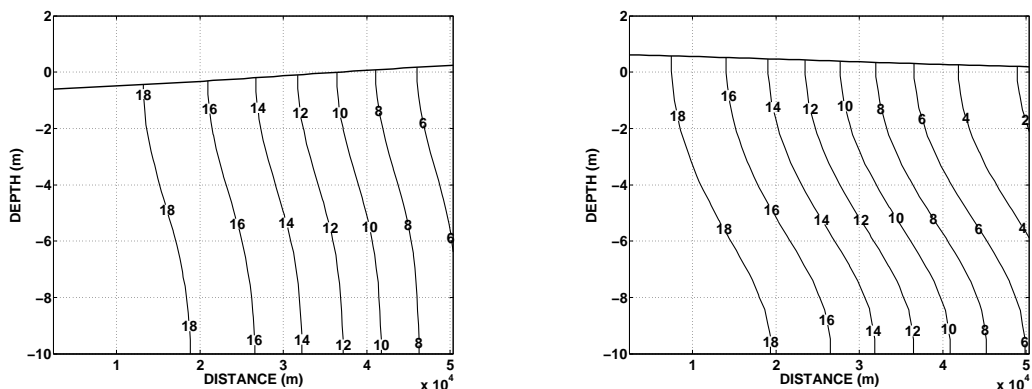*(Left: Ebb, Right: Flood, NO Data Assimilation).*
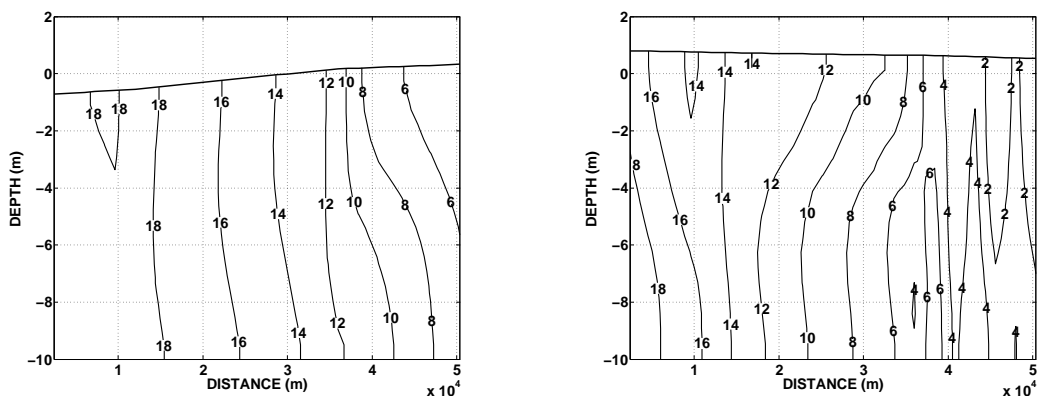
Figure: 7.17. **Curved estuary: along-channel salinity profile**
(Case: 2 - River Discharge + Stratification + Tides)
(Left: Ebb, Right: Flood, Data Assimilation: +1.0 m s^{-1}).
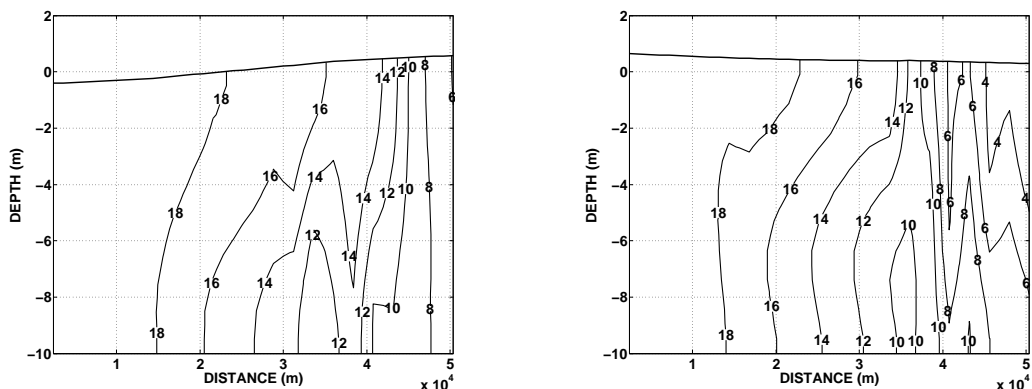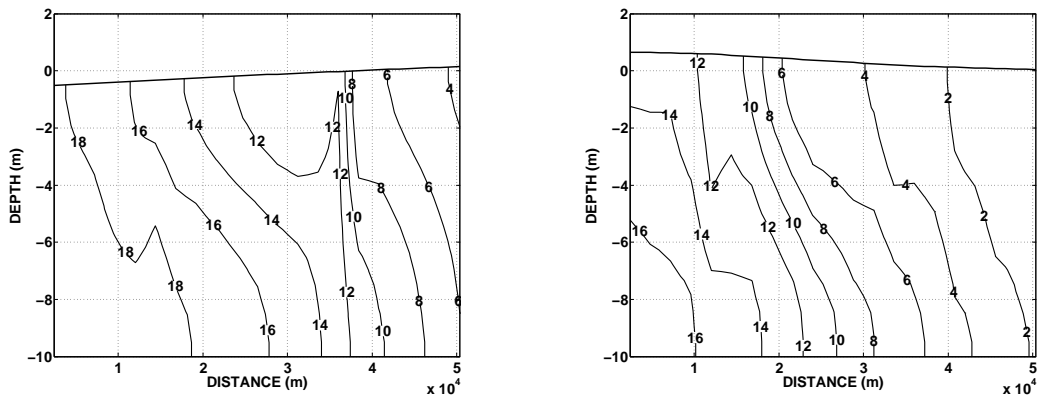

Figure: 7.18. **Curved estuary: along-channel salinity profile**
(Case: 2 - River Discharge + Stratification + Tides)
(Left: Ebb, Right: Flood, Data Assimilation: -1.0 m s^{-1}).

conditions are shown in Figure: 7.19. The ebb tide conditions shows a vertical stratification with a salinity difference of 6 psu between surface and bottom layers, while during flood tide, the stratification is decreased and a salinity difference of 4 psu is observed between top and bottom layers. Across-channel salinity profiles with DA of (+1.0 m s^{-1}) for ebb tide and flood tide conditions are shown in Figure: 7.20. Both ebb tide and flood tide represents a weak vertical stratification. Across-channel salinity profiles with DA of (-1.0 m s^{-1}) for ebb tide and flood tide conditions are shown in Figure: 7.21. During ebb tide and flood tide conditions, the salinity profile follows a similar pattern as that of no DA case. The along-channel and across-channel temperature profiles (not shown) follow similar pattern as that of the salinity profiles for all the cases of model simulation.

7.4   Conclusions

Surface currents were assimilated into an estuarine and coastal ocean circulation model using nudging scheme for an idealized model of long straight and curved channels. The model is forced with realistic estuarine conditions of river discharge, tide, and density stratification. In the case of long straight channel configuration with only river discharge forcing condition, DA of along-channel synthetic surface currents directed opposite to the river flow (+1.0 m s^{-1}) introduces a strong fully developed clockwise cell circulation within the DA domain. The DA of along-channel synthetic surface currents directed in the direction of the river flow (-1.0 m s^{-1}) with only river
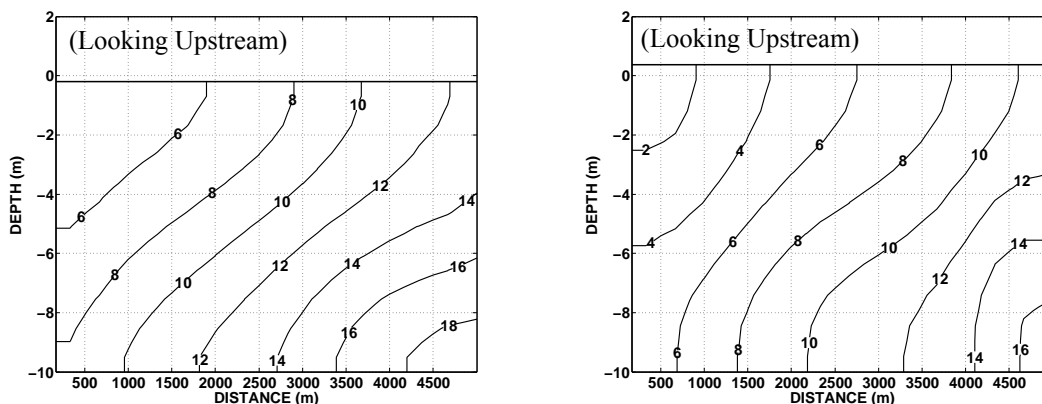
Figure: 7.19. Curved estuary: across-channel salinity profile
(Case: 2 - River Discharge + Stratification + Tides)
(Left: Ebb, Right: Flood, NO Data Assimilation).
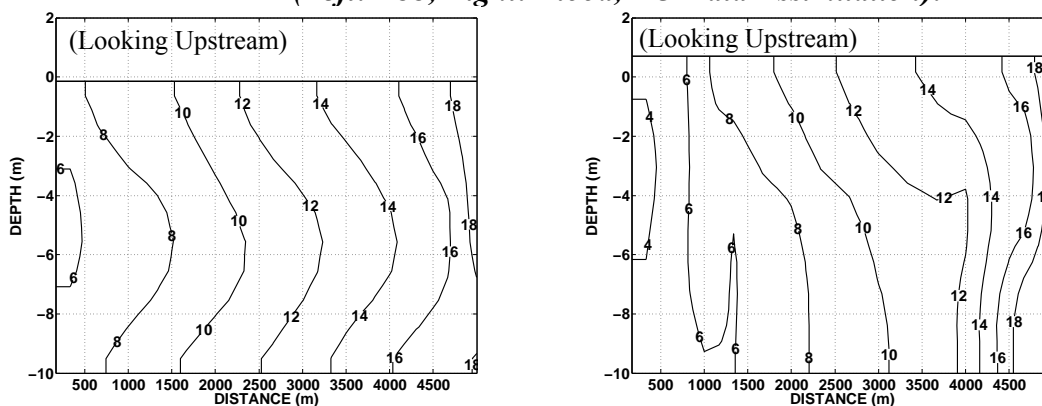
Figure: 7.20. Curved estuary: across-channel salinity profile
(Case: 2 - River Discharge + Stratification + Tides)
(Left: Ebb, Right: Flood, Data Assimilation: +1.0 m s^{-1}).

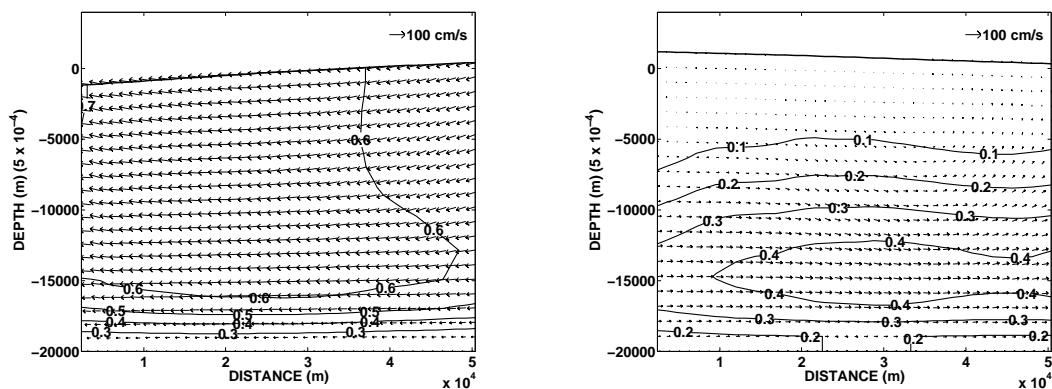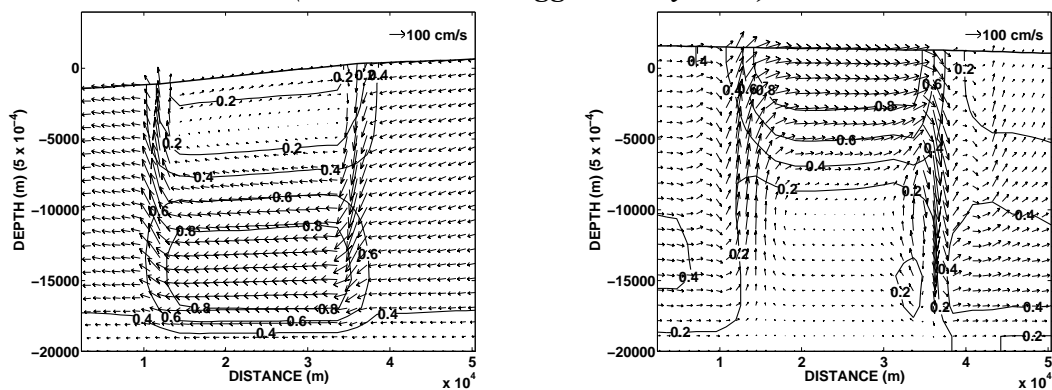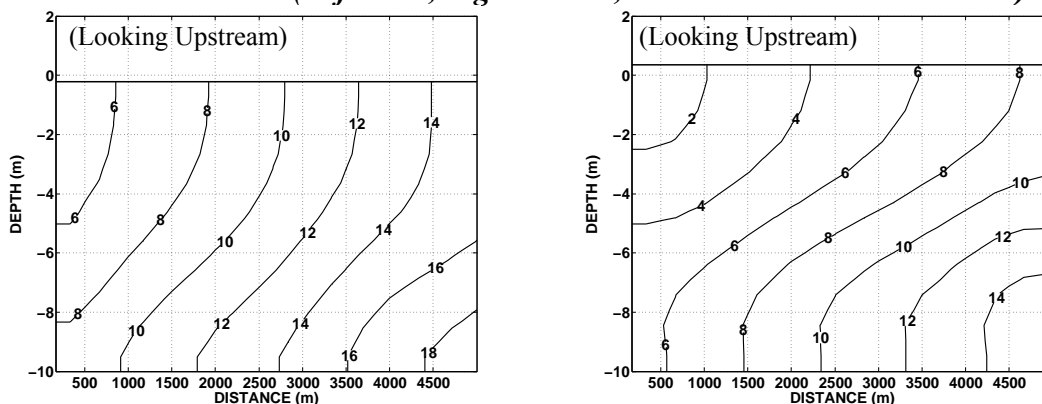
Figure: 7.21. Curved estuary: across-channel salinity profile
(Case: 2 - River Discharge + Stratification + Tides)
(Left: Ebb, Right: Flood, Data Assimilation: -1.0 m s^{-1}).

discharge forcing condition introduces a weakly developed anti-clockwise cell circulation with no significant modifications to near-bottom flow field within the DA domain. When M_2 tides and density stratification are introduced along with the river discharge forcing in the idealized long straight channel estuary, DA of (+1.0 m s^{-1}) represents a stronger clockwise circulation during flood tide than ebb tide within the DA domain, while DA of (-1.0 m s^{-1}) represents a stronger anti-clockwise circulation during ebb tide than flood tide within the DA domain. The DA affects the density stratification within the DA domain for the idealized long straight channel estuary. The DA of (+1.0 m s^{-1}) results in a weakly stratified estuarine condition within the DA domain due to strong vertical circulation, while DA of (-1.0 m s^{-1}) represents no significant effect in the vertical stratification due to weak vertical circulation.

The effect of DA on the along-channel sectional flow field for the case of curved estuary configuration with realistic forcing conditions of river discharge, tide, and density stratification is similar to that of long straight channel configuration. It should be noted that a stronger flow field is observed in the case of curved estuary than long straight channel, which can be due to the curvature effect. A more pronounced effect on density stratification is observed due to DA in the case of curved estuary compared to long straight channel. This increased effect on the density fields with respect to curved estuary is due to strong lateral circulation and vertical mixing.

In the case of across-channel sectional flow field, DA of (+1.0 m s^{-1}) accelerates the secondary circulation during flood tide and ebb tide conditions and a stronger lateral circulation is observed during ebb tide than during flood tide. In this case of DA of (+1.0

m s^{-1}), secondary circulation is mainly governed by the effect of DA rather than the effect of centrifugal force, and the reversal in the direction of secondary cell circulation within the tidal cycle is not observed. In the case of DA of (-1.0 m s^{-1}), secondary circulation is weaker than that of the no DA case. Because of strong secondary circulation due to DA of (+1.0 m s^{-1}), a vertically well-mixed estuarine condition is observed across the curved channel, unlike for the no DA case of near-bottom higher salinity water at the inner bank and near-surface lower salinity water at the outer bank. Across-channel density stratification for DA of (-1.0 m s^{-1}) follows a similar pattern as that of the no DA case due to weak secondary circulation.

The present study reveals the three-dimensional modifications of water parameters due to assimilation of surface currents into an estuarine and coastal ocean circulation model for idealized estuaries. The effect of nudging is significant in the case of assimilation of observed surface currents with higher magnitude and directed opposite with respect to model surface currents. The effect of nudging is moderate in the case of assimilation of observed surface currents with higher magnitude and directed in the direction of the model surface currents. The effect of DA on the three-dimensional circulation and density stratification suggests the need of a quality check of magnitude and direction of HF radar derived surface currents before assimilation into the NYHOPS model. The nudging scheme is robust and efficient, and can be easily implemented in the real–time DA of the NYHOPS forecast model with minimum computational burden.

Chapter 8

Standard-Range HF Radar Data Assimilation in the New York Harbor Domain

8.1   Introduction

This chapter describes the application of HF radar data by assimilating it into the NYHOPS model. The surface currents measured using standard-range HF radar network covering Raritan Bay and the NYB Apex are assimilated into the model using a nudging assimilation scheme. The continuous record of HF radar surface currents obtained at a temporal resolution of 0.5 hours were assimilated into the NYHOPS model for the model hindcasting cycle (-24 hours to 0 hours, see Chapter 5, Figure: 5.2). The focus of this DA experiment is to study the effectiveness of HF radar surface current assimilation with respect to NYHOPS model hindcasting capability (daily model simulations from -24 hours to 0 hours). HF radar data was assimilated into the NYHOPS model for a period of 40 days (February 24th - April 4th, 2007).

8.2 Data Assimilation Skill Assessment

The effectiveness of DA is evaluated by statistically comparing the assimilated model ($Model_A$) and non–assimilated model (free-model: $Model_F$) simulations (hindcast) with *in–situ* observations of three-dimensional currents, temperature, and salinity fields which are not used as part of the DA. The *DA skill* assessment is based on mean square error *(mse)*, which can be represented as the combination of the mean error *(MB)*, standard deviation error *(SDE)*, and cross-correlation *(CC)* [*Oke et al.,* 2002].

$$MSE = \frac{1}{n}\sum_{i=1}^{n}\left(m_i - o_i\right)^2 \tag{8.1}$$

$$MSE = MB^2 + SDE^2 + 2S_m S_o (1 - CC) \tag{8.2}$$

$$MB = \left(\overline{m} - \overline{o}\right) \tag{8.3}$$

$$SDE = (S_m - S_o) \tag{8.4}$$

$$CC = S_m^{-1} S_o^{-1} \frac{1}{n}\sum_{i=1}^{n}\left(m_i - \overline{m}\right)\left(o_i - \overline{o}\right) \tag{8.5}$$

$$DA \ \ skill = 1 - \left(MSE_A / MSE_F\right) \tag{8.6}$$

Where MSE_A is the mean square error between the assimilated model simulation and the *in-situ* observation, MSE_F is the mean square error between the non–assimilated (free) model simulation and the *in-situ* observation, *m* represents the model*,* and *o* represents the observation. The *DA skill* represents a single number which determines the effect of DA in the model performance. The *DA skill* > 0, when MSE_A < MSE_F (positive skill), and

DA skill = 0, when MSE_A = MSE_F (no skill), *DA skill* < 0, when MSE_A > MSE_F (negative skill), and   *DA skill* = 1, when MSE_A = *0* (perfect agreement between assimilated model and *in-situ* observation). A positive *DA skill* (0 – 100%) represents an improvement in the model performance by HF radar DA. The *DA skill* with respect to three-dimensional currents is computed by comparing assimilated and non–assimilated model currents with the mooring data (M1, M2, and M3: the mooring details are provided in Table: 4.2, Page 65 of Chapter 4 of this thesis), and surface currents obtained from one drifter for the period of February 24th - April 4th, 2007. The *DA skill* with respect to three-dimensional temperature (T) and salinity (S) fields is obtained by comparing assimilated and non–assimilated model T and S simulations with two Slocum Glider T and S data sets for the period of March 2007. The *DA skill* is also assessed with respect to fixed sensor *in–situ* T observations at six locations for the period of February 24th - April 4th, 2007.

8.3   Results and Discussion

8.3.1 Data Assimilation Skill Based on Mooring Data

The *DA skill* for the *u* and *v* component with respect to M1 current profile, and the complex correlation magnitude ρ and phase θ between assimilated/non-assimilated
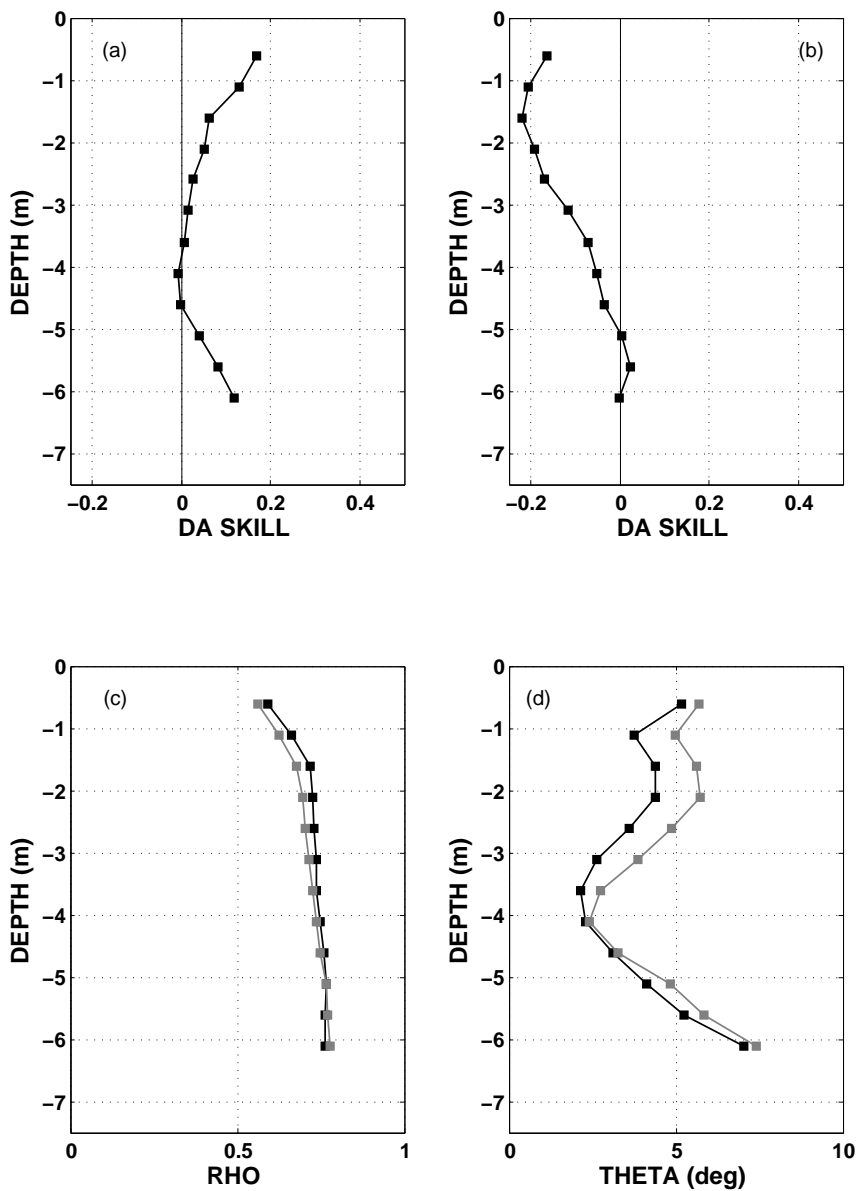
Figure: 8.1. **Data assimilation skill (black square) with respect to M1 data for the**

u (a) and v (b) component, and complex correlation [complex

correlation magnitude ρ (c), and complex correlation phase θ (d)]

between non-assimilated model and M1 data (black square) and

assimilated model and M1 data (gray square).

model currents and M1 current profile are shown in Figure: 8.1. HF radar DA represents a *DA skill* of +17% for the u component and -16% for the v component with respect to near-surface layers. The plot showing magnitude ρ and phase θ of complex correlation fails to represent any improvement in the model performance by DA. The mean and standard deviation for the u and v component of assimilated model currents, non-assimilated model currents, and M1 data are shown in Figure: 8.2. The DA represents no significant modifications to the mean and standard deviation for the u and v components of the model at M1 location. The *DA skill* for the u and v component with respect to M2 current profile, and the complex correlation magnitude ρ and phase θ between assimilated/non-assimilated model currents and M2 current profile are shown in Figure: 8.3. The *DA skill* with respect to M2 mooring data represents a significant improvement in the model performance by DA for the near-surface layers. A *DA skill* of +27% for the u component and +16% for the v component were achieved. The DA increases the magnitude of the complex correlation ρ and increases the average veering angle θ between model currents and M2 current profile. The mean and standard deviation for the u and v component of assimilated model currents, non-assimilated model currents, and M2 data are shown in Figure: 8.4. The DA represents a decrease in the mean for the u and v components of the model currents for the near-surface layers at M2 location, while the standard deviation for the u and v components of the model currents at M2 location remains the same.
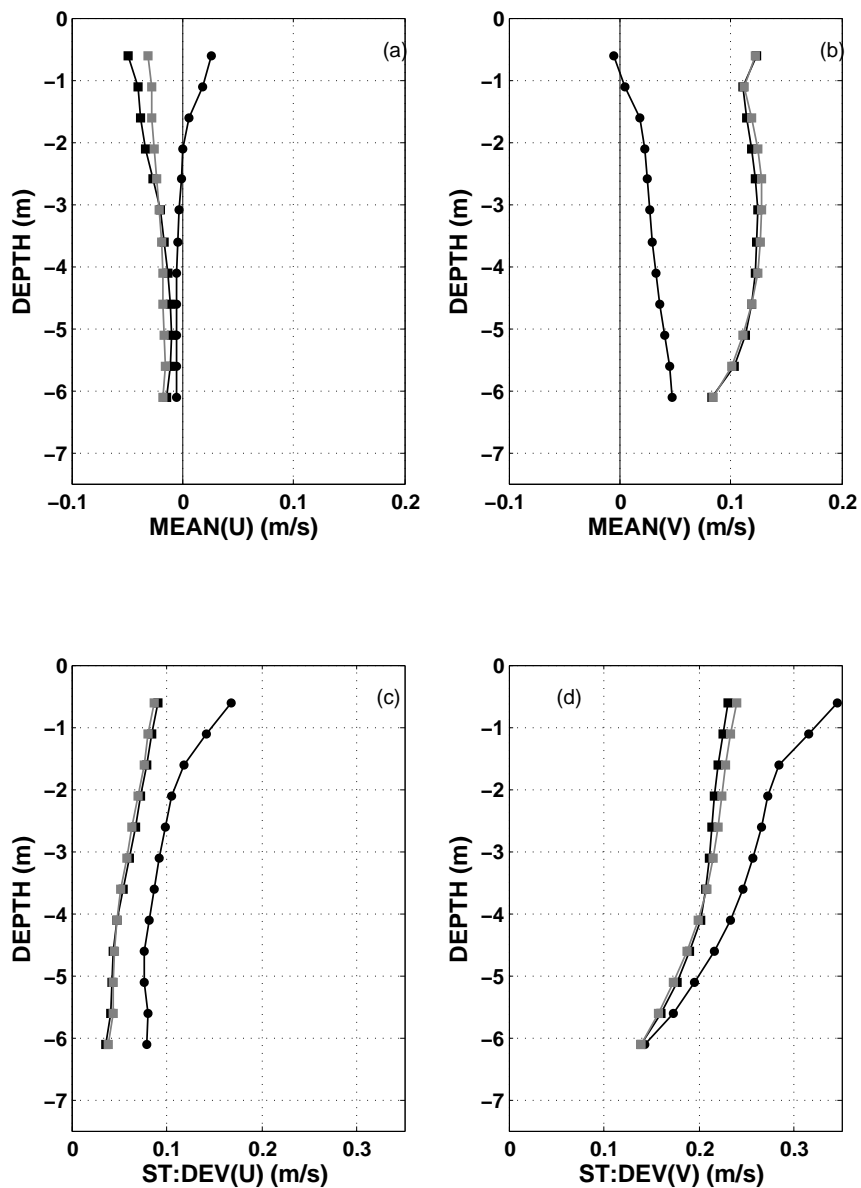
Figure: 8.2. Mean of *u* (a) and *v* (b) of non-assimilated model (black square), assimilated model (gray square), and M1 data (black circle), and standard deviation of *u* (c) and *v* (d) of non-assimilated model (black square), assimilated model (gray square), and M1 data (black circle).
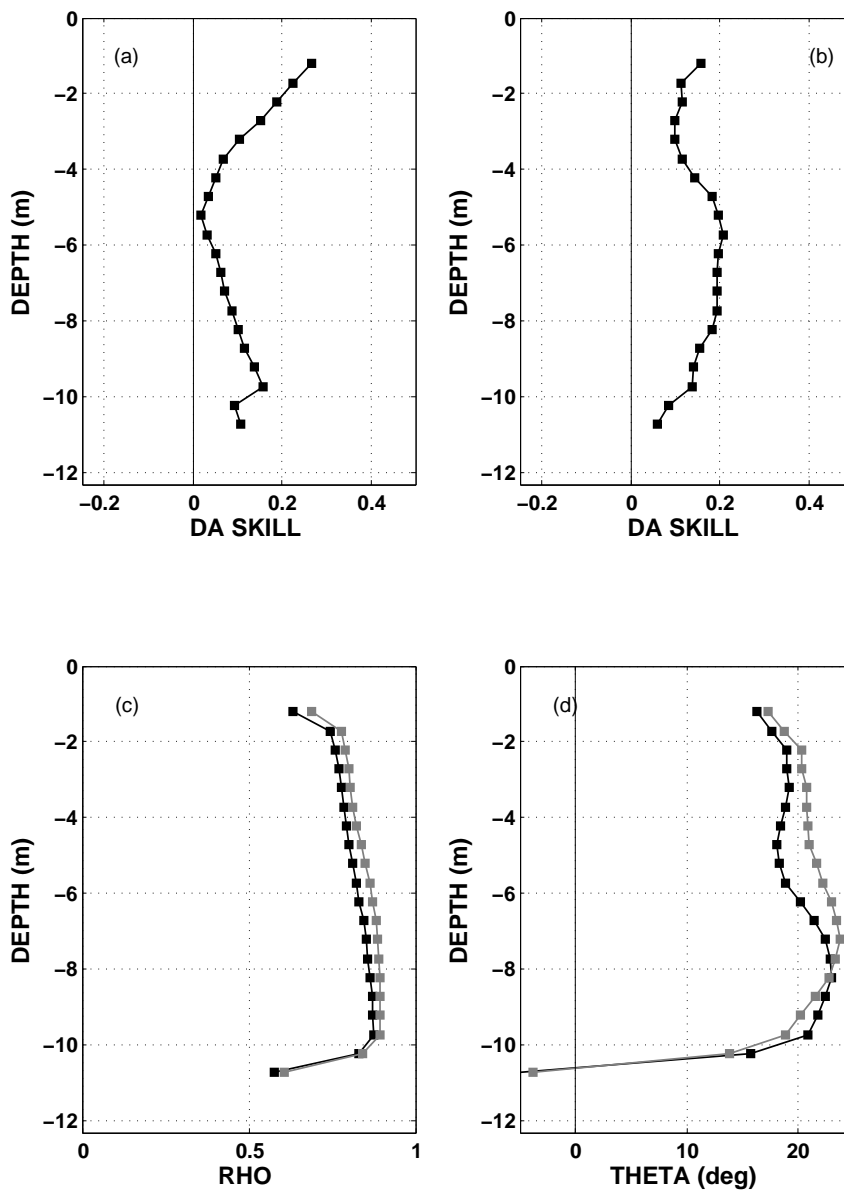
Figure: 8.3. Data assimilation skill (black square) with respect to M2 data for the *u* (a) and *v* (b) component, and complex correlation [complex correlation magnitude ρ (c), and complex correlation phase θ (d)] between non-assimilated model and M2 data (black square) and assimilated model and M2 data (gray square).
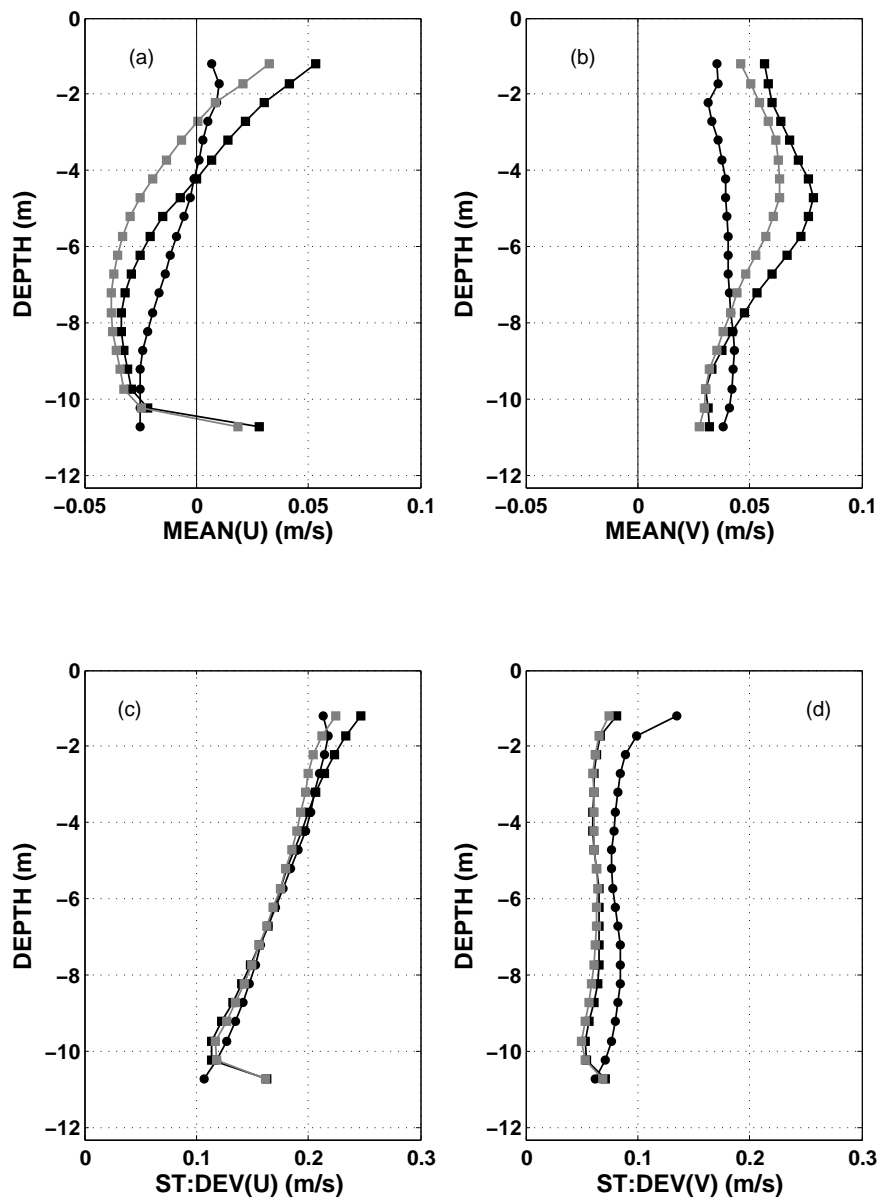
Figure: 8.4. Mean of *u* (a) and *v* (b) of non-assimilated model (black square), assimilated model (gray square), and M2 data (black circle), and standard deviation of *u* (c) and *v* (d) of non-assimilated model (black square), assimilated model (gray square), and M2 data (black circle).

The *DA skill* for the *u* and *v* components with respect to M3 mooring data, and complex correlations (ρ,θ) between assimilated/non-assimilated model and M3 current profile (data upto 10 m from the head of the instrument) were computed and shown in Figure: 8.5. HF radar DA significantly improves the model performance and a *DA skill* of +50% for the *u* component and +21% for the *v* component were achieved at a depth of 6.0 m from the surface. The DA increases the magnitude of the complex correlation ρ and considerably decreases the average veering angle θ between model currents and M3 current profile. The mean and standard deviation for the *u* and *v* component of assimilated model currents, non-assimilated model currents, and M3 data are shown in Figure: 8.6. The DA represents a decrease in the mean for the *u* and *v* components of the model with respect to near-surface layers at M3 location, while the standard deviation for the *u* and *v* components of the model currents at M3 location remains the same.

8.3.2 Data Assimilation Skill Based on Drifter Data

The assimilated and non-assimilated model surface currents were compared with surface currents obtained from a drifter in the region outside the assimilation domain. A surface drifter (SLDMB) was deployed by the United States Coast Guard (USCG) during the period of February 24th - April 4th, 2007 at the mid-NJ shelf region. The drifter trajectory along with the bathymetric contours and coastline are shown in Figure: 8.7.
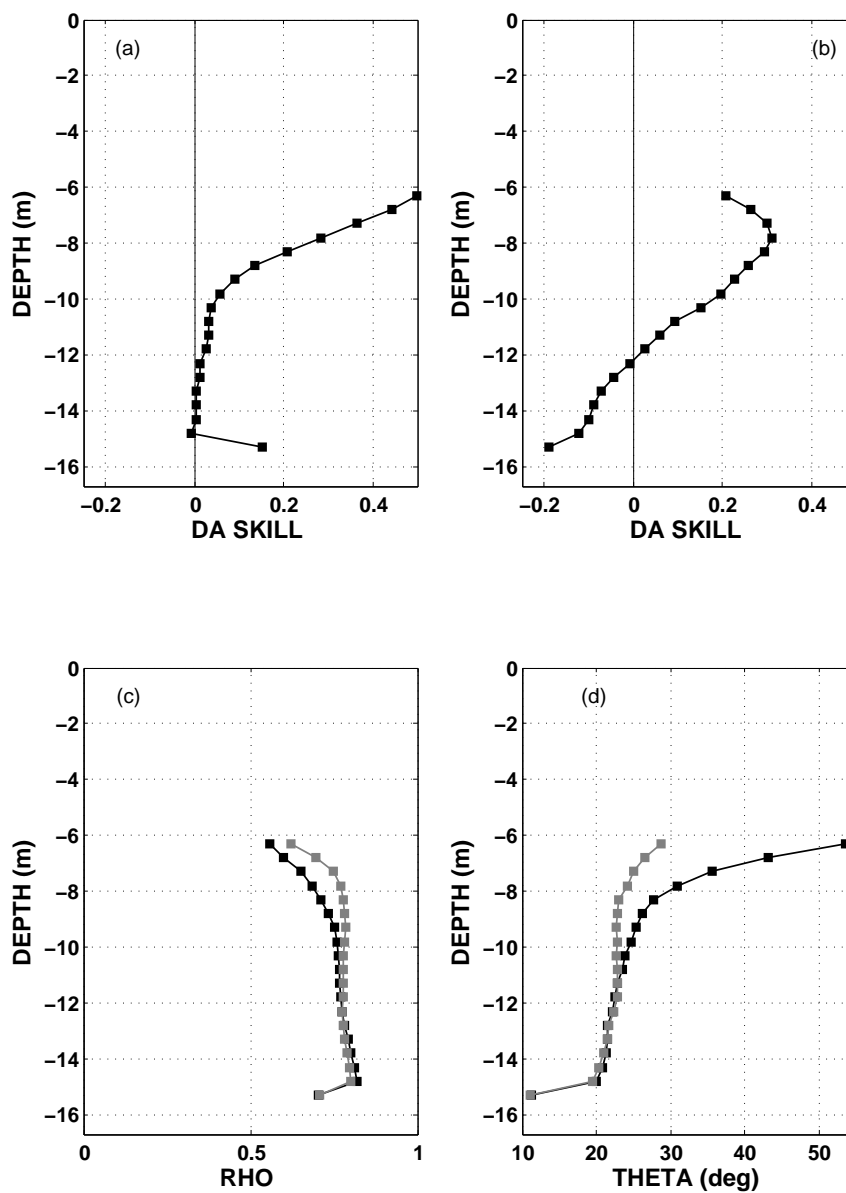
Figure: 8.5. **Data assimilation skill (black square) with respect to M3 data for the**

u (a) and v (b) component, and complex correlation [complex

correlation magnitude ρ (c), and complex correlation phase θ (d)]

between non-assimilated model and M3 data (black square) and

assimilated model and M3 data (gray square).
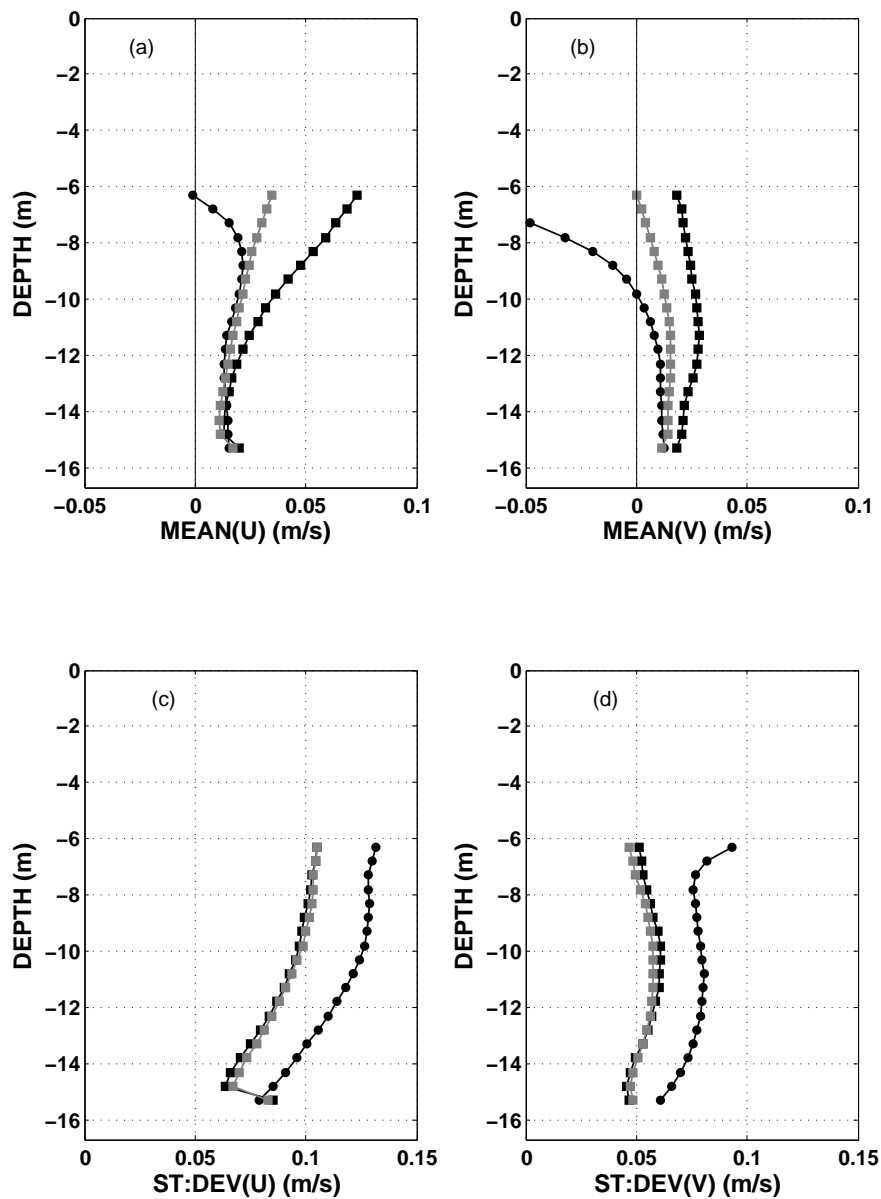
Figure: 8.6. **Mean of *u* (a) and *v* (b) of non-assimilated model (black square), assimilated model (gray square), and M3 data (black circle), and standard deviation of *u* (c) and *v* (d) of non-assimilated model (black square), assimilated model (gray square), and M3 data (black circle).**
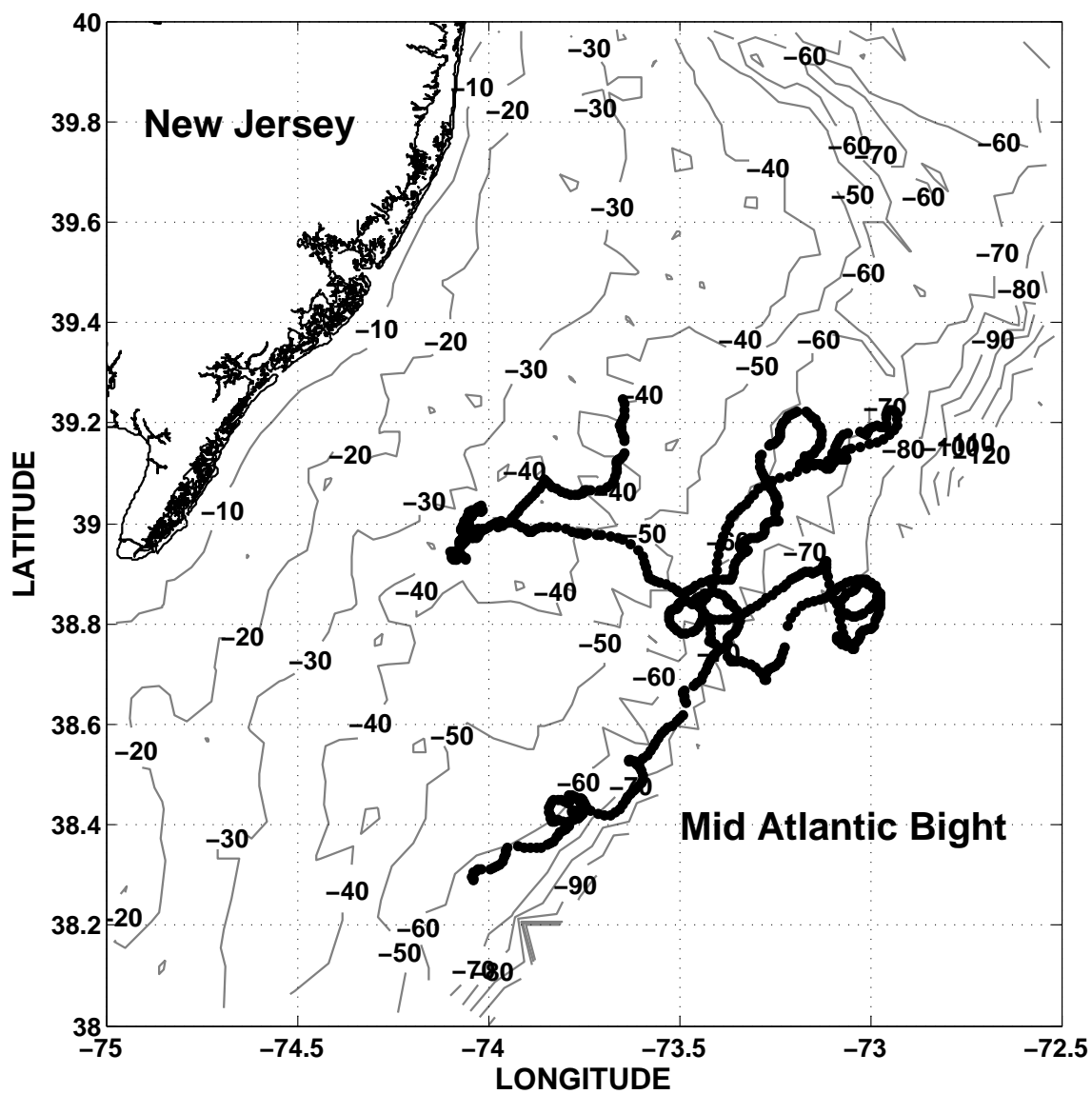
Figure: 8.7.   Drifter trajectory (black circles), along with bathymetric contours (in meters) and NJ coastline.

The raw drifter data consists of GPS locations of longitude and latitude, and corresponding time stamp for each drifter position. From this drifter position information and from the time taken by the drifter to traverse from one position to other, velocity of surface water is computed with respect to east-west (u) and north-south (v) direction. The processed drifter data consists of surface currents of u (east-west) and v (north-south) components, averaged over an hour and outputted at every 30 minutes. The processed drifter data are compared with assimilated and non-assimilated surface currents with respect to space and time. The time-series comparison for u component and v component between drifter data, non-assimilated model, and assimilated model currents are shown in Figure: 8.8. The correlation values between assimilated and non-assimilated model surface currents and drifter data are tabulated and shown in Table: 8.1. The comparison shows a good correlation between drifter data and assimilated and non-assimilated model currents, and the DA improves the model performance with a *DA skill* of +6% for the u component and +1% for the v component (Table: 8.1).

8.3.3 Data Assimilation Skill Based on Slocum Glider Data

Effectiveness of DA with respect to three-dimensional T and S distributions in the regions outside the assimilation domain was studied by comparing the assimilated and non-assimilated model T and S profiles with Slocum Glider T and S data. Rutgers University deployed two Gliders during the period of March 2007. The Glider flight
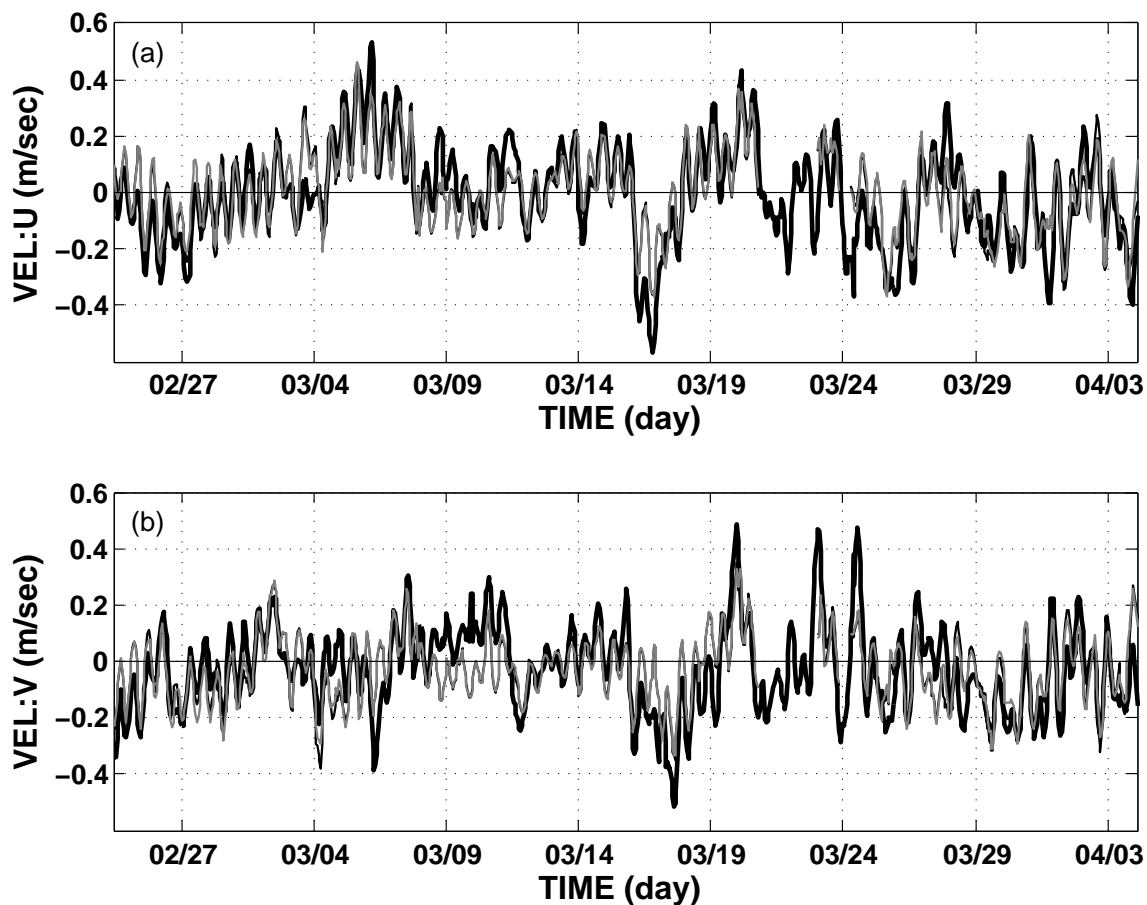
Figure: 8.8. Time-series comparison for the *u* (a) and *v* (b) component of the surface current obtained from surface drifter, non-assimilated model, and assimilated model. (Thick black lines indicate drifter, thin black line indicate non-assimilated model, and gray lines indicate assimilated model).

Table: 8.1. **Correlation values between assimilated and non-assimilated model currents, and drifter data.**

	Drifter data					
	r^2 (u)	r^2 (v)	rmse(u) (m s^{-1})	rmse(v) (m s^{-1})	rho (ρ)	theta: θ (degrees)
Model$_F$ *(NO assimilation)*	*0.68*	*0.50*	*0.10*	*0.11*	*0.78*	*3.52*
Model$_A$ *(HF radar data assimilation)*	*0.70*	*0.51*	*0.09*	*0.11*	*0.79*	*3.42*
DA skill *(East – West : u component)*	*+6%*					
DA skill *(North – South : v component)*	*+1%*					
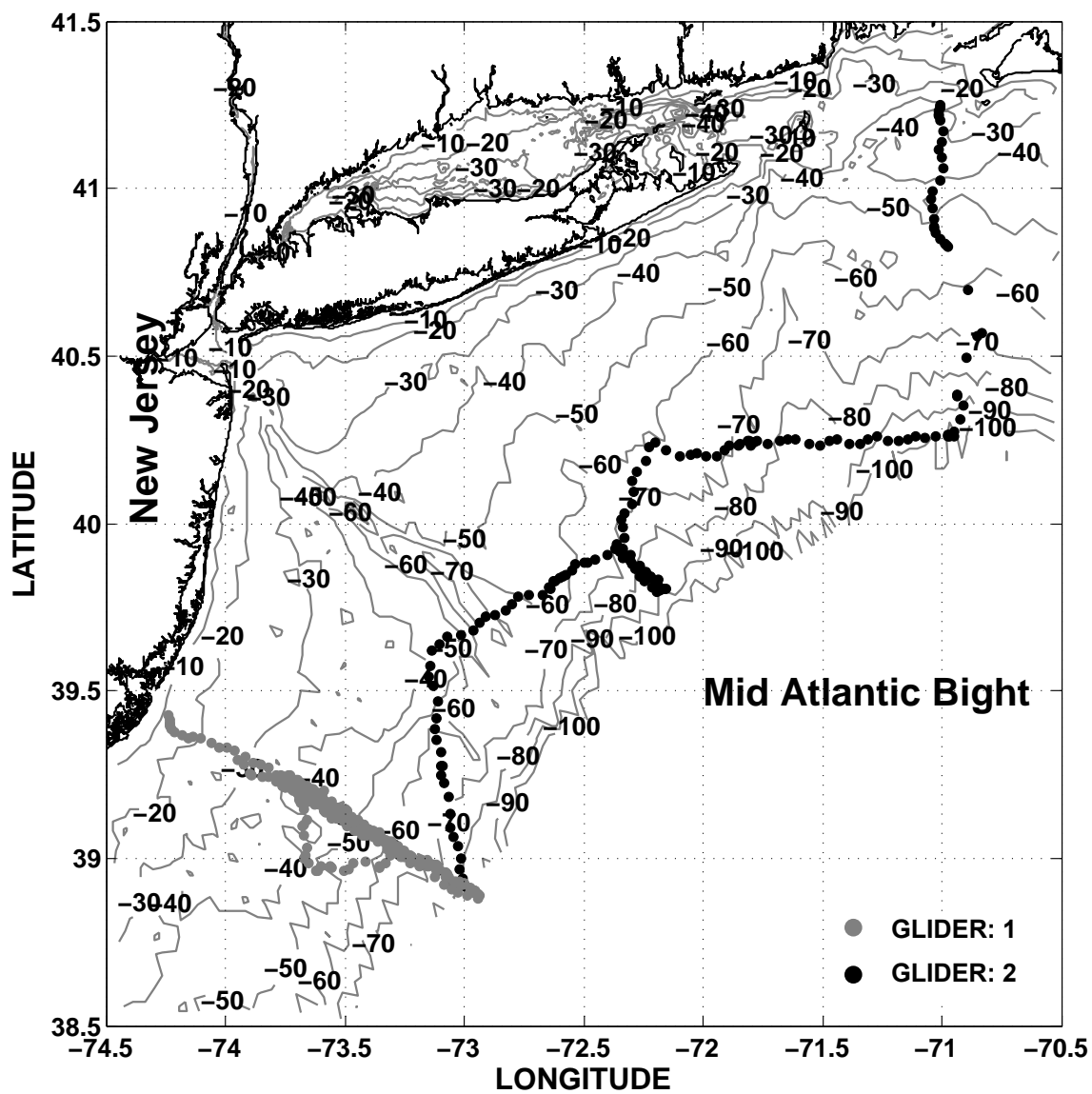
Figure: 8.9.   Glider flight trajectory along with bathymetric contours and NJ coastline.

trajectory along with the bathymetric contours and the NJ coastline are shown in Figure: 8.9. The Glider: 1 flight (03/07/2007 – 04/03/2007) was across the NJ shelf with Glider trajectory extending from the inner-NJ shelf at Great Bay, south of NJ coastal ocean; to the outer-NJ shelf upto a depth of 100 m. The Glider: 2 flight (03/13/2007 – 04/06/2007) was along the mid-NJ shelf region, with Glider trajectory extending from the Great Bay, south of NJ coastal ocean; to the Nantucket Islands, MA. The improvement in the model hindcasting performance by HF radar DA is studied by computing the *DA skill* with respect to three-dimensional T and S fields. The Glider T and S profiles were hourly averaged over time and vertically averaged over depth at every meter from the surface. The NYHOPS model T and S profiles were hourly averaged and vertically interpolated over depth at every meter from the surface similar to Glider T and S profiles. The *DA skill* is based on mean square error *(mse)* between assimilated model T and S profiles and Glider T and S profiles *(MSE_A)*, and non-assimilated model T and S profiles and Glider T and S profiles *(MSE_F)*. The *DA skill* (Equation 8.6) for T and S is computed as a function of the depth for the regions of inner-NJ shelf *(0-30 m)* and mid-NJ shelf *(30-90 m)* for the whole period (March 2007) of Glider flights. The *DA skill* for T and S fields at the inner-NJ shelf region with respect to Glider: 1 is shown in Figure: 8.10a. In the inner-NJ shelf region, DA shows considerable improvement in hindcasting T than S with respect to near-surface layers [*DA skill* (T): +53%, *DA skill* (S): +38%]. The *DA skill* for T and S fields in the mid-NJ shelf region with respect to Glider: 2 is shown in Figure: 8.10b. The DA shows a moderate improvement in hindcasting T (*DA skill*: +5%) and no improvement in hindcasting S (*DA skill*: -5%) in the mid-NJ shelf region.
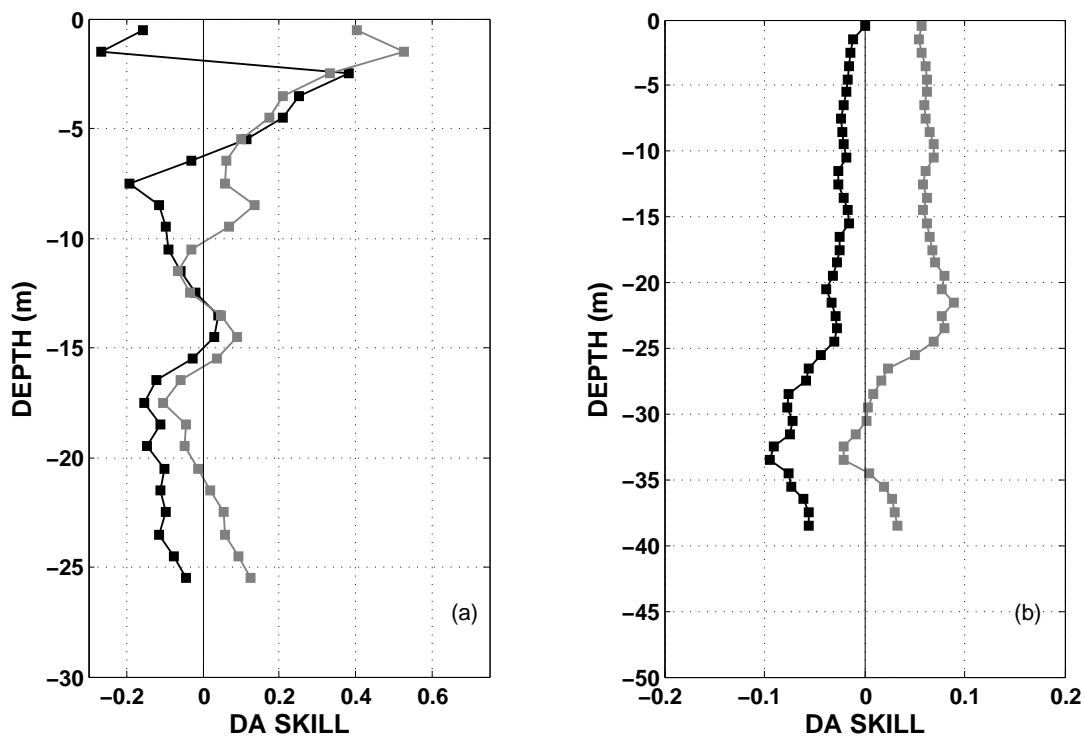
Figure: 8.10. **Data assimilation skill with respect to Glider: 1 data for the inner-shelf region (a) and with respect to Glider: 2 data for the mid-shelf region (b). (Black square represents salinity and gray square represents temperature).**

8.3.4 Data Assimilation Skill Based on Fixed Sensor Temperature

Observations

The assimilated and non–assimilated model T were compared with fixed sensor *in–situ* T observations obtained from NOS stations (BATN6 and SDHN4), SIT station (STBLD4), and mooring stations (M1, M2, and M3). The computed *DA skill* with respect to T observations were tabulated and shown in Table: 8.2. The surface elevation at the Battery: BATN6 representing the spring-neap tidal variability is shown in Figure: 8.11a. The assimilated and non-assimilated model T were compared with the Battery: BATN6 data and the Sandy Hook: SDHN4 data and the plots are shown in Figure: 8.11b and Figure: 8.11c respectively. The assimilated model T shows a better comparison with *in–situ* observations than non-assimilate model T, representing an enhancement in the model performance by DA. The sea-bottom T comparisons with Belford: STBLD4 data, M1, M2, and M3 data are shown in Figure: 8.12. At all the four stations assimilated model simulations shows a better comparison with *in–situ* observations than non-assimilated simulations, representing an improvement in the model performance by DA.
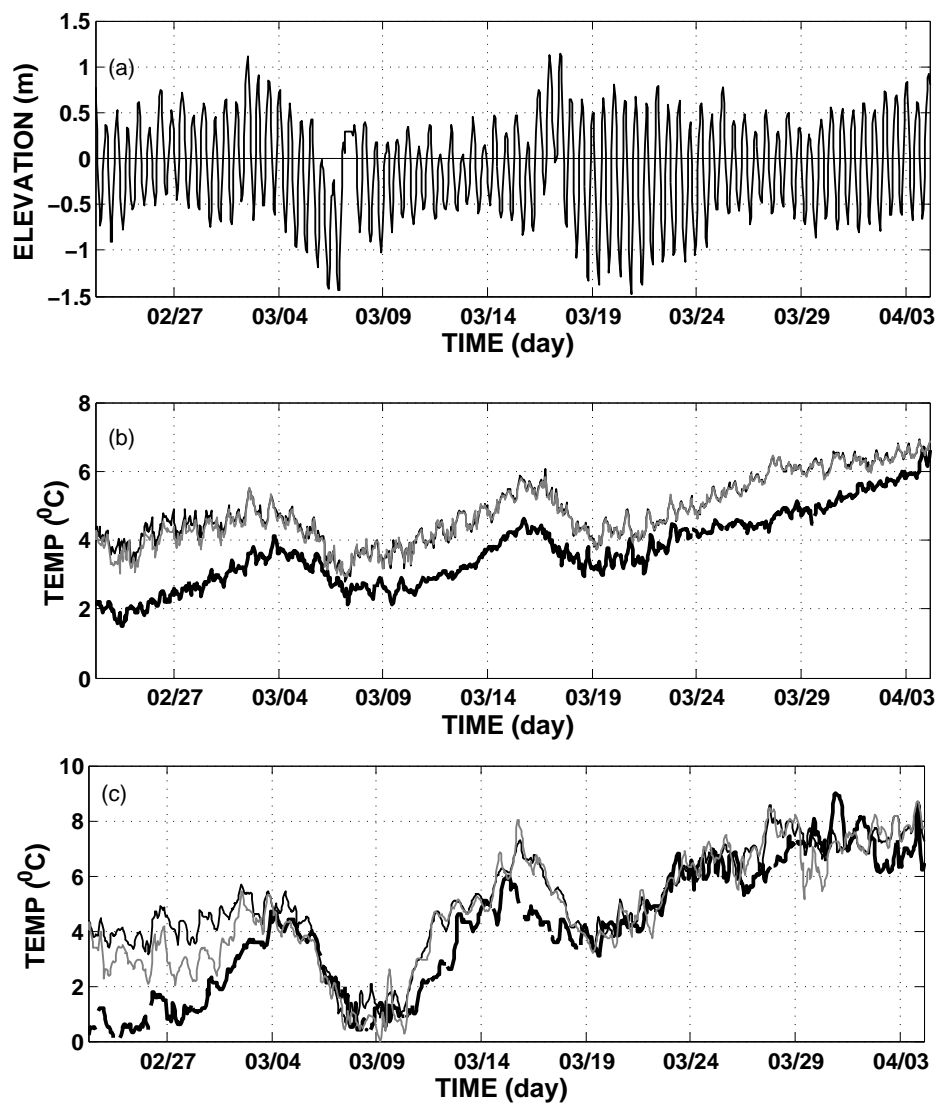
Figure: 8.11. Sea-surface elevation at the Battery: BATN6 (a), time-series comparison for sea-surface temperature obtained from assimilated model (gray line), non-assimilated model (thin black line), and *in-situ* observation (thick black line) at the Battery: BATN6 (b), at Sandy Hook: SDHN4 (c).
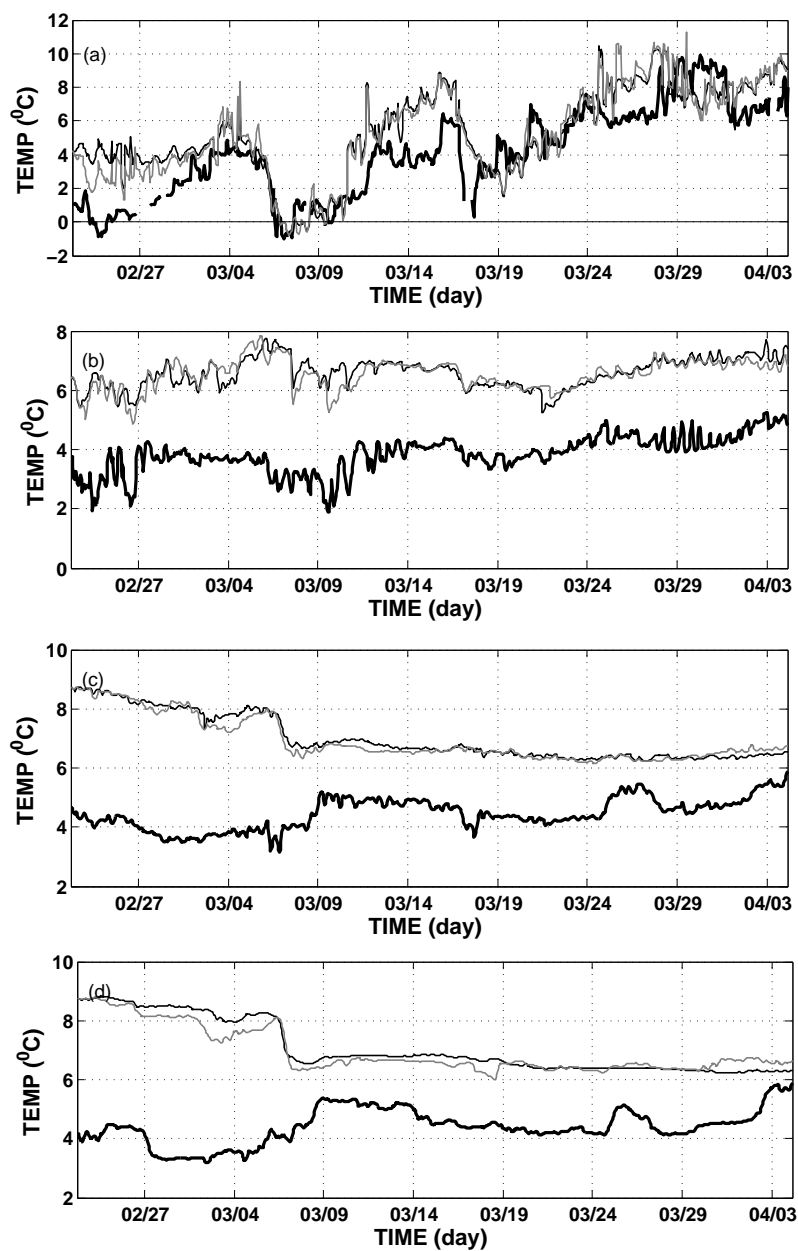
Figure: 8.12. Time-series comparison for sea-bottom temperature obtained from assimilated model (gray line), non-assimilated model (thin black line), and *in-situ* observation (thick black line) at Belford: STBLD4 (a), Mooring: 1 station (b), Mooring: 2 station (c), and Mooring: 3 station (d).

Table: 8.2. **Data assimilation skill (Hindcast) of the NYHOPS model**

(Comparison with fixed sensor *in-situ* temperature observations).

Location	Station Name	Agency	Parameter	Depth	DA skill
The Battery, NY	*BATN6*	*NOS*	*Temperature*	*Surface*	*+11%*
Sandy Hook, NJ	*SDHN4*	*NOS*	*Temperature*	*Surface*	*+34%*
Belford, NJ	*STBLD4*	*SIT*	*Temperature*	*Bottom*	*+12%*
Mooring: 1	*M1*	*RU*	*Temperature*	*Bottom*	*+4%*
Mooring: 2	*M2*	*RU*	*Temperature*	*Bottom*	*+5%*
Mooring: 3	*M3*	*RU*	*Temperature*	*Bottom*	*+11%*

8.4   Conclusions

Surface currents measured using standard-range HF radar network in Raritan Bay and the NYB Apex were assimilated into the NYHOPS model for a period of 40 days (February 24th - April 4th, 2007) using a nudging scheme. The effectiveness of DA in enhancing the model performance is evaluated by computing the *DA skill* and a positive *DA skill* (0 – 100%) represents an improvement in the model performance. The *DA skill* is based on mean square error between assimilated/non-assimilated model simulations and *in–situ* observations of three–dimensional currents, T, and S, which are not used as part of the DA. This standard-range HF radar DA experiment focused on the hindcasting capability (daily model simulations from -24 hours to 0 hours) of the NYHOPS model. The *DA skill* is computed by comparing assimilated and non-assimilated model results with three–dimensional currents obtained from three moorings, surface currents obtained from one drifter, three–dimensional T and S fields obtained from two Slocum Gliders, and fixed sensor *in-situ* T observations at six locations.

The HF radar DA improved the model hindcasts for three-dimensional currents based on the *DA skill* values with respect to M2 and M3 mooring data. A *DA skill* of +27% and +16% for *u* and *v* component is achieved with respect to M2 data for the near-surface layers, and a *DA skill* of +50% and +21% for *u* and *v* component is achieved with respect to M3 data at a depth of 6.0 m from the surface. The *DA skill* values with respect to M1 data showed only a marginal improvement in the model performance by DA. This can be related to the proximity of M1 location to the shore. The HF radar data validation

results (see Chapter 4, Page 79) showed a higher correlation with respect to M2 data than M1 data. The moderate correlation of HF radar surface currents with M1 near-surface bin currents also influences the assimilated model performance at the M1 location.

The comparison of assimilated and non-assimilated model surface currents with surface currents obtained from drifters represented a good correlation between the model and the data. The HF radar DA improved the model hindcasts for surface currents and a *DA skill* of +6% and +1% for *u* and *v* component is achieved with respect to drifter data. The drifter trajectory falls outside the assimilation domain and the improvement in the model performance suggests the influence of HF radar DA beyond the assimilation domain.

The modifications to three-dimensional T and S fields due to DA were studied by comparing assimilated and non-assimilated model T and S simulations with T and S fields obtained from two Slocum Gliders. The *DA skill*, based on mean square error, is computed for T and S with respect to inner-NJ shelf and mid-NJ shelf regions as a function of water depth. A *DA skill* of +53% and +38% is achieved in hindcasting T and S with respect to near-surface layers in the inner-NJ shelf region, while the *DA skill* values for the mid-NJ shelf region showed no significant improvement in the model performance [*DA skill* (T): +5%, *DA skill* (S): -5%]. The Glider flights falls outside the assimilation domain and the improvement in the model performance suggests the influence of HF radar DA beyond the assimilation domain. The low *DA skill* values in the mid-NJ shelf regions can be associated with the model boundary conditions along the

open ocean boundary at the mid-NJ shelf region, and also due to the influence of offshore climatological boundary conditions.

The *DA skill* is also computed with respect to fixed sensor *in-situ* T observations at six locations. The DA showed pronounced improvement in hindcasting sea-surface T (*DA skill* of +34% at SDHN4 station).

In all the comparison studies for the *DA skill* with respect to T and S fields, the *DA skill* values for T fields were found to be higher than S fields. This difference in the model performance with respect to T and S fields needs to be studied in detail with more DA experiments into the NYHOPS model. The nudging assimilation scheme is found to be robust and efficient for the NYHOPS model with minimum computational burden. The HF radar DA is extended to the NYHOPS model forecasting experiment and validated with more *in–situ* observations, which is explained in detail in Chapter 9 of this thesis.

Chapter 9

Long-Range HF Radar Data Assimilation in the New York Bight Domain

9.1   Introduction

This chapter describes the assimilation of HF radar surface currents covering the NYB domain into the NYHOPS model. The surface current data for the NYB domain is obtained by a long-range HF radar network consisting of eight CODAR sites located along the NY/NJ coast. The long-range HF radar network specifications for the NYB domain are tabulated and shown in the Table: 9.1. The HF radar data are assimilated into the model using a nudging assimilation scheme. The continuous record of HF radar surface currents obtained at a temporal resolution of 1.0 hour are assimilated into the NYHOPS model for the model hindcasting cycle (-24 hours to 0 hours, see Chapter 5, Figure: 5.2). The focus of this DA experiment is to study the effectiveness of HF radar surface current assimilation with respect to model forecasting capability (daily model simulations from 0 hours to 24 hours). HF radar data were assimilated into the NYHOPS model for a period of 120 days (March 2nd - June 29th, 2007).

Table: 9.1.   Specifications of the long-range HF radar network for the NYB domain.

Site No	1	2	3	4	5	6	7	8
Deployment Site	Sandy Hook, NJ (HOOK)	Moriches, NY (MRCH)	Loveladiess, NJ (LOVE)	Wildwood, NJ (WILD)	Tuckerton, NJ (GRHD)	Sandy Hook, NJ (HOMR)	Sandy Hook, NJ (HOSR)	Breezy Point, NJ (BRZY)
HF radar Type	CODAR Seasonde Long-Range	CODAR Seasonde Long-Range	CODAR Seasonde Long-Range	CODAR Seasonde Long-Range	CODAR Seasonde Long-Range	CODAR Seasonde Medium-Range	CODAR Seasonde Standard-Range	CODAR Seasonde Standard-Range
Collaborator	Rutgers University	Rutgers University	Rutgers University	Rutgers University	Rutgers University	Rutgers University	Rutgers University	Rutgers University
Latitude	40.4332 N	40.7882 N	39.7362 N	38.9537 N	39.5085 N	40.4326 N	40.4322 N	40.5616 N
Longitude	73.9838 W	72.7452 W	74.1171 W	74.8532 W	74.3243 W	73.9840 W	73.9836 W	73.8826 W
Transmitting Frequency	4.89 MHz	4.80 MHz	4.89 MHz	4.69 MHz	4.79 MHz	13.46 MHz	24.65 MHz	24.65 MHz
Resonant Bragg Condition	$\lambda_{radar} = 60\ m$ $\lambda_{wave} = 30\ m$	$\lambda_{radar} = 60\ m$ $\lambda_{wave} = 30\ m$	$\lambda_{radar} = 60\ m$ $\lambda_{wave} = 30\ m$	$\lambda_{radar} = 60\ m$ $\lambda_{wave} = 30\ m$	$\lambda_{radar} = 60\ m$ $\lambda_{wave} = 30\ m$	$\lambda_{radar} = 25\ m$ $\lambda_{wave} = 12.5\ m$	$\lambda_{radar} = 12\ m$ $\lambda_{wave} = 6\ m$	$\lambda_{radar} = 12\ m$ $\lambda_{wave} = 6\ m$
Sweep Rate	1 Hz	1 Hz	1 Hz	1 Hz	1 Hz	2 Hz	2 Hz	2 Hz
Sweep Width	25 KHz	25 KHz	25 KHz	25 KHz	25 KHz	100 KHz	100 KHz	100 KHz
Radial Range	180 km	180 km	180 km	180 km	180 km	60 km	40 km	40 km
Radial Coverage	0^0 - 360^0	0^0 - 360^0	0^0 - 360^0	0^0 - 360^0	0^0 - 360^0	0^0 - 360^0	0^0 - 360^0	0^0 - 360^0
Radial Bin	6 km	6 km	6 km	6 km	6 km	1.5 km	1.5 km	1.5 km
Radial Bearing Increment	5^0	5^0	5^0	5^0	5^0	5^0	5^0	5^0
Average Depth of Measurement	2.4 m	2.4 m	2.4 m	2.4 m	2.4 m	1.0 m	0.5 m	0.5 m

The enhancement in the NYHOPS model forecasts by HF radar DA is studied with respect to model simulation for 120 days (March 2nd - June 29th, 2007). The long-range HF radar DA experiment also focuses on the flooding event that happened on April 15 - 16, 2007 along the NJ coast, and the *DA skill* is analyzed for this flooding event period (April 14th – 23rd, 2007). A typical surface current field for the NYB domain measured using eight HF radar stations along the NY/NJ coast is shown in Figure: 9.1.

9.2 Data Assimilation Skill Assessment

The effectiveness of DA is evaluated by statistically comparing the assimilated model (*Model$_A$*) and non–assimilated model (free-model: *Model$_F$*) simulations (first day forecast: daily model simulations from 0 hours to 24 hours) with *in-situ* observations which are not used as part of DA. The *DA skill* assessment is based on mean square error *(mse)* [*Oke et al.,* 2002] (see Chapter 8 for the *DA skill* equations, Page 128). A positive *DA skill* (0 – 100%) represents an improvement in the model performance by HF radar DA. The *DA skill* with respect to three-dimensional currents is computed by comparing assimilated and non–assimilated model currents with the mooring data (M1, M2, and M3: the mooring details are provided in Table: 4.2, Page 65 of Chapter 4 of this thesis) for the period of 53 days (March 2nd - April 23rd 2007). The *DA skill* with respect to three-dimensional temperature (T) and salinity (S) fields is obtained by comparing assimilated and non–assimilated model T and S simulations with four Slocum Glider T and S data sets obtained within the 120 days period of DA, and fixed sensor *in-situ* T
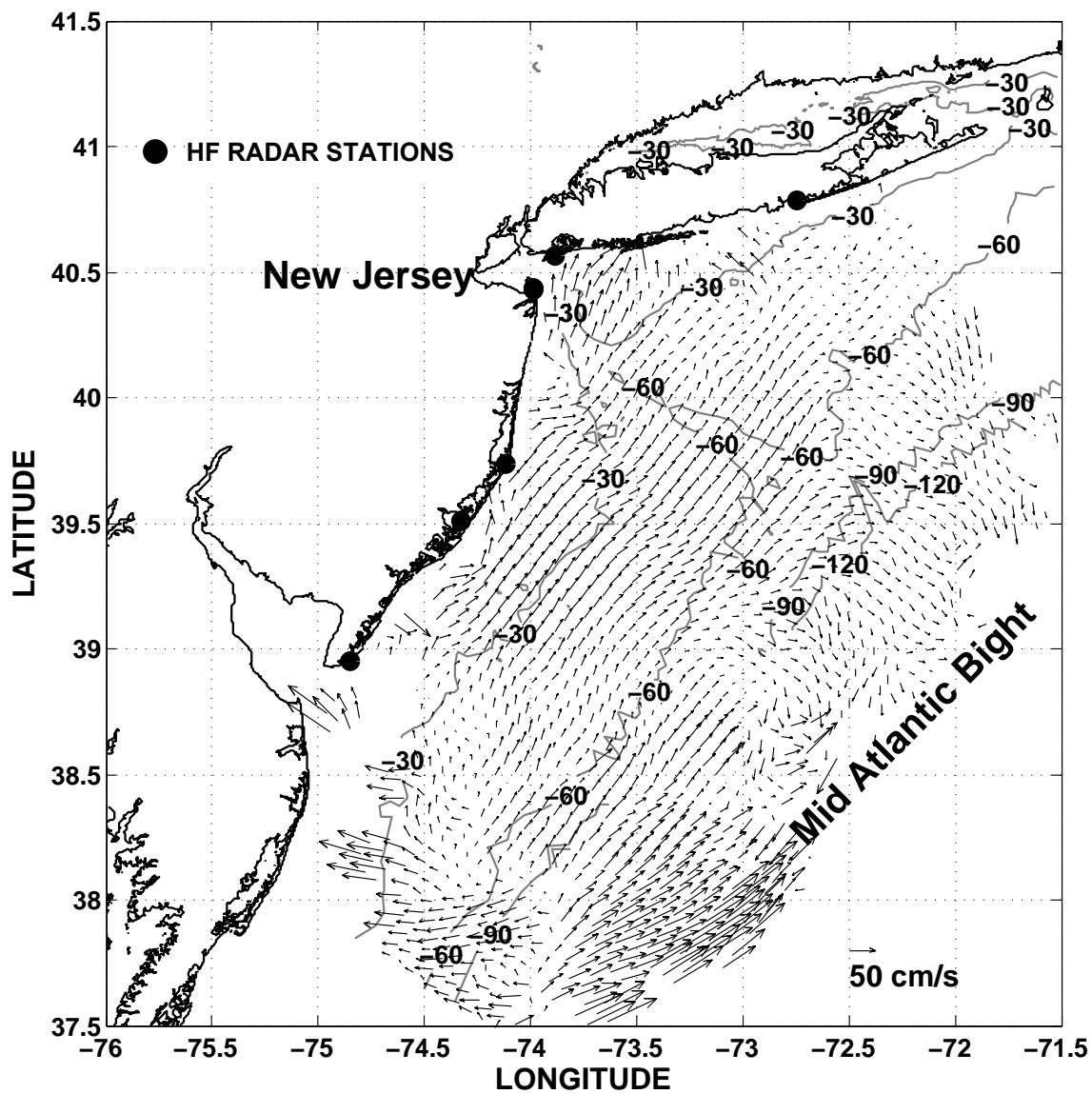
Figure: 9.1.   A typical HF radar total vector plot for the NYB domain (03/14/2007 19:00). (Black circle represents eight monostatic HF radar stations).

observations at eight locations and S observations at three locations for the 120 days period of DA.

9.3   Results and Discussion

9.3.1 Data Assimilation Skill Based on Mooring Data

The *DA skill* for the *u* and *v* component with respect to M1 current profile, and the complex correlation magnitude ρ and phase θ between assimilated/non-assimilated model currents and M1 current profile are shown in Figure: 9.2. A *DA skill* of +8% for the *v* component and -3% for the *u* component were achieved with respect to near-surface layers. The plot showing magnitude ρ and phase θ of complex correlation fails to represent any improvement in the model performance by DA. The *DA skill* for the *u* and *v* component with respect to M2 current profile, and the complex correlation magnitude ρ and phase θ between assimilated/non-assimilated model currents and M2 current profile are shown in the Figure: 9.3. The *DA skill* with respect to M2 mooring data represents a moderate improvement in the model performance by DA for the near-surface layers. A *DA skill* of +6% for the *u* component and +14% for the *v* component were achieved. DA fails to represent any significant modifications to the magnitude of the complex correlation ρ and the average veering angle θ between model currents and M2 current profile.
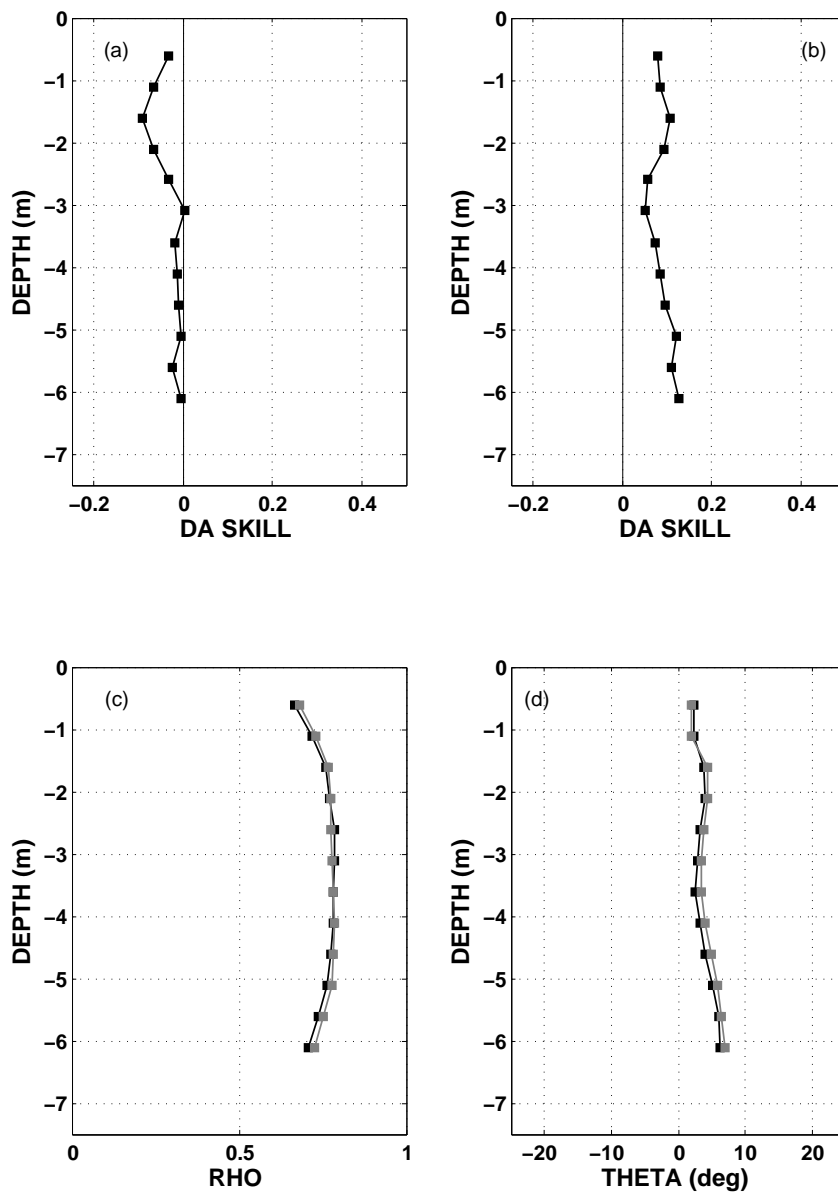
Figure: 9.2. **Data assimilation skill (black square) with respect to M1 data for the**
u (a) and v (b) component, and complex correlation [complex
correlation magnitude ρ (c), and complex correlation phase θ (d)]
between non-assimilated model and M1 data (black square) and
assimilated model and M1 data (gray square).
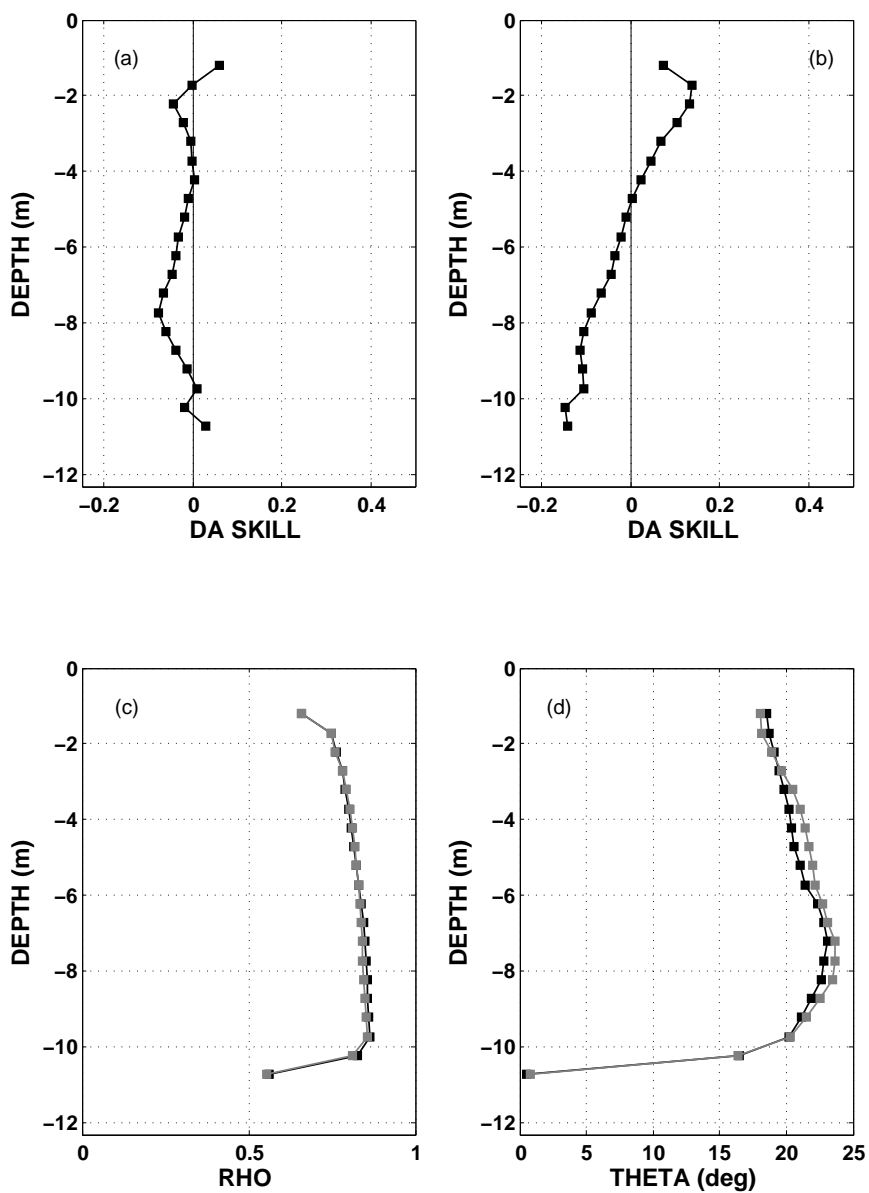
Figure: 9.3. Data assimilation skill (black square) with respect to M2 data for the *u* (a) and *v* (b) component, and complex correlation [complex correlation magnitude ρ (c), and complex correlation phase θ (d)] between non-assimilated model and M2 data (black square) and assimilated model and M2 data (gray square).

The *DA skill* for the *u* and *v* components with respect to M3 mooring data, and complex correlations (ρ, θ) between assimilated/non-assimilated model and M3 current profile (data upto 10 m from the head of the instrument) were computed and shown in Figure: 9.4. HF radar DA significantly improves the model performance and a *DA skill* of +26% for the *u* component and +10% for the *v* component were achieved at a depth of 6.0 m from the surface. The DA increases the magnitude of the complex correlation ρ and decreases the average veering angle θ between model currents and M3 current profile.

9.3.2 Data Assimilation Skill Based on Slocum Glider Data

Effectiveness of DA with respect to three-dimensional T and S distributions was examined by comparing the assimilated and non-assimilated model T and S profiles with Slocum Glider T and S data. Rutgers University (RU) deployed four Gliders during the period of March – May, 2007. The Glider flight trajectory along with the bathymetric contours and the NJ coastline are shown in Figure: 9.5. The flight of Glider: 1 (03/07/2007 – 04/03/2007) and Glider: 3 (04/03/2007 – 04/06/2007) was across the NJ shelf with the Glider trajectory extending from the inner-NJ shelf at Great Bay, south of NJ coastal ocean; to the outer-NJ shelf upto a depth of 100 m. The flight of Glider: 2 (03/13/2007 – 04/06/2007) and Glider: 4 (04/26/2007 – 05/21/2007) was along the mid-NJ shelf region, with the Glider trajectory extending from the Great Bay, south of NJ
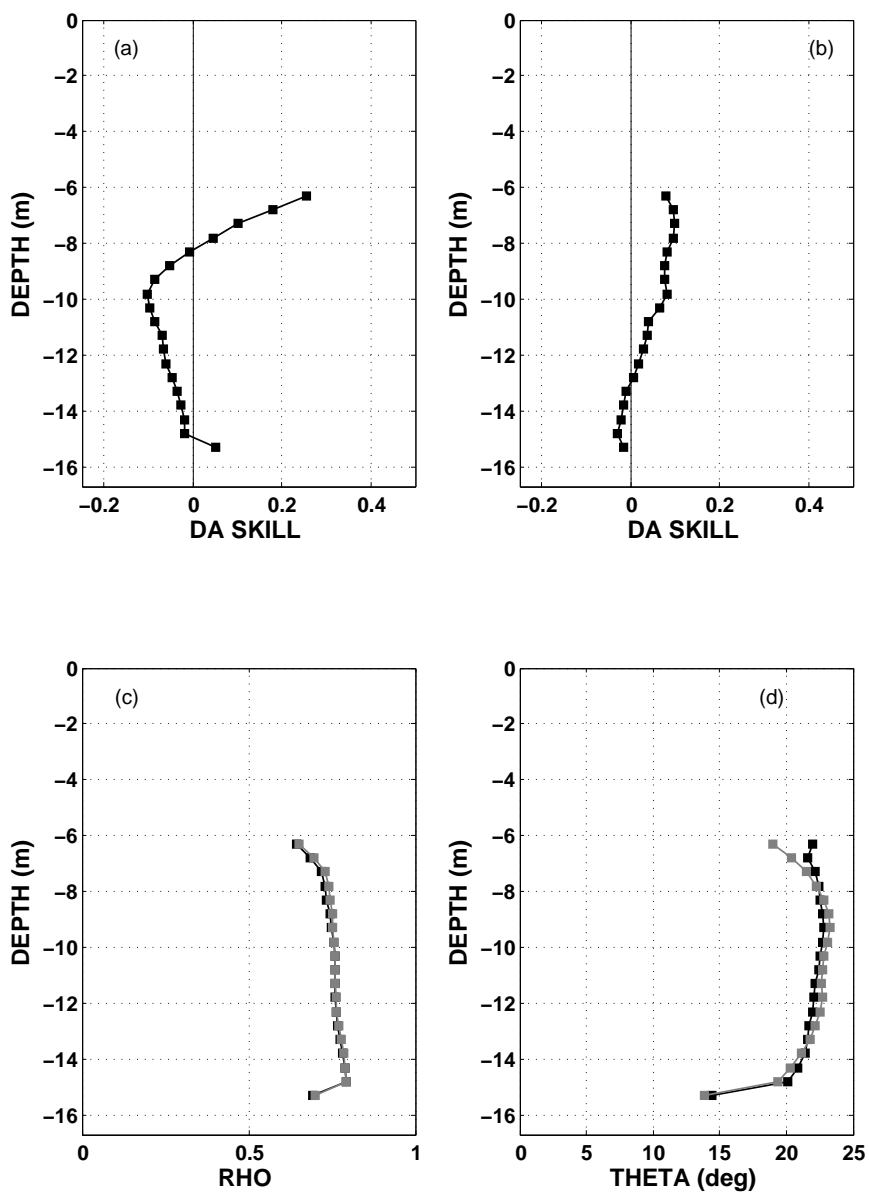
Figure: 9.4. **Data assimilation skill (black square) with respect to M3 data for the**

u (a) and v (b) component, and complex correlation [complex

correlation magnitude ρ (c), and complex correlation phase θ (d)]

between non-assimilated model and M3 data (black square) and

assimilated model and M3 data (gray square).
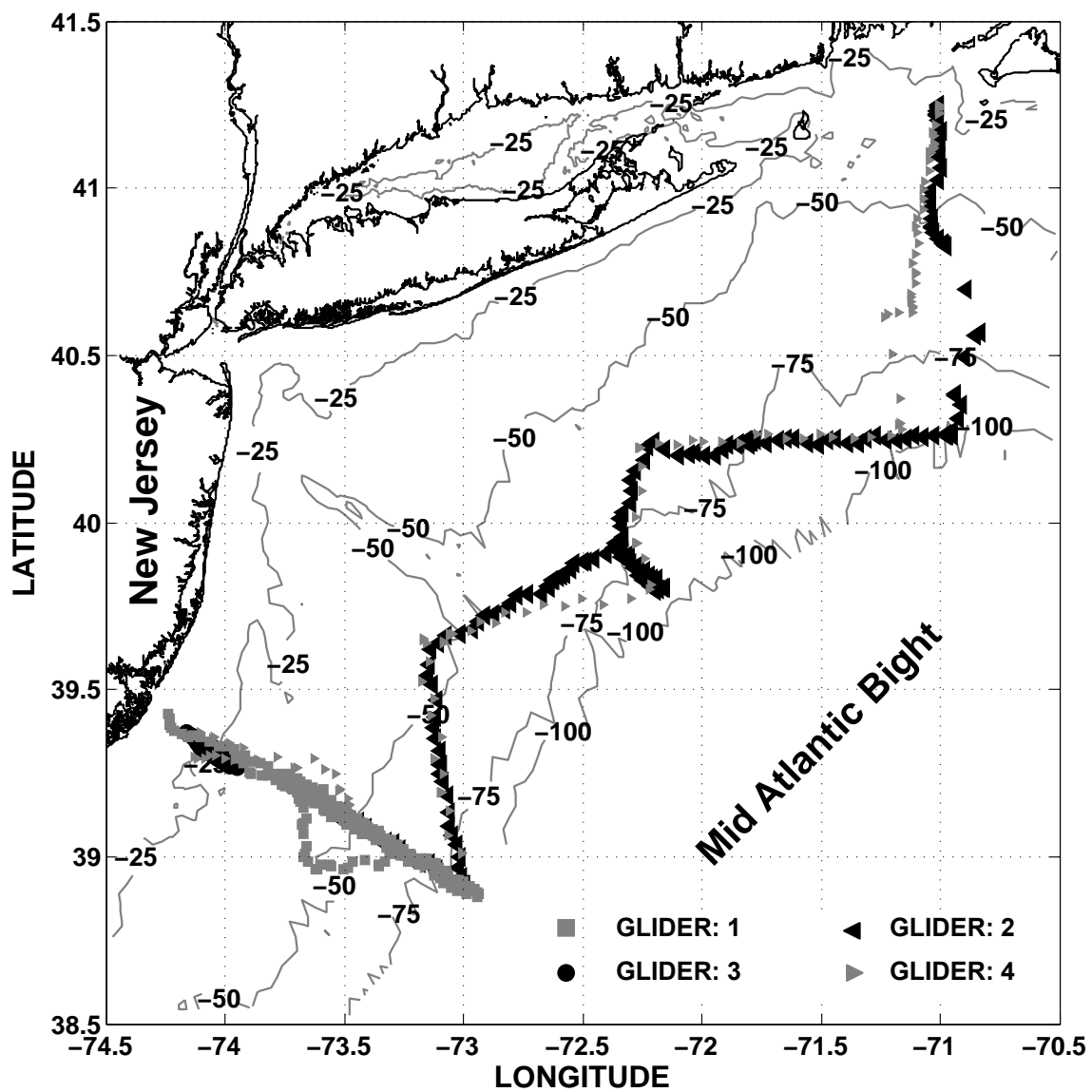
Figure: 9.5. Glider flight trajectory along with bathymetric contours (in meters) and NJ coastline.

coastal ocean; to the Nantucket Islands, MA. The improvement in the model performance with respect to three-dimensional T and S fields by DA studied by computing the *DA skill* based on mean square error *(mse)* between assimilated model T and S profiles and Glider T and S profiles *(MSE$_A$)*, and non-assimilated model T and S profiles and Glider T and S profiles *(MSE$_F$)*. The Glider T and S profiles were hourly averaged over time and vertically averaged over depth at every meter from the surface. The NYHOPS model T and S profiles were hourly averaged and vertically interpolated over depth at every meter from the surface similar to Glider T and S profiles. The *DA skill* (see Chapter 8, Equation 8.6, Page 128) for T and S is computed as a function of the depth for the regions of inner-NJ shelf *(0-30 m)* and mid-NJ shelf *(30-90 m)* for the whole period of Glider flight. The *DA skill* for the T and S for the inner-shelf region with respect to Glider: 1 and Glider: 3 are shown in Figure: 9.6. In the inner-NJ shelf region, DA shows considerable improvement in forecasting T and S throughout the water column [*DA skill* (T): +10%, *DA skill* (S): +16%]. The *DA skill* for the T and S for the mid-NJ shelf region with respect to Glider: 4 and Glider: 2 are shown in Figure: 9.7. In the mid-NJ shelf region, DA represents no significant enhancement in the model performance for both S and T.

9.3.3 Data Assimilation Skill Based on Fixed Sensor Temperature and Salinity Observations

The assimilated and non–assimilated model simulations for T and S were compared with fixed sensor *in-situ* T and S observations obtained from NDBC stations,
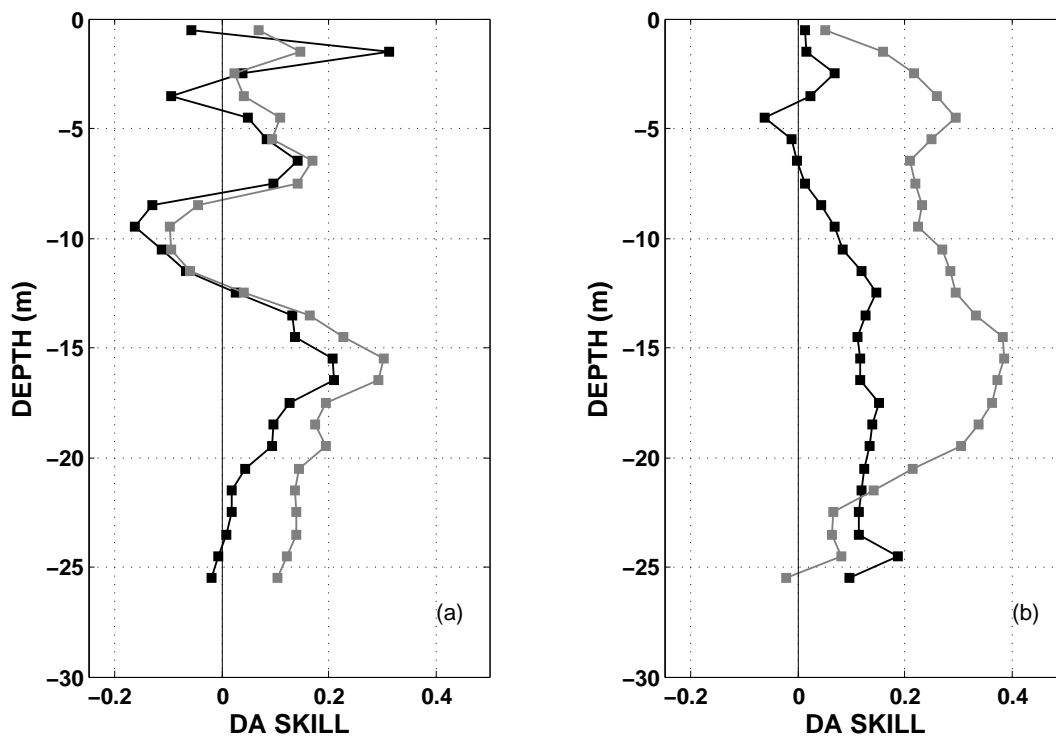
Figure: 9.6.   Data assimilation skill at the inner-NJ shelf region with respect to Glider: 1 data (a) and Glider: 3 data (b). (Black square represents salinity and gray square represents temperature).
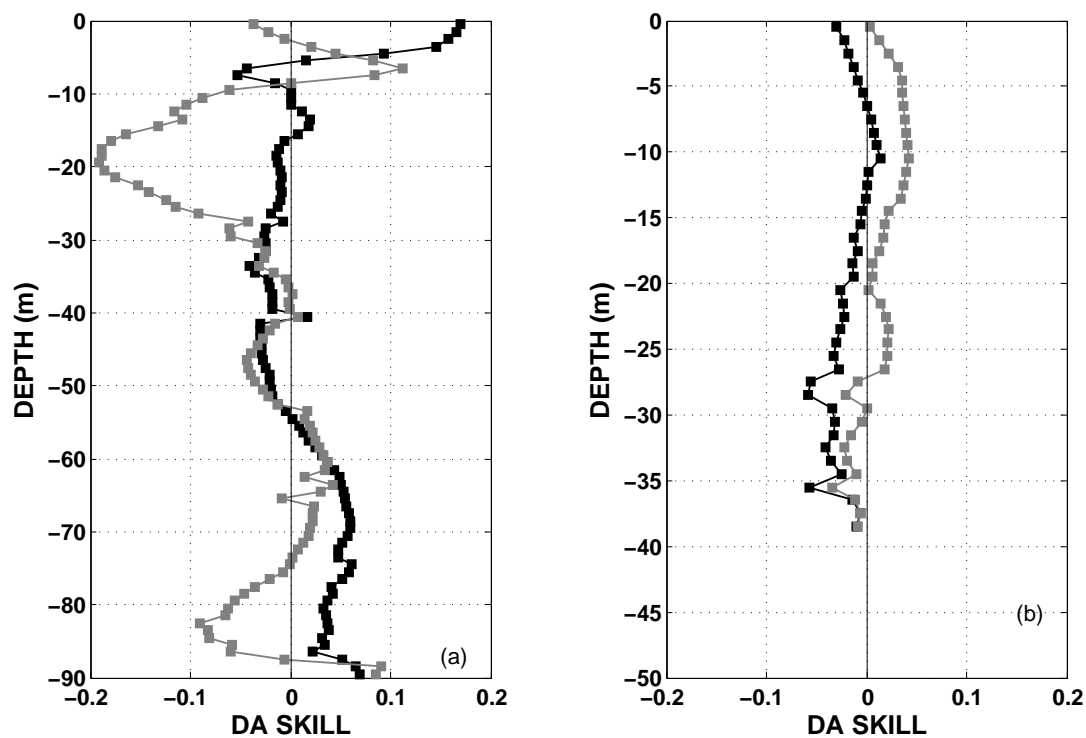
Figure: 9.7.   Data assimilation skill at the mid-NJ shelf region with respect to Glider: 4 data (a) and Glider: 2 data (b). (Black square represents salinity and gray square represents temperature).

NOS stations, USGS stations, and SIT stations. The computed *DA skill* with respect to T and S observations were tabulated and shown in Table: 9.2. The comparisons between assimilated and non-assimilated model T simulations with *in-situ* T observations are shown in Figure: 9.8. (BATN6, ALSN6, 44009). The assimilated model simulations show a better comparison with *in–situ* observations than non-assimilated model, representing an improvement in the model performance by DA. The comparisons between assimilated and non-assimilated model simulations with *in-situ* S observations are shown in Figure: 9.9. (STGWBR4 and STPR404). This figure also shows a better comparison between assimilated model simulations and *in–situ* observations than non-assimilated model, representing an improvement in the model performance by DA.

9.4   Analysis of the NYHOPS Model Performance During Flooding Event

The HF radar DA experiment in the NYB domain for the period of 120 days (March 2nd - June 29th, 2007) focused on the extreme weather event of coastal flooding along the NJ coast on April 15th – 16th, 2007 (Tax Day flooding event). The effectiveness of the HF radar DA in enhancing the forecasting capability of the NYHOPS model is analyzed for the period of Tax Day flooding event (April 14th – 23rd, 2007). The *DA skill* for the flooding event, based on mean square error, is computed with respect to fixed sensor *in-situ* T and S observations.

Table: 9.2.   Data assimilation skill (Forecast) of the NYHOPS model

(Comparison with fixed sensor *in-situ* observations).

Location	Station Name	Agency	Parameter	Depth	DA skill
The Battery, NY	BATN6	NOS	Temperature	Surface	+14%
Ambrose Light, NY	ALSN6	NDBC	Temperature	Surface	+16%
Delaware Bay, NJ	44009	NDBC	Temperature	Surface	+22%
Belford, NJ	STBLD4	SIT	Temperature	Bottom	+15%
George Washington Bridge, NJ	STGWBR4	SIT	Temperature	Surface	+6%
Pier 40, NY	STPR404	SIT	Temperature	Surface	+23%
Avalon, NJ	AVAN4	NDBC	Temperature	Surface	+6%
Reynolds Channel at Point Lookout, NY	U206	USGS	Temperature	Surface	+5%
George Washington Bridge, NJ	STGWBR4	SIT	Salinity	Surface	+7%
Pier 40, NY	STPR404	SIT	Salinity	Surface	+6%
Reynolds Channel at Point Lookout, NY	U206	USGS	Salinity	Surface	+17%
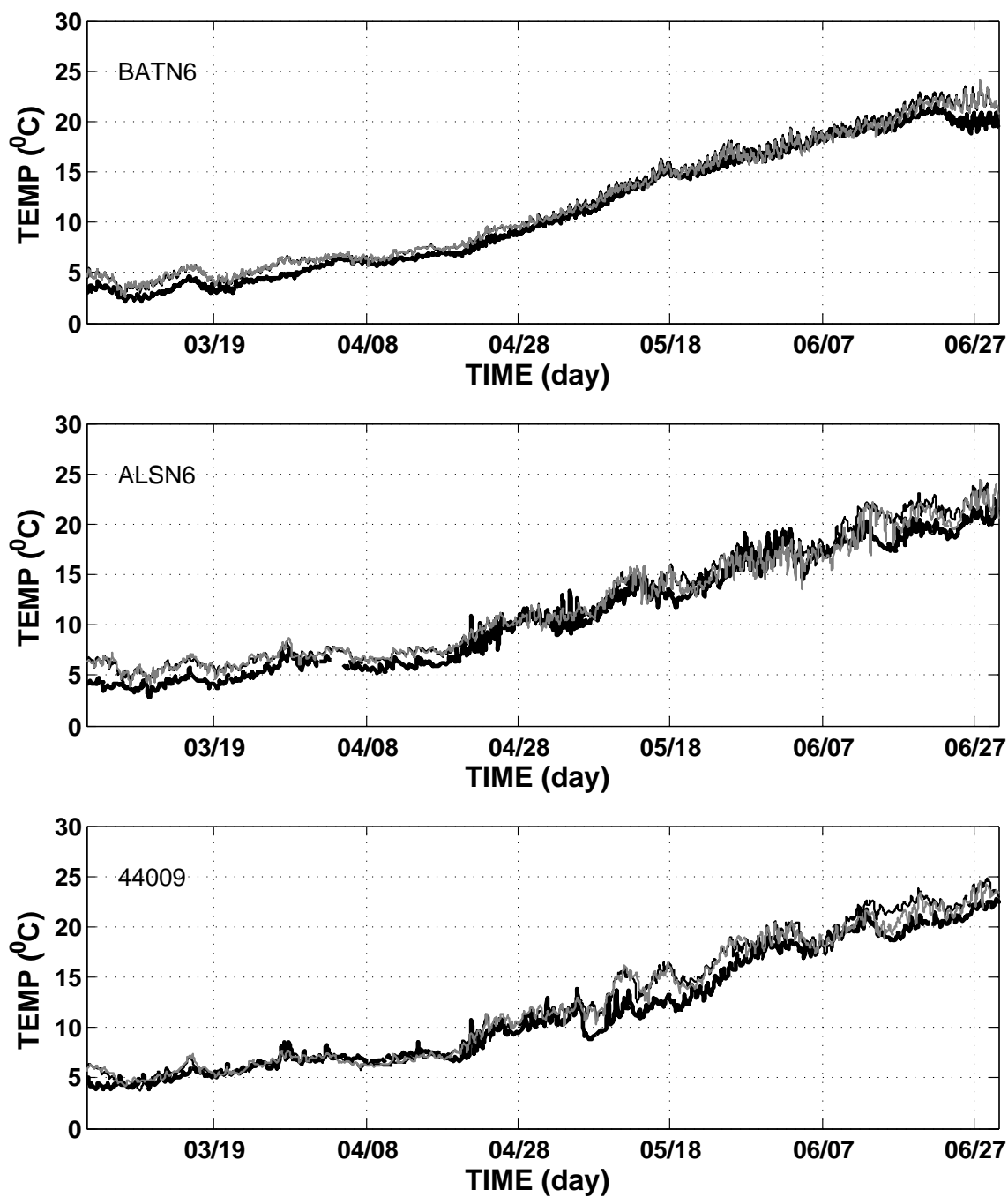
Figure: 9.8. Time-series comparison for temperature obtained from assimilated model (gray line), non-assimilated model (thin black line), and *in-situ* observation (thick black line). Figure legend represents the stations.
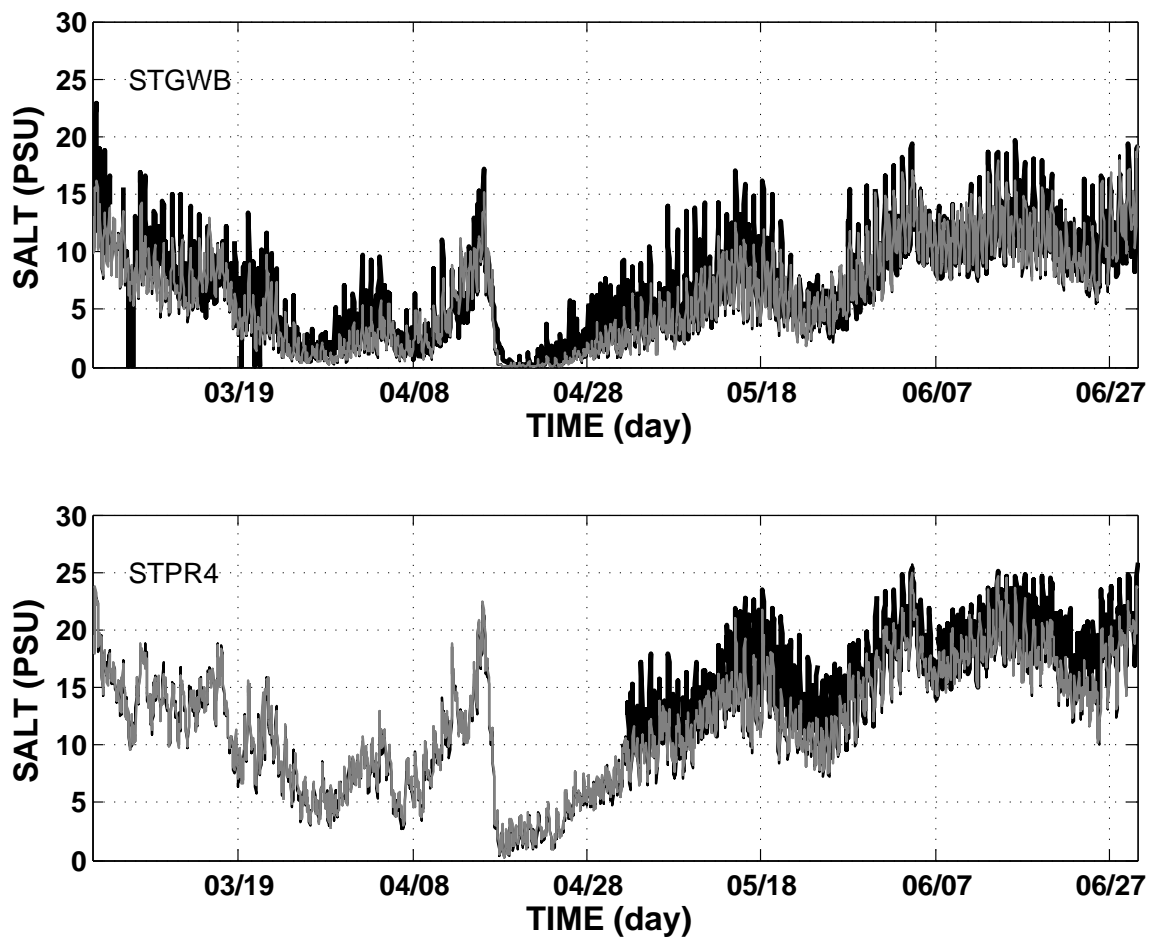
Figure: 9.9. **Time-series comparison for salinity obtained from assimilated model (gray line), non-assimilated model (thin black line), and *in-situ* observation (thick black line). Figure legend represents the stations.**

The Hudson River discharge for the month of April 2007 measured by USGS station (#01335754) at Federal dam, Troy, NY; is shown in Figure: 9.10a. The discharge during the flooding event (shaded region) peaks up to 35,000 ft^3 s^{-1} (991 m^3 s^{-1}). The water level for the month of April 2007 measured by the NOS station (Atlantic City, NJ: ACNY4) is shown in Figure: 9.10b. This plot shows the flooding event (shaded region) with water levels greater than 1.0 m. The atmospheric pressure variations and surface wind data for the flooding event (April 14th – 23rd, 2007) obtained from the NDBC station (Ambrose Light, NY: ALSN6) are shown in Figures: 9.10c and 9.10d. The atmospheric pressure drops from 1020 mb to 970 mb on April 16th and a reversal of wind stress is experienced. Northerly wind with a magnitude greater than 10 m s^{-1} was observed during April 17th – 19th. This strong northerly winds may trigger a net shoreward Ekman transport. The increased Hudson River outflow and the strong northerly winds during April 14th – 23rd, 2007 resulted in coastal flooding and downwelling processes along the NJ coast.

9.4.1 Results and Discussion

The assimilated and non–assimilated model forecast simulations were compared with fixed sensor *in-situ* T and S observations for the period of flooding event (April 14th – 23rd, 2007). The computed *DA skill* with respect to *in-situ* T and S observations for the flooding event were tabulated and shown in Table: 9.3. The comparisons between assimilated and non-assimilated model with *in-situ* T and S observations
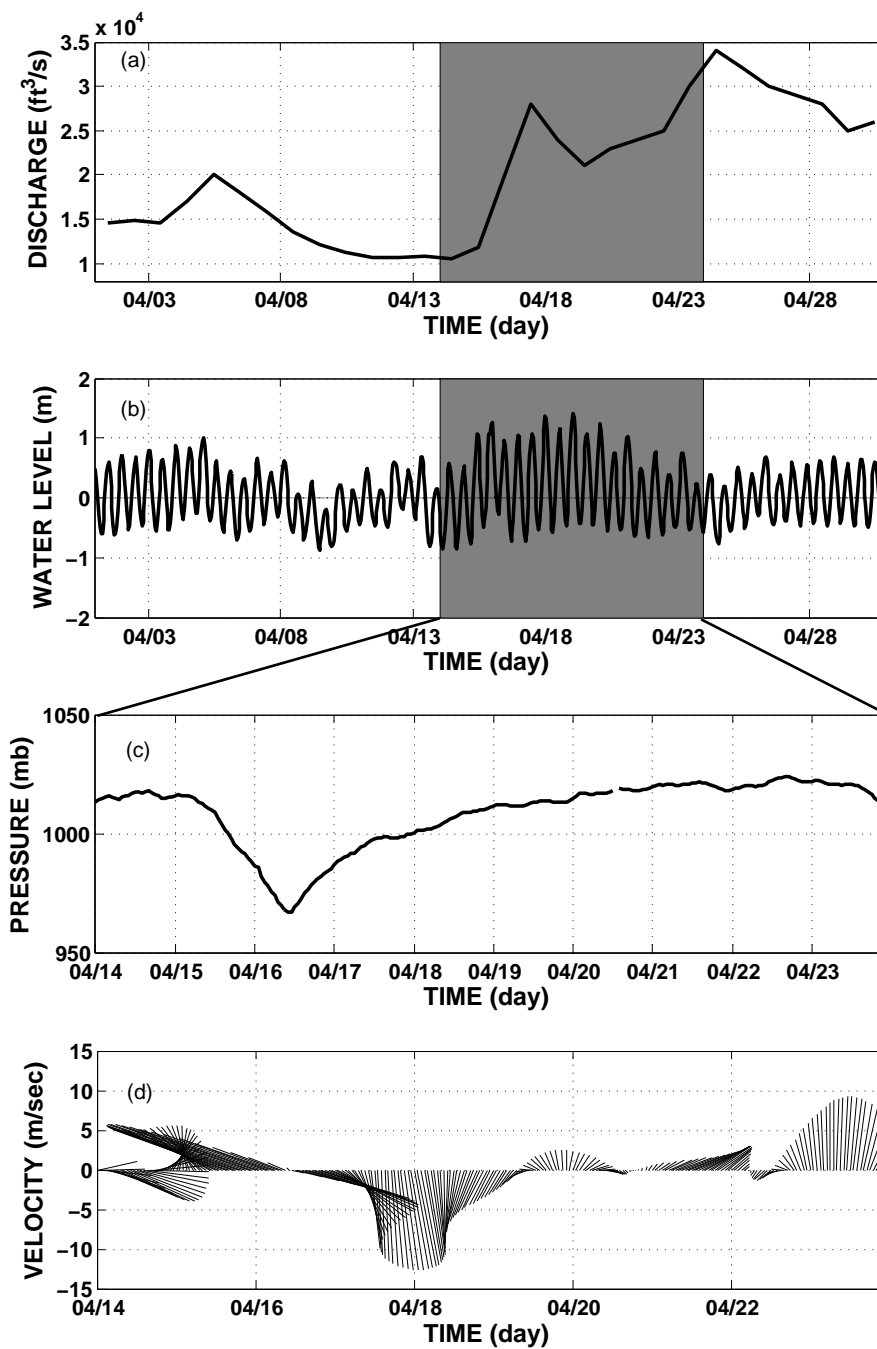
Figure: 9.10. Time-series for Hudson River discharge (a), water level at Atlantic City, NJ (b), atmospheric pressure at Ambrose Light, NY (c), wind velocity (d) (34 hour low-pass filtered) at Ambrose Light, NY.

Table: 9.3. **Data assimilation skill (Forecast) of the NYHOPS model**

(Comparison with fixed sensor *in-situ* observations for the Tax day

flooding event: April 14th – 23rd, 2007).

Location	Station Name	Agency	Parameter	Depth	DA skill
Montauk Point, NY	*44017*	*NOS*	*Temperature*	*Surface*	*+11%*
Delaware Bay, NJ	*44009*	*NDBC*	*Temperature*	*Surface*	*+26%*
George Washington Bridge, NJ	*STGWBR4*	*SIT*	*Salinity*	*Surface*	*+7%*

(44017, 44009, STGWBR4) are shown in Figure: 9.11. The assimilated model shows a better comparison with *in–situ* T and S observations than the non-assimilated model, representing an improvement in the model performance by DA.

The non-assimilated and assimilated model forecast simulations for the three-dimensional currents, salinity, and temperature were averaged for a ten day period during the flooding event (April 14th – 23rd, 2007). The ten day mean surface flow field for the non-assimilated model and the modifications due to DA (non-assimilated model – assimilated model) for the NYB Apex is shown in Figure: 9.12. The non-assimilated model shows a stronger outflow of ~ 0.5 m s^{-1} near the mouth of the NY/NJ Harbor Estuary. This stronger outflow due to the Hudson River plume follows a re-circulation pattern, resulting in a buoyant bulge formation near the mouth. The Hudson River plume bulge formation near the mouth of the NY/NJ Harbor Estuary was earlier reported by *Choi and Wilkin* [2007], *Chant el al.* [2008]. The northerly wind during the flooding event amplifies the coastal current and drains out the buoyant Hudson River plume bulge. The modified surface flow field (non-assimilated model – assimilated model) due to DA shows a magnitude difference greater than 5 cm s^{-1} in the NYB Apex region and inside Raritan Bay, and a cyclonic eddy is observed in Raritan Bay. The non-assimilated model shows a stronger coastal current in the inner-NJ shelf region and an offshore directed transport.

The ten day mean surface salinity and temperature distribution obtained from the non-assimilated model and modifications due to DA (non-assimilated model - assimilated model) for the flooding event is shown in Figure: 9.13. The mean surface
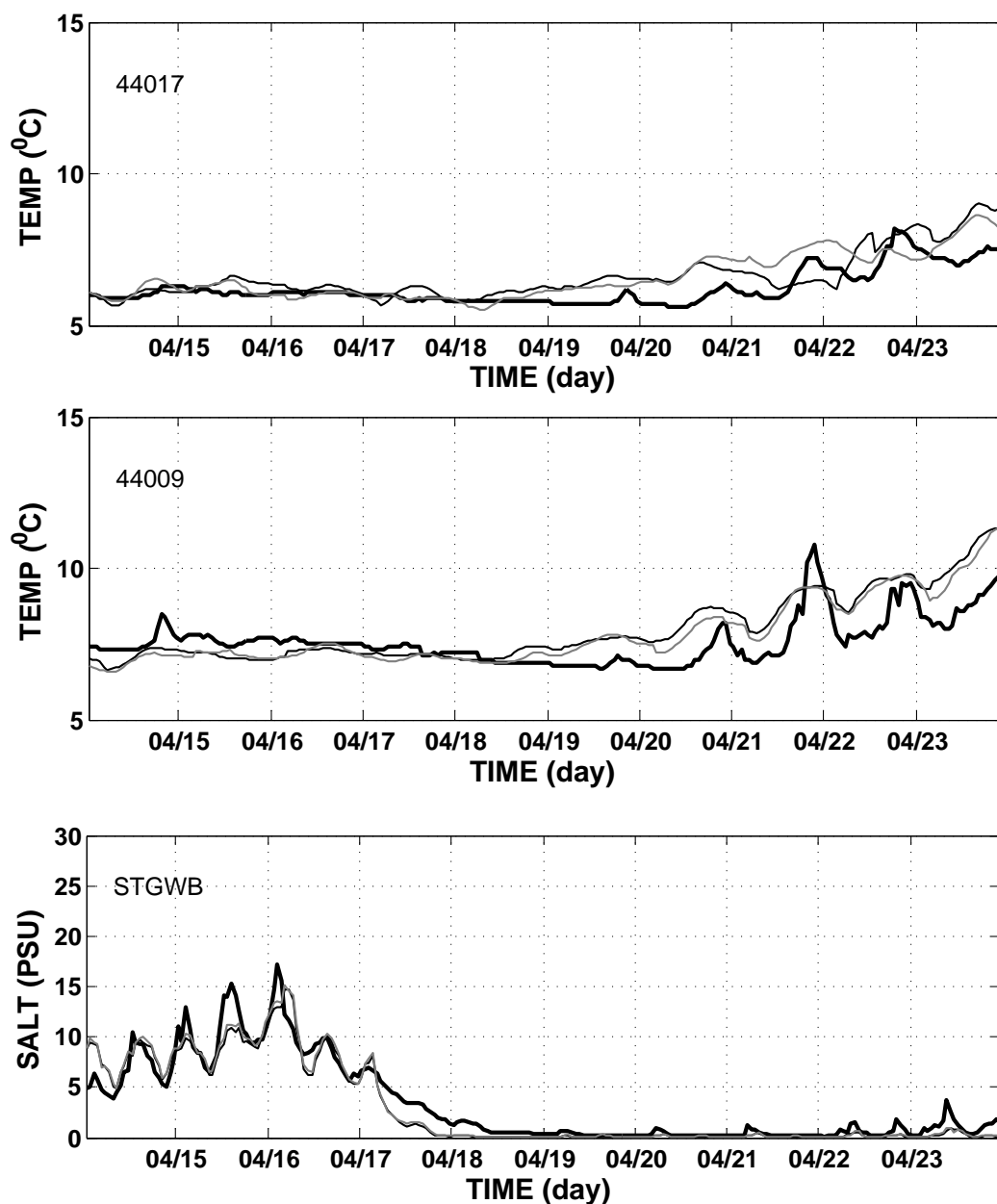
Figure: 9.11. Time-series comparison for temperature and salinity during the flooding event [assimilated model (gray line), non-assimilated model (thin black line), and *in-situ* observation (thick black line), Figure legend represents the stations].
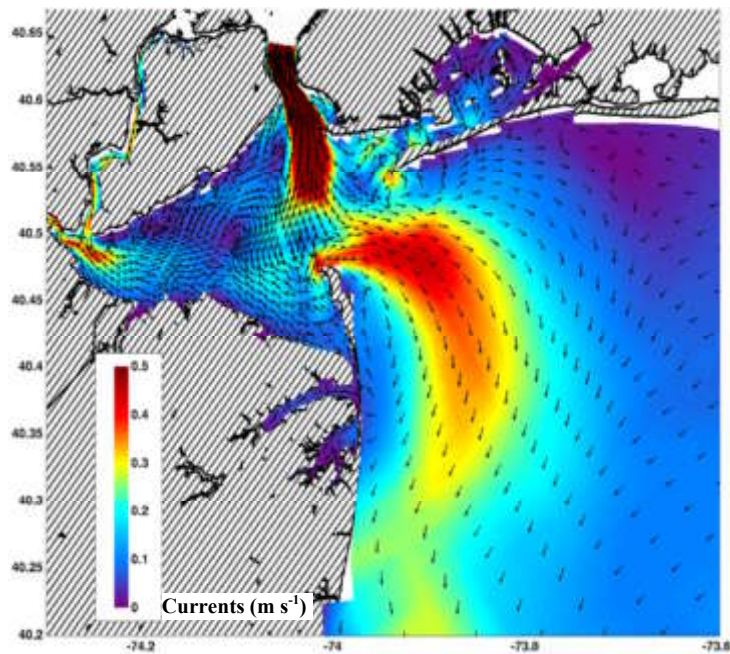
No Data Assimilation
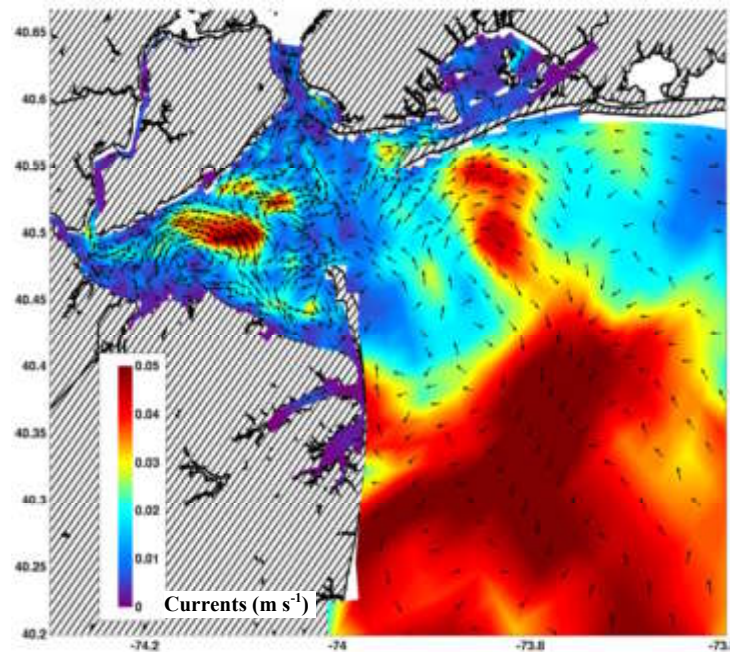
Modification (No DA - HF radar DA)

Figure: 9.12. Mean surface velocity (April 14th – 23rd, 2007) for the NYB Apex.

No Data Assimilation **Modification (No DA - HF radar DA)**
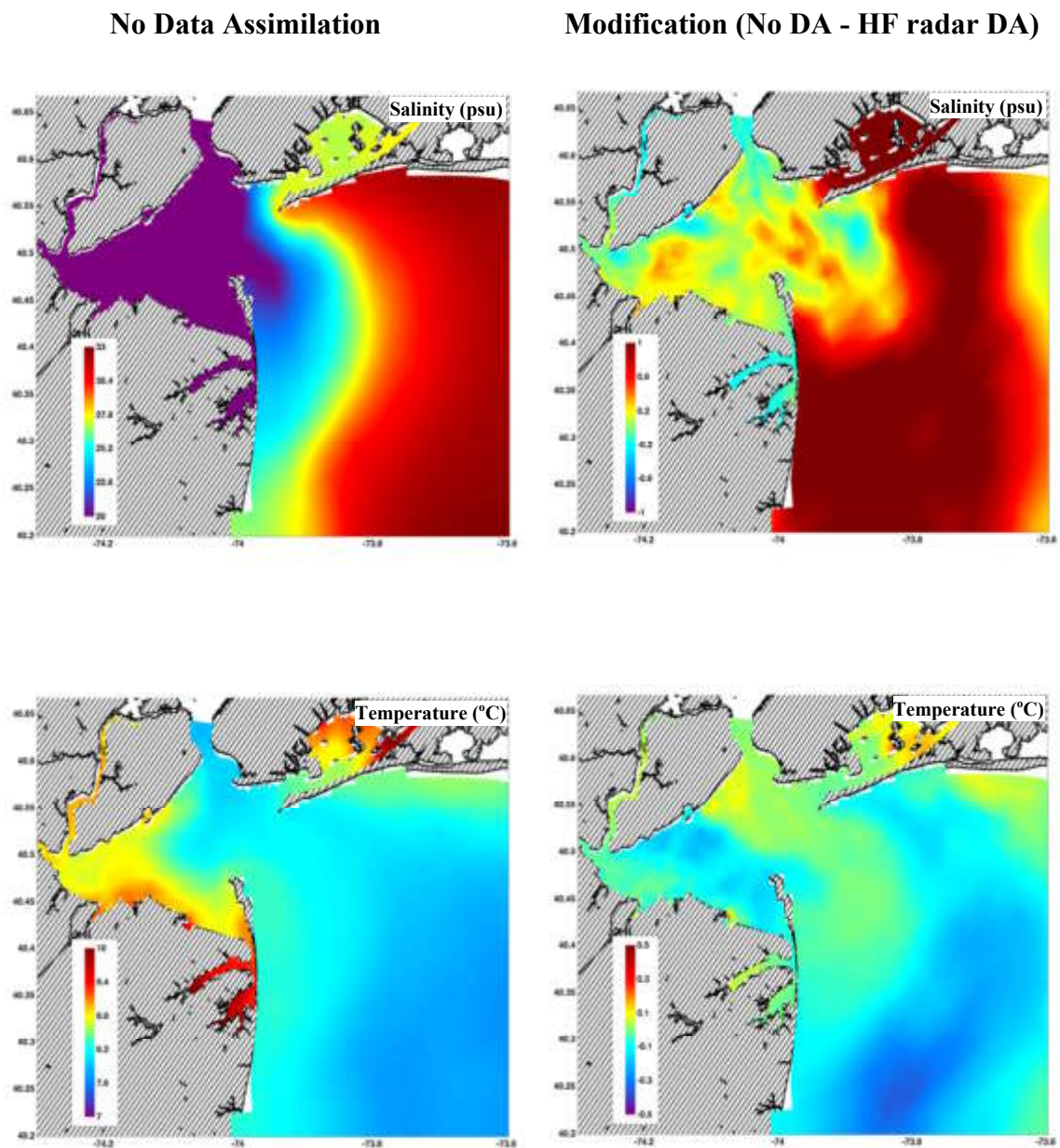
Figure: 9.13. Mean surface salinity (top) and temperature (bottom) for the

NYB Apex (April 14th – 23rd, 2007).

salinity distribution for the non-assimilated model represents the freshwater bulge formation near the mouth of the NY/NJ Harbor Estuary. The modified salinity distribution (non-assimilated model – assimilated model) shows a salinity difference of ~ +0.5 psu near the mouth and inside Raritan Bay, and a salinity difference greater than +1 psu in the NYB Apex region, representing fresher waters due to DA. In the case of non-assimilated model, the stronger surface re-circulation increases the across-shelf mixing processes between buoyant freshwater and saltier sea water. HF radar DA decreases the re-circulation and across-shelf mixing processes near the mouth of the NY/NJ Harbor Estuary and allows surface spreading of buoyant freshwater across the shelf and along the NJ coast. This results in fresher near-surface waters south of the Sandy Hook coast compared to non-assimilated model. The mean surface temperature distribution for the modified field (non-assimilated model – assimilated model) shows a temperature difference of ~ -0.3 ^{0}C in the NYB Apex region and Raritan Bay, representing warmer waters due to DA. The weaker surface flow field near the mouth of the NY/NJ Harbor Estuary due to HF radar DA decreases the across-shelf coastal mixing processes and allows the freshwater pathway of warmer Hudson River outflow into Raritan Bay and along the NJ coast. The presence of warmer waters along the NJ coast and its dependency on the Hudson River plume has been reported by *Kohut el al.* [2005] based on the Lagrangian Transport and Transformation Experiment (LaTTE), April 2005.

The ten day mean across-shelf sectional currents, salinity, and temperature for the non-assimilated model and the modifications due to DA (non-assimilated model – assimilated model) for a section off of Sea Girt, NJ; are shown in Figure: 9.14. The

across-shelf sectional flow field for the non-assimilated model shows a strong, near-surface, southward directed coastal current of ~ 15 cm s^{-1} and an offshore directed across-shelf current greater than 5 cm s^{-1} in the inner-NJ shelf region. The modified across-shelf sectional flow field shows a difference of ~ -5 cm s^{-1} in the southward directed coastal current and an along-shelf current difference of ~ +1 cm s^{-1} in the mid-NJ shelf region. The modified across-shelf current remains the same as that of the non-assimilated model except in the inner-NJ shelf and outer-NJ shelf regions. The modified across-shelf salinity distribution shows a salinity difference of ~ +0.5 psu in the inner-NJ shelf region, representing fresher near-surface waters due to DA. The modified across-shelf temperature distribution shows a temperature difference of ~ -0.2 ^{0}C in the inner-NJ shelf region, representing warmer near-surface layers, and a near-bottom temperature difference of ~ 0.3 ^{0}C in the mid-NJ shelf region representing cooler waters due to DA. The effect of warmer and fresher Hudson River plume with respect to across-shelf temperature and salinity distribution is more predominant in the assimilated model than non-assimilated model.

The ten day mean along-shelf sectional currents, salinity, and temperature for the non-assimilated model and the modifications due to DA (non-assimilated model – assimilated model) between Cape May, NJ; and Sea Girt, NJ; are shown in Figure: 9.15. The modified along-shelf sectional flow field shows no significant differences in the along-shore and across-shore velocities except near Sea Girt, NJ, where a velocity difference of ~ -5 cm s^{-1} in observed in both along-shelf and across-shelf direction. The

No Data Assimilation   **Modification (No DA - HF radar DA)**
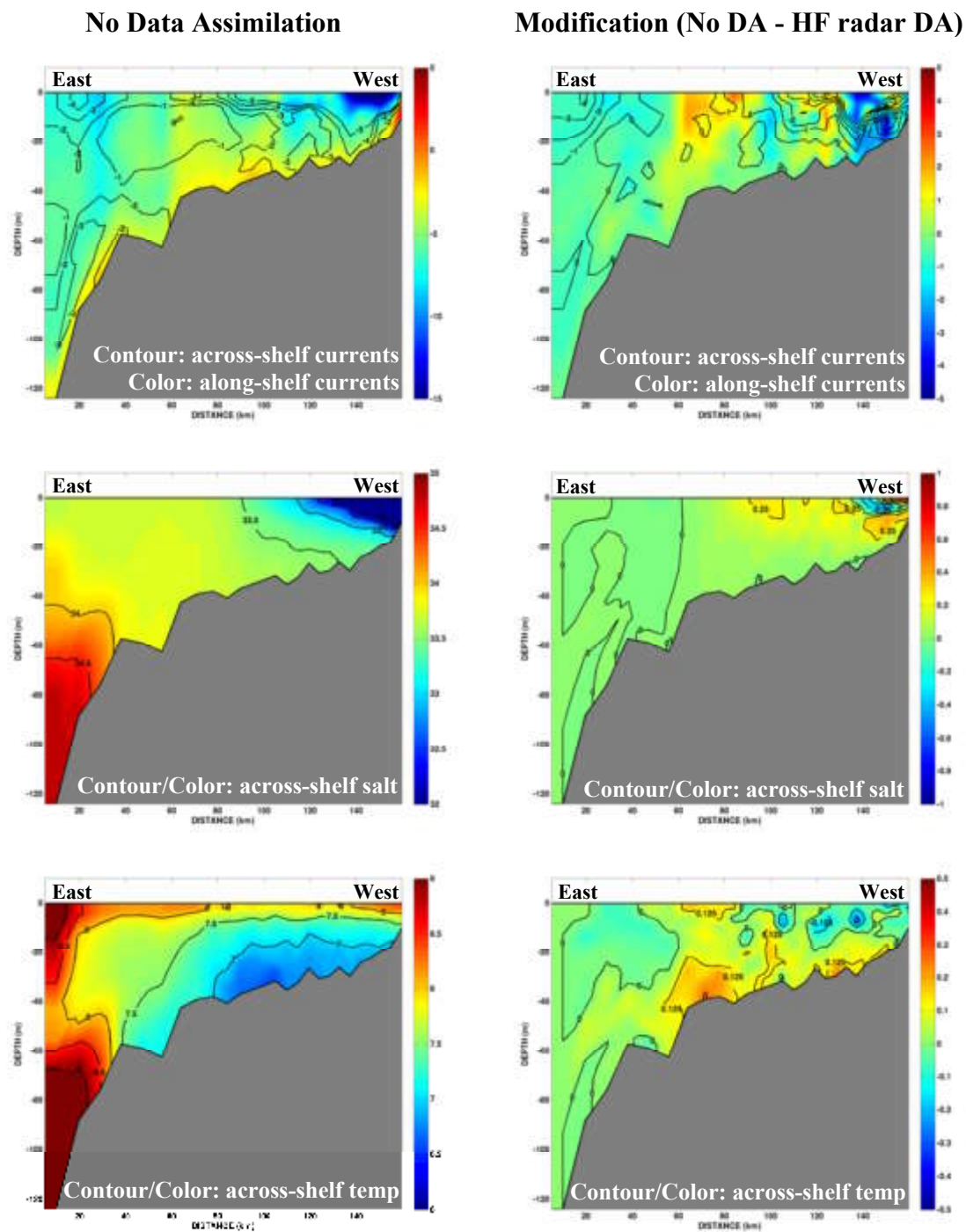
Figure: 9.14. **Mean across-shelf currents in cm s^{-1} (top), salinity in psu (middle),**

and temperature in degree Celsius (bottom) off Sea Girt, NJ (April

14th – 23rd, 2007).

No Data Assimilation **Modification (No DA - HF radar DA)**
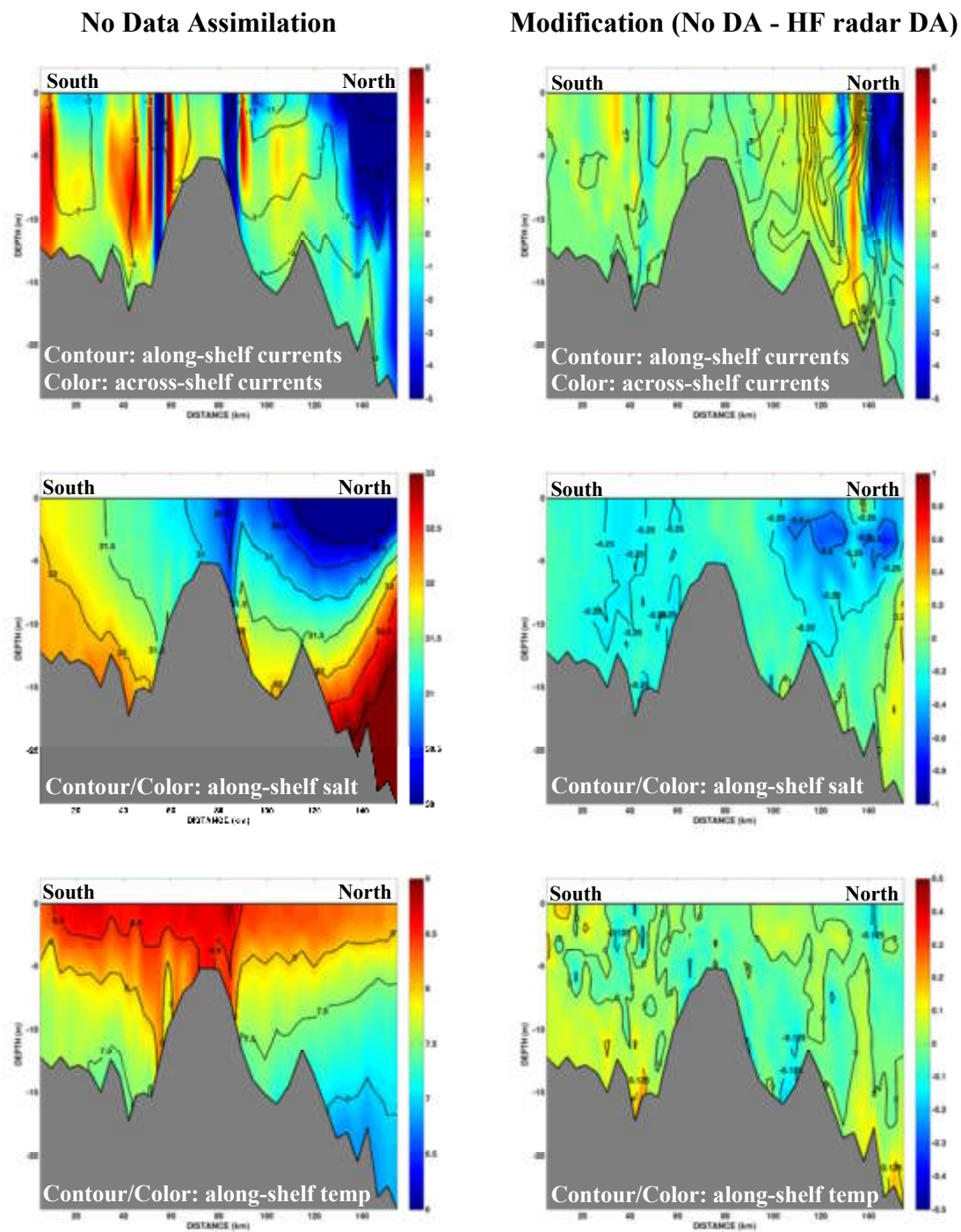
Figure: 9.15. Mean along-shelf currents in cm s^{-1} (top), salinity in psu (middle), and temperature in degree Celsius (bottom) from Cape May, NJ to Sea Girt, NJ (April 14th – 23rd, 2007).

modified along-shelf salinity distribution shows a salinity difference of ~ -0.5 psu near Sea Girt, NJ; representing saltier waters due to DA. The modified along-shelf temperature distribution shows no significant differences due to HF radar DA.

9.5   Conclusions

Long-range HF radar data obtained in the NYB domain were assimilated into the NYHOPS model for a period of 120 days (March 2nd - June 29th, 2007) using a nudging scheme. The effectiveness of DA in enhancing the model forecasting capabilities (1st day model forecast, daily model simulations from 0 hours to 24 hours) is studied by computing the *DA skill*. The *DA skill* is based on mean square error between assimilated/non-assimilated model results and three–dimensional currents obtained from three moorings, three–dimensional T and S fields obtained from four Slocum Gliders, and fixed sensor *in-situ* T observations at eight locations and S observations at three locations. A positive *DA skill* (0 – 100%) represents an improvement in the model performance by HF radar DA. The model forecasting capabilities with and without HF radar DA for the period of extreme weather event (Tax day flooding event: April 15th – 16th, 2007) is also studied.

The DA improved the model forecasting performance based on the *DA skill* measures with respect to M2 and M3 mooring data. A *DA skill* of +6% and +14% for *u* and *v* component was achieved with respect to M2 data for the near-surface layers, and a *DA skill* of +26% and +10% for *u* and *v* component was achieved with respect to M3 data

at a depth of 6.0 m from the surface. The *DA skill* values with respect to M1 data showed only a marginal improvement in the model performance by DA. The *DA skill* for the NYHOPS model forecasts with respect to the three moorings (M1, M2, and M3) for this long-range HF radar DA experiment followed a similar trend to that of the *DA skill* for the NYHOPS model hindcasts for the standard-range HF radar DA experiment (see Chapter 8).

The modifications to three-dimensional T and S fields due to DA were studied by comparing assimilated and non-assimilated model T and S simulations with T and S fields obtained from four Slocum Gliders with Glider flights across and along the NJ shelf. The *DA skill*, based on mean square error, is computed for T and S with respect to inner-NJ shelf and mid-NJ shelf regions as a function of water depth. The DA improved model forecasts T and S for the near-surface layers with respect to inner-NJ shelf region [*DA skill* (T): +10%, *DA skill* (S): +16%], while the *DA skill* values show no improvement in the model performance with respect to mid-NJ shelf region. The low *DA skill* values in the mid-NJ shelf regions can be associated with the model boundary conditions along the open ocean boundary at the mid-shelf, and also due to the influence of offshore climatology.

The *DA skill* is also computed with respect to fixed sensor *in-situ* T observations at eight locations and S observations at three locations. The DA showed improvement in forecasting sea-surface T (*DA skill* of +22% at 44009 station) and salinity (*DA skill* of +7% at STGWBR4 station).

The performance of the model with and without HF radar DA for the period of tax day flooding (April 14th – 23rd, 2007) event was analyzed. The assimilated and non-assimilated model T simulations were compared with fixed sensor *in-situ* T and S observations along the NY/NJ coast for the flooding period. The comparison yielded improvement in the model forecast by DA (*DA skill* of +26% at 44009 station). The ten day mean (April 14th – 23rd, 2007) surface currents, temperature, and salinity fields for the assimilated model during the flooding period showed a dominant influence of warmer and fresher Hudson River outflow in Raritan Bay, mouth of the NY/NJ Harbor Estuary, and along the NJ coast than non-assimilated model. The NYHOPS model is capable of simulating the buoyant Hudson River plume and the bulge formation near the mouth during high river discharge event. The nudging of HF radar surface currents results in a weaker flow field near the mouth of the NY/NJ Harbor Estuary and an increased effect of warmer and fresher Hudson River outflow in Raritan Bay, mouth of the NY/NJ Harbor Estuary, and along the NJ coast.

Chapter 10

Summary and Conclusions

The focus of this research work can be separated into two major categories; first, surface current measurement using HF radar and its validation and second, application of surface current data by assimilating it into the estuarine and coastal ocean circulation model for idealized model with long straight and curved channel, and the NYHOPS model. HF radar is a novel, land-based ocean measurement platform capable of measuring near-surface ocean currents in real-time. The continuous stream of surface current data measured using HF radar over a synoptic scale of $O(40$ km$)$ were assimilated into the NYHOPS model using a nudging scheme to improve the model performance in hindcasting as well as forecasting three-dimensional water parameters. The salient conclusions of the present work are presented in the following sections.

10.1   Sensitivity of CODAR First-Order Doppler Region Settings

The present research revealed the importance of the first-order (FO) Doppler region settings of CODAR in a tidally-dominated region of the NY/NJ Harbor Estuary (see Section 3.6 in Chapter 3). Empirical methods are used to identify the local minima

which define the FO Doppler region, from which the surface current information is derived. The FO settings are highly sensitive to the oceanographic circulation at a particular site. The occurrence of strong currents results in spreading of the FO Doppler region in the sea-echo, and a wider FO setting is required to capture these strong currents. Since the FO region settings remains the same for all CODAR range cells, CODAR fails to capture the strong currents which occurs only at a particular range cell surrounded by range cells representing weak currents.

In the present study, the total surface currents obtained by combining the radial currents measured by the four CODAR systems covering Raritan Bay and the NYB Apex, exhibits a peculiar pattern near the mouth of the NY/NJ Harbor Estuary. The CODAR surface currents near the mouth of the NY/NJ Harbor Estuary were directed along the SHRP transect rather than flowing normal to it. This unusual flow pattern of the CODAR currents at the SHRP transect are dominant during strong ebb tides. This peculiar CODAR current pattern can be due to the elimination of good data near the mouth of the NY/NJ Harbor Estuary, measured by the SILD site, owing to the spreading of the FO Doppler spectrum during strong ebb tidal currents. Earlier observational findings by *Oey et al.* [1985b] reported a strong tidal current of $O(1.0 \text{ m s}^{-1})$ at the SHRP transect and the Verazzano Narrows, oriented normal to the cross-section. The CODAR surface currents near the SHRP transect were found to be weaker than the earlier findings and oriented mostly along the SHRP transect. This suggests the need of a more precise FO Doppler region setting for the SILD and BSWP CODAR sites.

10.2   HF Radar Data Validation

The surface currents measured using HF radar was validated with respect to *in-situ* current measurements (see Chapter 4). The HF radar measured surface currents were statistically compared with near-surface current measurements obtained from two moorings (M1 and M2). The conclusions of the validation study are summarized below.

- HF radar surface currents showed an overall moderate correlation with M1 near-surface bin currents with a better correlation for the along-shore component v than the cross-shore component u.

- HF radar surface currents showed an overall good correlation with M2 near-surface bin currents with a better correlation for the predominant along-shore component u than the cross-shore component v.

- The cross-shore processes and the horizontal and vertical shear in the near-surface water column influences the validation results at the two locations (M1 and M2).

- The estimation of total vector field by combining radial vectors measured by different HF radar sites introduces inherent errors due to the geometric combination of the radials (GDOP, see Section 3.5, Chapter 3) which can possibly affect the validation results.

- HF radar total vectors are spatially averaged over an ocean surface patch of $O(1 \sim 4 \text{ km}^2)$ and near-surface depth averaged of $O(0.5 \text{ m})$, while mooring data represents a point measurement of subsurface currents and is averaged over the

depth of measurement bin of $O(0.5 \text{ m})$. This difference in the spatial averaging of the current measurement highly influences the validation results.

- The proximity of M1 and M2 location to the HF radar station (M1 falls within the first range cell of Sandy Hook site, M2 falls within second range cell of Breezy Point site) and the shallow water conditions influences the HF radar data quality at M1 and M2 location. The HF radar data in the first range cell were generally neglected owing to poor data quality. These factors contribute to the observed differences between HF radar data and mooring data.

- Since HF radar works on the basic assumptions of linear wave theory and deep water conditions, the influence of shallow water waves and wave-current interaction are not well resolved by the generic HF radar processing algorithm. An enhanced site specific HF radar (CODAR) processing algorithm based on shallow water conditions may improve the validation results.

10.3   Surface Current Data Assimilation: An Idealized Model Study

The nudging scheme to assimilate surface currents into an estuarine and coastal ocean circulation model was initially applied to an idealized model using a long straight and curved channel (see Chapter 7). The ocean model was forced with realistic estuarine conditions of river discharge, tide, and density stratification. The conclusions of the idealized case study are summarized below.

- The idealized model study revealed the three-dimensional modifications to current, temperature and salinity fields due to assimilation of surface currents.

- The effect of nudging is significant in the case of assimilation of observed surface currents with higher magnitude and oppositely directed with respect to model surface currents.

- The effect of nudging is moderate in the case of assimilation of observed surface currents with higher magnitude and directed in the direction of model surface currents.

- The effect of DA on the three-dimensional circulation and density stratification suggested the requirement of a quality check of the magnitude and direction of HF radar derived surface currents prior to the assimilation into the NYHOPS model.

10.4   HF Radar Data Assimilation Experiment in the New York Harbor Domain

Surface currents measured using standard-range HF radar network covering Raritan Bay and the NYB Apex were assimilated into the NYHOPS model for a period of 40 days (February 24th - April 4th, 2007) using a nudging scheme (see Chapter 8). This DA experiment focused on the hindcasting capability of the NYHOPS model. The effectiveness of DA in enhancing the model performance is evaluated by computing the *DA skill*. The *DA skill* is based on mean square error between assimilated/non-assimilated

model results and *in-situ* observations which are not used as part of the DA. A positive *DA skill* (0 − 100%) represents an improvement in the model performance by HF radar DA. The *DA skill* matrix is shown in Table: 10.1 (Page 193 − 194). The conclusions are summarized below.

- The DA improved the model hindcasts for three-dimensional currents based on the *DA skill* scores with respect to M2 mooring data (*u*: +27% and *v*: +16% at the near-surface layers) and M3 mooring data (*u*: +50% and *v*: +21% at a depth of 6.0 m from the surface). The *DA skill* scores with respect to M1 mooring data showed only a marginal improvement in the model performance by DA. This can be related to the moderate correlation of HF radar surface currents with M1 near-surface bin currents (see Chapter 4, Page 79) and also the proximity of M1 location to the shore.

- The comparison of assimilated and non-assimilated model surface currents with surface currents obtained from drifter represented a good correlation between the model and the data. The HF radar DA improved the model hindcasts for surface currents (*DA skill* of *u*: +6% and *v*: +1% at near-surface) with respect to drifter data which falls outside the assimilation domain. The improvement in the model performance shows the influence of HF radar DA beyond the assimilation domain.

- The HF radar DA improved the model hindcasts for three-dimensional temperature and salinity distributions based on the *DA skill* with respect to Slocum Glider temperature and salinity data for the inner-NJ shelf region [*DA*

skill (T): +53%, *DA skill* (S): +38% at the near-surface layers]. The *DA skill* values for the mid-NJ shelf region showed no improvement in the model performance which can be related to model open ocean boundary conditions at the mid-NJ shelf region and the offshore climatology. The Glider flights falls outside the assimilation domain and the improvement in model performance suggests the influence of HF radar DA beyond the assimilation domain.

- The *DA skill* with respect to fixed sensor *in-situ* temperature observations at six locations showed pronounced improvement in hindcasting sea-surface temperature (*DA skill* of +34% at SDHN4 station).

10.5 HF Radar Data Assimilation Experiment in the New York Bight Domain

Long-range HF radar data obtained in the NYB domain were assimilated into the NYHOPS model for a period of 120 days (March 2nd - June 29th, 2007) using a nudging scheme. The effectiveness of DA in enhancing the model forecasting capabilities is studied by computing the *DA skill*. The *DA skill* is based on mean square error between assimilated/non-assimilated model results and *in-situ* observations which are not used as part of the DA. A positive *DA skill* (0 – 100%) represents an improvement in the model performance by HF radar DA. The long-range HF radar DA experiment also focused on the forecasting capabilities of assimilated and non-assimilated model for the extreme

weather event (Tax day flooding event: April 15th – 16th, 2007). The *DA skill* matrix is shown in Table: 10.1 (Page 193 – 194). The conclusions are summarized below.

- The HF radar DA improved the model forecasting performance based on the *DA skill* scores with respect to M2 mooring data (u: +6% and v: +14% at the near-surface layers) and M3 mooring data (u: +26% and v: +10% at a depth of 6.0 m from the surface).The *DA skill* for the NYHOPS forecasts with respect to the three moorings (M1, M2, and M3) for this long-range HF radar DA experiment followed a similar trend to that of *DA skill* for the NYHOPS hindcasts for the standard-range HF radar DA experiment (see Chapter 8). The proximity to the land boundary and the poor HF radar data quality at M1 location influences the assimilated model performance at the M1 location.

- The HF radar DA improved the model forecasts for three-dimensional temperature and salinity distribution based on *DA skill* with respect to Slocum Glider data [*DA skill* (T): +10%, *DA skill* (S): +16% at the near-surface layers] The *DA skill* values showed no improvement in model performance with respect to mid-NJ shelf region which can be associated with open ocean model boundary conditions and offshore climatology.

- The *DA skill* with respect to fixed sensor *in-situ* temperature observations at eight locations and salinity observations at three locations showed improvement in forecasting sea-surface temperature (*DA skill* of +22% at 44009 station) and salinity (*DA skill* of +7% at STGWBR4 station).

- The performance of the model with and without HF radar DA for the period of tax day flooding (April 15th – 16th, 2007) event was analyzed. The *DA skill* with respect to fixed sensor *in-situ* T and S observations showed improvement in the model forecast by DA (*DA skill* of +26% at 44009 station) for the flooding period.

- The ten day mean surface currents, temperature, and salinity fields of the assimilated model during the flooding period (April 15th – 16th, 2007) showed a dominant influence of warmer and fresher Hudson River outflow in Raritan Bay, mouth of the NY/NJ Harbor Estuary, and along the NJ coast than non-assimilated model. The model is capable of simulating the buoyant Hudson River plume and the bulge formation near the mouth. The nudging of HF radar surface currents results in a weaker flow field near the mouth and along the NJ coast and an increased effect of Hudson River outflow in Raritan Bay, mouth of the NY/NJ Harbor Estuary, and along the NJ coast.

10.6   Future Research

Future research in the areas of HF radar and advanced data assimilation techniques will be important in understanding the immense capabilities of HF radar system in the field of ocean measurements and application of ocean observations by assimilating ocean data into the numerical models providing an improved understanding of the ocean dynamics. Some areas of future work are listed below.

- Investigate the data quality and performance of CODAR in a tidally-dominated region of the NY/NJ Harbor Estuary incorporating more precise CODAR FO region settings.

- Perform a CODAR data validation experiment in Raritan Bay and SHRP transect using ADCP deployments at selected locations and vessel mounted ADCP transect studies.

- Assimilate sea surface temperature (SST) data from satellite, temperature and salinity data obtained from Slocum Gliders, and elevation data from NOS/NDBC sensors into the NYHOPS model along with HF radar surface current assimilation.

- Test advanced data assimilation techniques such as Ensemble Kalman filter or 4D variational method in NYHOPS model using ocean observations of currents, temperature, salinity, and elevation data.

- NYHOPS model coupling with atmospheric models, particle trajectory models, sediment transport model, chemical and biological model, and acoustic models. NYHOPS model hydrodynamics can be used as the driving source.

Table: 10.1. Data assimilation skill (*DA skill*) matrix (Hindcast and Forecast experiments).

Velocity (Moorings/drifter)												
Location			*Near-shore of Sandy Hook*			*Near-shore of Breezy Point*			*Offshore of Breezy Point*			*Mid NJ shelf*
Station Name			*M1*			*M2*			*M3*			*#43484*
Agency			*RU*			*RU*			*RU*			*USCG*
Depth			*S*	*M*	*B*	*S*	*M*	*B*	*S*	*M*	*B*	*S*
DA Skill	**Hindcast (40 Days Experiment)**	**u**	*17%*	*0*	*12%*	*27%*	*5%*	*11%*		*50%*	*15%*	*6%*
		v	*-16%*	*-7%*	*0*	*16%*	*20%*	*6%*		*21%*	*-19%*	*1%*
	Forecast (120 Days Experiment)	**u**	*-3%*	*-2%*	*0*	*6%*	*-4%*	*3%*		*26%*	*5%*	
		v	*8%*	*7%*	*13%*	*14%*	*-3%*	*-14%*		*10%*	*-2%*	

Temperature/Salinity (Fixed sensor observations)														
Station Name			*M1*	*M2*	*M3*	*SDHN4*	*ALSN6*	*BATN6*	*STBLD4*	*U206*	*44009*	*AVAN4*	*STGWBR4*	*STPR404*
Agency			*RU*	*RU*	*RU*	*NOS*	*NDBC*	*NOS*	*SIT*	*USGS*	*NDBC*	*NDBC*	*SIT*	*SIT*
Depth			*B*	*B*	*B*	*S*	*S*	*S*	*B*	*S*	*S*	*S*	*S*	*S*
DA Skill	**Hindcast (40 Days Experiment)**	**T**	*4%*	*5%*	*11%*	*34%*		*11%*	*12%*					
		S												
	Forecast (120 Days Experiment)	**T**					*16%*	*14%*	*15%*	*5%*	*22%*	*6%*	*6%*	*23%*
		S								*17%*			*7%*	*6%*

Temperature/Salinity (Slocum Glider)															
Location				*Across NJ shelf*			*Along NJ shelf*			*Across NJ shelf*			*Along NJ shelf*		
Station Name				*G1*			*G2*			*G3*			*G4*		
Agency				*RU*			*RU*			*RU*			*RU*		
Depth				*S*	*M*	*B*	*S*	*M*	*B*	*S*	*M*	*B*	*S*	*M*	*B*
DA Skill	**Hindcast (40 Days Experiment)**	T	INN	53%	9%	12%									
			MID	5%	7%	0%	6%	3%							
		S	INN	38%	3%	-4%									
			MID	0%	8%	0%	0%	-6%							
	Forecast (120 Days Experiment)	T	INN	15%	23%	10%				5%	38%	-2%			
			MID	9%	34%	-5%	4%	0%					11%	-3%	8%
		S	INN	31%	14%	-2%				1%	11%	10%			
			MID	14%	-12%	-2%	-3%	0%					17%	-3%	7%

Depth (S: near-surface, M: mid-depth, B: near-bottom), Slocum Glider (INN: inner NJ shelf, MID: mid NJ shelf)

Velocity (u: east – west component, v: north – south component), Temperature/Salinity (T: Temperature, S: Salinity)

References

Ahsan, A.K.M.O., and A.F. Blumberg (1999): "A Three-Dimensional Hydrothermal Model of Onondaga Lake, New York.", *Journal of Hydraulic Engineering*, 125, 912-923.

Anderson, D. L. T., J. Sheinbaum, and K. Haines (1996): "Data assimilation in ocean models.", *Rep. Prog. Phys.*, 59, 1209–1266.

Barrick, D. E. (1972): "First-order theory and analysis of MF/HF/VHF scatter from the sea", IEEE Trans. *Antennas Propag.*, AP-20, 2 –10.

Barrick, D. E. (1971): "Theory of HF and VHF propagation across the rough sea, 1, The effective surface impedance for a slightly rough highly conducting medium at grazing incidence", *Radio Science*, Volume 6, pp 517-526.

Barrick, D. E., M. W. Evens, and B. L. Weber (1977): "Ocean surface currents mapped by radar", *Science*, 198, 138– 144.

Barrick, D. E. and B. L. Weber (1977): "On the Non-Linear Theory for Gravity Waves on Ocean Surface, Part I, & Part II", *Journal of Physical Oceanography*, 7, NO. 1, 11.

Barrick, D. E. (1977): "Extraction of wave parameters from measured HF Radar sea echo Doppler spectra", *Radio Science*, Volume 12.

Barrick, D. E. (1979): "A Coastal Radar System for Tsunami Warning. Remote Sensing of Environment", *An Interdisciplinary Journal*, Vol-8, 353-358.

Barrick, D. E., and B. J. Lipa (1986): "Correcting for distorted antenna patterns in CODAR ocean surface measurements". *IEEE J. Oceanic Eng.*, OE-11, 304–309.

Barrick, D. E., and B. J. Lipa (1986): "Second Order Shallow Water Hydrodynamic Coupling Coefficient in Interpretation of the Sea Echo". *IEEE J. Oceanic Eng.*, OE-11.

Barrick, D. E. (2005): "Effects of Shallow water on Radar Measurements", *Codar Ocean Sensors Inc Publication*.

Beardsley, R. C. and W. C. Boicourt, (1981): "On estuarine and continental shelf circulation in the Middle Atlantic Bight". *Evolution of Physical Oceanography*, B. A. Warren and C. Wunsch, Eds.,The MIT Press, 198-223.

Beardsley, R. C., W. C. Boicourt, and D. V. Hansen (1976): "Physical oceanography of the Middle Atlantic Bight". *Limnology and Oceanography Special Symposium*, **2**, 20-34.

Bigelow, H.B. (1933): "Studies of the waters on the continental shelf, Cape Cod to Chesapeake Bay: I, The cycle of temperature". *Papers in Physical Oceanography* 2(4), 135 pp.

Blumberg, A. F., and G. L. Mellor (1980): "A coastal ocean numerical model", Proc., *Int. Symp. on Math. Modeling of Estuarine Phys*., J. Sundermann and K. P. Holz, eds., Springer, Berlin, 202–19.

Blumberg, A. F., and G. L. Mellor (1987): "A description of a three-dimensional coastal ocean circulation model", *Three-dimensional coastal ocean models. Coastal and estuarine sciences*: Volume 4, N. Heaps, ed., American Geophysical Union, Washington, D.C., 1–16.

Blumberg, A. F., B. Galperin, and D. J. O'Conner (1992): "Modeling vertical structure of open-channel flows", *J. Hydr. Engg*., ASCE, 118(8), 1119–1134.

Blumberg, A. F. and L. –Y. Oey (1985): "Modeling circulation and mixing in estuaries and coastal oceans". *Adv. In Geophysics*, 28A, 525-547.

Blumberg, A. F., L. A. Khan, and J. P. St. John (1999): "Three-dimensional hydrodynamic model of New York Harbor region", *Journal of Hydraulic Engineering*, 125, 799-816.

Blumberg, A. F., and Prichard, D. W. (1997): "Estimates of the transport through the East River, New York." *J. Geophys. Res*., 102(3), 5685–5703.

Blumberg, A. F., and M. S. Bruno (2004): "An Operational Port Security and Vessel Traffic Management System for the Port of New York and New Jersey", *Seventh Marine Transportation System Research and Coordination Conference*, The National Academy of Sciences, Washington DC, November.

Bowman, M. J (1978): "Spreading and mixing of the Hudson River effluent into the New York Bight", *Hydrodynamics of Estuaries and Fjords*, J. C. J. Nihoul, Ed., Elsevier, 373-386.

Breivik ∅, and Saetra ∅ (2001): "Real time assimilation of HF radar currents into a coastal ocean model", *Journal of Marine Systems., 28Z2001.161–182.

Bruno M. S, O. G. Nwogu, K.L. Rankin, and T. O. Herrington. (2001): "Real-Time Coastal Monitoring and Forecasting System: Preliminary Results.", *International Conference on Coastal Engineering, ASCE*. 1, 283-291.

Bruno M. S., A.F. Blumberg and T.O. Herrington. (2006): "The Urban Ocean Observatory - Coastal Ocean Observations and Forecasting in the New York Bight.", *Journal of Marine Science and Environment,* No C4, IMarEST, 1-9.

Bumpus, D.F (1973): "A description of the circulation on the continental shelf of the east coast of the United States", *In: Progr. Oceanogr.*, 6, 111-157.

CERC Technical Report – 94 - 4 (1994): "New York Bight Study Report: 1: Hydrodynamic Modeling*"*.

Chant, R. J., S. Glenn, E. Hunter, J. Kohut, R. F. Chen, and J. Wilkin (2006): „Bulge formation and cross-shelf transport of the Hudson estuarine discharge". *Eos Trans. AGU, Ocean Sci. Meet. Suppl.*, 87(6), Abstract OS34I-01.

Chant, R. J. (2002): "Secondary flows in a region of flow curvature: relationship with tidal forcing and river discharge". *Journal of Geophysical Research.* 10.1029/2001JC001082, 21 September.

Chant, R. J., S. M. Glenn, E. Hunter, J. Kohut, R. F. Chen, R. W. Houghton, J. Bosch, and O. Schofield (2008): "Bulge Formation of a Buoyant River Outflow", *J. Geophys. Res.*, 113, C01017, doi:10.1029/2007JC004100.

Chapman, R.D., L.K. Shay, H.C. Graber, J.B. Edson, A. Karachintsev, C.L. Trump, and D.B. Ross (1997): "On the accuracy of HF radar surface current measurements: Inter-comparison with ship-based sensors.", *J. Geophys. Res.,* 102 (C8), 18,737-18,748.

Chapman, R. D., and H. C. Graber (1997): "Validation of HF radar measurements", *Oceanography*, 10, 76– 79.

Choi B.-J. and J. L. Wilkin (2007): "The effect of wind on the dispersal of the Hudson River plume", *J. Physical Ocenogr*. 37(7), 1878-1897.

Cohn, S. E., A. da Silva, J. Guo, M. Sienkiewicz, and D. Lamich (1998): "Assessing the effects of data selection with the DAO Physical-space Statistical Analysis System", *Mon. Weather Rev.*, 126(11), 2913– 2926.

Crombie D (1955): "Doppler spectrum of sea echo at 13.56 Mc/s", *Nature*, vol. 175, pp. 681-682.

CODAR, Inc. (2004): "Seasonde 10: First Order Settings Document".

Daley, R (1991): "Atmospheric Data Analysis. Cambridge Atmospheric and Space Science Series.", *Cambridge University Press.* ISBN 0-521-38215-7, 457 pages.

Emery, B. M., L. Washburn and J. A. Harlan (2004): "Evaluating radial current measurements from CODAR high frequency radars with moored current meters", *J. Atmos. Oceanic Technol.*, Vol 21, pp 1259-1271.

Essen H. H., ∅ Breivik, H. Gunther, K. W. Gurgel, J. Johannessen, H. Klein, T. Schlick, and M. Stawarz (2003): "Comparison of Remotely Measured and Modeled Currents in Coastal Areas of Norway and Spain," *The Global Atmosphere and Ocean System*, Vol. 9, No. 1–2, March–June 2003, pp. 39–64.

Essen H. H (1993): "Ekman Portion of Surface Currents, as Measured by Radar in Different Areas", *Dt Hydrogr*. Z. 45.

Ezer, T. and G. L. Mellor (1994): "Continuous assimilation of Geosat altimeter data into a three-dimensional primitive equation Gulf Stream model.", *J. Phys. Oceanogr.,* 24, 832-847.

Ezer, T., and G. L. Mellor, (1997): "Simulations of the Atlantic Ocean with a free surface sigma coordinate ocean model". *Journal of Geophysical Research,* 102(C7), 15,647-15,657.

Fan, S.J., L.-Y. Oey, and P. Hamilton (2004): "Assimilation of drifters and satellite data in a circulation model of the northeastern Gulf of Mexico.", *Cont. Shelf Res.,* 24(9): 1001- 1013.

Fan, S., Blumberg, A.F., Bruno, M.S., Kruger, D., and Fullerton, B. (2006): "The skill of an urban ocean forecast system.", Spaulding, M. (ed): *Estuarine and coastal modeling: Proceedings of the ninth international conference*, Charleston, South Carolina, October 31 - September 2, 2005, Pub. ASCE, Reston, VA, 603-618.

Fukomori, I., and P. Malanotte-Rizzoli (1995): "An approximate Kalman filter for ocean data assimilation: An example with an idealized Gulf stream model.", *J. Geophys. Res.,* 100, 6777-6793.

Galperin, B., L. H. Kantha, S. Hassid, and A. Rosati (1988): "A quasi equilibrium turbulent energy model for geophysical flows", *J. Atmospheric Sci.*, 45, 55–62.

Garvine, R. W., K. –C. Wong, G.G. Gawarkiewicz, R. K. McCarthy, R.W. Houghton and F. Aikman III (1988): "The morphology of shelf-break eddies", *J. Geo. Res.*, 93, 15, 593-15, 607, December.

Georgas, N. and A. F. Blumberg (2003): "The Influence of Centrifugal and Coriolis Forces on the Circulation in a Curving Estuary.", *Estuarine and Coastal Modeling: Proceedings of the Eighth International Conference Monterey, California*, November 3-5, 2003 American Society of Civil Engineers 541-558.

Geyer, W.R. and R.J. Chant (2003): "Physical processes in the Hudson River", in *The Hudson River Ecosystem*. Levinton, J. S., (ed.) Oxford University Press.

Geyer, W. R. and H. M. Nepf, (1996): "Tidal pumping of salt in a moderately stratified estuary". *Coastal and Estuarine Studies*. **53**: 213-226.

Gonella, J. (1972): "A rotary-component method for analyzing meteorological and oceanographic vector time series.", *Deep Sea Res.*, 19, 833-846.

Gopalakrishnan, G., A. F. Blumberg, and R. Hires (2008): "Assimilating Surface Current Data into a Model of Estuarine and Coastal Ocean Circulation.", *Estuarine and Coastal Modeling: Proceedings of the Tenth International Conference,* Newport, Rhode Island, November 5-7, 2007, American Society of Civil Engineers *(in press)*.

Graber, H.C., B.K. Haus, R.D. Chapman, and L.K. Shay (1997): "HF radar comparison with moored estimates of current speed and direction: Expected differences and implications", *Journal of Geophysical Research*, 102 (C8), 18,749-18,766.

Harlan J. A. (2005): "Short Time Scale Effects on High Frequency Radar-Derived Current Velocity Measurements", *PhD Dissertation*.

Holland, W. R., and P. Malanotte-Rizzoli (1989): "Alongtrack assimilation of altimeter data into an ocean circulation model: Space versus time resolution studies.", *J. Phys. Oceanogr.,* 19, 1507-1534.

HydroQual, Inc. (2001): "Newtown Creek Water Pollution Control Project East River Water Quality Plan Task 10.0 System-Wide Eutrophication Model (SWEM) Sub-Task 10.6 Validate SWEM Hydrodynamics", prepared for *City of New York Department of Environmental Protection* under subcontract to Greeley and Hansen.

HydroQual, Inc. (2002): "A primer for ECOMSED.", Version 1.3, *Users Manual*.

Ishikawa, Y., T. Awaji, and K. Akitomo (1996): "Successive correction of the mean sea surface height by the simultaneous assimilation of drifting buoy and altimetric data.", *J. Phys. Oceanogr.,* 26, 2381-2397.

Jeffries, H.P (1962): "Environmental characteristics of Raritan Bay, a polluted estuary", *Limnol. Oceanogr.*, 7, 21-31.

Kaplan D. M., Largier. J.,Botsford W. L (2005): "HF radar observations of surface circulation off Bodega Bay (northern California, USA)", *Journal of Geophysical Research*, Vol. 110.

Kelly F. J., J. S. Bonner, J. C. Perez, J. S. Adams, D. Prouty, D. Trujillo, R. H. Weisberg, M. E. Luther, R. He, R. Cole, J. Donovan, C. R. Merz (2002): "An HF-Radar Test Deployment Amidst an ADCP Array on the West Florida Shelf", *IEEE*.

Kelley, J. G. W., F. Aikman, L. C. Breaker, G. L. Mellor, (1997): "Coastal Ocean Forecasts.", *Sea Technology*, May.

Ketchum B. H., A. C. Redfield, and J. C. Ayers (1951): "The Oceanography of The New York Bight", *Papers in Physical Oceanography and Meteorology*, MIT - WHOI.

Ketchum, B. H (1950): "Hydrographic factors involved in the dispersion of pollutants introduced into tidal waters", *J. Boston Soc. Civil Eng.*, 37:296-314.

Kohut, J. T., Roarty, H. J., and S. M. Glenn (2006): "Characterizing observed environmental variability with HF Doppler Radar surface current mappers and Acoustic Doppler Current Profilers: Environmental Variability in the Coastal Ocean Seasonal current variability on the New Jersey inner shelf.", *IEEE J. Ocean. Engr,* OE-31, 876-884.

Kohut, J. T., and S. M. Glenn (2003): "Improving HF radar surface current measurements with measured antenna beam patterns", *J. Atmos. Oceanic Technol.*, 20, 1303–1316.

Kohut, J.T., S.M. Glenn and D.E. Barrick (2001): "Multiple HF-Radar system development for a regional long-term ecosystem observatory in the New York bight", *American Meteorological Society: Fifth Symposium on Integrated Observing Systems*, 4-7.

Kohut, J. T., S. M. Glenn, D. E. Barrick (2002): "A multi-system HF radar array for the New Jersey Shelf Observing System (NJSOS)". *Oceanology International Proceedings.*

Kohut, J. T. and S. M. Glenn (2003): "Calibration of HF radar surface current measurements using measured antenna beam patterns", *J. Atmos. Ocean. Tech.*,1303-1316.

Kohut, J. T., Glenn, S. M., R. J. Chant (2004): "Seasonal current variability on the New Jersey inner shelf", *Journal of Geophysical Research*. 109, C07S07, DOI: 10.1029/2003JC001963.

Kohut, J. T., Roarty, H. J., Glenn, S. M., and R. J. Chant (2005); "Surface current response of Hudson River plume to wind forcing", *Proceedings of MTS/IEEE*, Vol. 3, pp 2540-2542.

Kundu, P. K (1976): "Ekman veering observed near the ocean bottom.", *J. Phys. Oceanogr.,* 6, 238– 242.

Laws K. (2001): "Measurements of Near Surface Ocean Currents Using HF Radar", *PhD Dissertation*, University of California.

Levitus (1998): "NODC (Levitus) World Ocean Atlas 1998". http://www.cdc.noaa.gov/cdc/data.nodc.woa98.html.

Lewis, J. K., I. Shulman, and A. F. Blumberg (1998): "Assimilation of CODAR observations into ocean models.", *Cont. Shelf Res.,* 18, 541– 559.

Lin X. –H., Oey L.-Y., and D. –P. Wang (2006): "Altimetry and Drifter Data Assimilations of Loop Current and Eddies.", *J. Geophys. Res.,* 112, C05046, doi:10.1029/2006JC003779.

Lipa, B. J. and D.E. Barrick (1983): "Least-squares methods for the extraction of surface currents from CODAR cross-loop data: application at ARSLOE.", *IEEE J. Ocean. Engr,* OE-8, 226-253.

Lipa B. J. (1978): "Inversion of Second-Order Echoes from the Sea", J*ournal of Geophysical Research*, Vol 83, No.2.

Lipa, B. J. (2005): "Directional Wave Information from the Seasonde", *IEEE J. Oceanic Eng.*, OE-30.

Lipa, B. J. (2003): "Uncertainties in Seasonde Current Velocities", *Proc. of the IEEE/OES Seventh Working Conference on Current Measurement Technology*.

Lipa B. J., Barrick. D. E., Bourg J , and B. B. Nyden (2006): "HF Radar Detection of Tsunamis", *Journal of Oceanography*, Vol. 62, pp. 705 to 716.

Mellor, G. L., and T. Yamada (1982): "Development of a turbulence closure model for geophysical fluid problems.", *Rev. Geophys. Space Phys.,* 20, 851–875.

Mellor, G.L., and T. Ezer (1991): "A Gulf Stream model and an altimetry assimilation scheme.", *J. Geophys. Res.,* 96, 8779–8795.

Molcard, A., L. I. Piterbarg, A. Griffa, T. M. Ozgogmen, and A. J. Mariano (2003): "Assimilation of drifter observations for the reconstruction of the Eulerain circulation field.", *J. Geophys. Res.,* 108, NO. C3, 3056, doi:10.1029/2001JC001240.

Mukai, A.Y., J.J. Westerink, R.A. Luettich (2002): "Guidelines for Using East coast 2001 Database of Tidal Constituents within Western North Atlantic Ocean, Gulf of Mexico and Caribbean Sea.", *US Army Corp of Engineers. ERDC/CHL CHETN-IV-40*.

New Jersey marine Science Consortium (NJMSC) (1997): "The biology of the Hudson-Raritan Estuary: A teachers guide", *NJMSC*-E-97-002.

New York City Department of Environmental Protection (DEP) (2003): "New York Harbor Water Quality Report 2003".

New York/ New Jersey Harbor Estuary Program., Hudson River Foundation.

Oey, L.-Y., Mellor, G. L., and R. I. Hires (1985a): "A three dimensional simulation of the Hudson-Raritan Estuary. Part I: Description of the model and model simulations", *J. Phys. Oceanography*, 15, 1676–1692.

Oey, L. –Y., G. L. Mellor and R. I. Hires, (1985b): "A three-dimensional simulation of the Hudson-Raritan estuary. Part II: Comparison with observation", *J. Phys. Oceanography*., 15, 1693-1709.

Oke, P. R., J. S. Allen, R. N. Miller, G. D. Egbert, J. A. Austin, J. A. Barth, T. J. Boyd, P. M. Kosro, and M. D. Levine (2002): "A modeling study of the three-dimensional continental shelf circulation off Oregon, Part-I, Model-data comparisons.", *J. Phys. Oceanogr.,* 32, 1360–1382, 2002a.

Oke, P. R., J. S. Allen, R. N. Miller, G. D. Egbert, and P. M. Kosro (2002): "Assimilation of surface velocity data into a primitive equation coastal ocean model.", *J. Geophys. Res.*, 107, 3122, doi: 10.1029/2000JC000511.

Ozgokmen, T. M., A. Molcard, T. M. Chin, L. I. Piterbarg, and A. Griffa (2003): "Assimilation of drifter observations in primitive equation models for midlatitude ocean circulation.", *J. Geophys. Res.,* 108, NO. C7, 3238, doi:10.1029/2002JC001719.

Paduan, J. D., and H. C. Graber (1997): "Introduction to high-frequency radar: reality and myth.", *Oceanography*, vol. 10 No.2 pp. 36-39.

Paduan, J. D., and L. K. Rosenfeld (1996): "Remotely sensed surface currents in Monterey Bay from shore-based HF radar (Coastal Ocean Dynamics Application Radar).", *J. Geophys. Res.,* 101 (C9), 20,669-20,686.

Paduan, J. D., and I. Shulman (2004): "HF radar data assimilation in the Monterey Bay area.", *J. Geophys. Res.,* 109, C07S09, doi:10.1029/2003JC001949.

Pawlowicz, R., R. Beardsley, and S. Lentz (2002): "Classical tidal harmonic analysis including error estimates in MATLAB using T_TIDE.", *Computers & Geosciences,* 28, 929-937.

Prandle, D (1987): "The fine-structure of near-shore tidal and residual circulations revealed by H.F. radar surface current measurements", *J. Phys. Oceanogr.*,17, 231– 246.

Schmidt, R. O. (1986): "Multiple emitter location and signal parameter estimation", *IEEE Trans. Antennas and Propagation*, vol. AP-34, no. 3, pp. 276-280.

Shay L. K., Thomas C. M., Hartmut P., Arthur M. J., Robert W., Edgar P. An., Alexander S., and L. Mark (2002): "Very High-Frequency Radar Mapping of Surface Currents", *IEEE Journal of Oceanic Engineering*, Vol. 27, NO. 2, April.

Shulman, I., C.-R. Wu, J. K. Lewis, J. D. Paduan, L. K. Rosenfeld, J. D. Kindle, S. R. Ramp, and C. A. Collins (2002): "High resolution modeling and data assimilation in the Monterey Bay area.", *Cont. Shelf Res.,* 22, 1129–1151.

Smagorinsky, J., (1963): "General circulation experiments with the primitive equations. Part I: the basic experiment.", *Monthly Weather Review,* 91, 99-164.

Stewart, R.H. and J.W. Joy (1974): "HF radio measurement of surface currents.", *Deep-Sea Res.,* 21, 1039-1049.

The Oceanographic Society (1997): "Special Issue on High Frequency Radars for Coastal Oceanography", *Oceanography*, 10, 76– 79.

Townsend D. W., Andrew C. T., Lawrence M. M., Maura A. T., and John A. Q (2004): "Oceanography of the Northwest Atlantic Continental Shelf (1,W)", *The Sea: The Global Coastal Ocean: Interdisciplinary Regional Studies and Syntheses*. Harvard University Press (in press), Robinson, A.R. and K.H. Brink (eds).

Wilkin J. L., Hernan A.G., Haidvogel D. B., Lichtenwalner S. C., Glenn S. M., and K. S. Hedstrom (2005): "A regional ocean modeling system for the Long-term Ecosystem Observatory.", *J. Geophys. Res.,* 110, C06S91, doi:10.1029/2003JC002218.

VITA

Name

Ganesh Gopalakrishnan

Date and Place of Birth

6th January, 1977, Kozhikode, Kerala state, India.

Education

Doctor of Philosophy (PhD) in Ocean Engineering *August 2008*
Department of Civil, Environmental and Ocean Engineering, Stevens Institute of Technology, Hoboken, NJ

Thesis Advisors	:	Prof. Alan Blumberg and Prof. Richard Hires
Thesis Title	:	Surface Current Observation using High Frequency Radar and its Assimilation into the New York Harbor Observing and Prediction System

Master of Science (MS by Research) in Ocean Engineering *December 2002*
Indian Institute of Technology, Madras, India

Thesis Advisor	:	Prof. V. Sundar
Thesis Title	:	Numerical Modeling for the Transformation of Waves in Coastal Waters

Bachelor of Technology (B-Tech) in Civil Engineering *October 1998*
National Institute of Technology - Calicut, Kerala State, India

Thesis Advisor	:	Prof. Mohammed Ameen
Thesis Title	:	Optimized Design of Reinforced Concrete Structures using Genetic Algorithm Technique and Analysis using Finite Element Method

Research Experience

Graduate Research Assistant
Center for Maritime Systems, Department of Civil, Environmental and Ocean Engineering,
Stevens Institute of Technology, Hoboken, NJ
September 2005 - Present

Graduate Research Assistant
Department of Ocean Engineering, Indian Institute of Technology, Madras
October 1999 - July 2003

Teaching Experience

Department of Civil, Environmental and Ocean Engineering

Stevens Institute of Technology, Hoboken, NJ
September 2004 - August 2005
Probability and Statistics for Engineers

Industrial Experience

Mentor Subsea Technology Services Inc (MSTS)
J.Ray Mc Dermott, Dubai, Middle East, S.A. (JRM)
Subsea & Pipeline Engineer
August 2003 - August 2004

Publications

"Assimilating Surface current Data into a Model of Estuarine and Coastal Ocean Circulation"., **Ganesh Gopalakrishnan**, Alan Blumberg, and Richard Hires., *10th International Conference on Estuarine and Coastal Modeling,* Newport, Rhode Island, Nov 5 – 7, 2007.

"HF Radar Data Assimilation into the New York Harbor Observing and Prediction System"., **Ganesh Gopalakrishnan** and Alan Blumberg, *Journal Article (in Prep).*

"Numerical model study for the coastal protection works at Kanyakumari district, Tamilnadu"., V. Sundar, R. Sundaravadivelu, **G. Ganesh**, K.A. Roopsekhar., *National Seminar on Harbor Structures–NASHAR'2003.,* IIT-Madras, India, February 2003.

"River mouth improvement works - Muara Sungai Kuantan experience"., Sundar,V., Roopsekhar, K.A., **Ganesh, G**. and YogaChandran, L., *Second world Engineering Congress.*, Kuching, Malaysia, 22-25, July 2002.

"Studies on the remedial measures for controlling the mouth closure of River Kuantan, Malaysia"., Sundar, V., Roopsekhar,K.A., **Ganesh,G**. and Yogachandran,L., *Journal of Coastal Research (under Review).*

"Numerical model for the prediction of wave transformations"., **Ganesh, G** and Sundar,V., *International Conference in Ocean Engineering–ICOE'2001.*, IIT- Madras, India, December 2001, Vol: 2, pp.539-544.

"Numerical modeling of combined refraction and diffraction of waves and its application"., **Ganesh, G** and Sundar, V., *2nd International Conference on Theoretical, Applied, Computational, and Experimental Mechanics-ICTACEM'2001.,* IIT-Kharagpur, India, December 2001, Paper no: 050.

"Numerical model for the prediction of the wave climate in the near shore"., **Ganesh, G** and Sundar, V., *3rd International Conference on Marine Industry–MARIND'2001.,* Varna, Bulgaria, June 2001, Vol: 2, pp 253-264.

Oral Presentations

"Assimilation of HF Radar Data into Ocean Circulation Model during an Extreme Weather Event"., **Ganesh Gopalakrishnan**, Alan Blumberg, Michael Bruno., *2008 Ocean Sciences Meeting,* Orlando, Florida, Mar 2 – 7, 2008.

"Assimilating Surface current Data into a Model of Estuarine and Coastal Ocean Circulation"., **Ganesh Gopalakrishnan**, Alan Blumberg, and Richard Hires., *10th International Conference on Estuarine and Coastal Modeling.,* Newport, Rhode Island, Nov 5 – 7, 2007.

"HF Radar Data Assimilation into the New York Harbor Observing and Prediction System: A Nudging Approach" ., **Ganesh Gopalakrishnan**, Alan Blumberg, Richard Hires., *Mid Atlantic Bight Physical Oceanography and Meteorology (MABPOM),* Rutgers University, New Brunswick, Oct 30, 2007.

"Numerical model study for the coastal protection works at Kanyakumari district, Tamilnadu"., V. Sundar, R. Sundaravadivelu, **G. Ganesh**, K.A. Roopsekhar., *National*

Seminar on Harbor Structures–NASHAR'2003., IIT-Madras, India, February 2003.

"Numerical model for the prediction of wave transformations"., **Ganesh, G** and Sundar,V., *International Conference in Ocean Engineering–ICOE'2001.*, IIT- Madras, India, December 2001, Vol: 2, pp.539-544.

"Numerical modeling of combined refraction and diffraction of waves and its application"., **Ganesh, G** and Sundar, V., *2nd International Conference on Theoretical, Applied, Computational, and Experimental Mechanics-ICTACEM'2001.,* IIT-Kharagpur, India, December 2001, Paper no: 050.